



HAL
open science

Managing Expectations and Imbalanced Training Data in Reactive Force Field Development : An Application to Water Adsorption on Alumina

Loïc Dumortier, Céline Chizallet, Benoit Creton, Theodorus de Bruin, Toon Verstraelen

► **To cite this version:**

Loïc Dumortier, Céline Chizallet, Benoit Creton, Theodorus de Bruin, Toon Verstraelen. Managing Expectations and Imbalanced Training Data in Reactive Force Field Development : An Application to Water Adsorption on Alumina. *Journal of Chemical Theory and Computation*, 2024, 20 (9), pp.3779-3797. 10.1021/acs.jctc.3c01009 . hal-04695974

HAL Id: hal-04695974

<https://ifp.hal.science/hal-04695974v1>

Submitted on 12 Sep 2024

HAL is a multi-disciplinary open access archive for the deposit and dissemination of scientific research documents, whether they are published or not. The documents may come from teaching and research institutions in France or abroad, or from public or private research centers.

L'archive ouverte pluridisciplinaire **HAL**, est destinée au dépôt et à la diffusion de documents scientifiques de niveau recherche, publiés ou non, émanant des établissements d'enseignement et de recherche français ou étrangers, des laboratoires publics ou privés.

Managing Expectations and Imbalanced Training Data in Reactive Force Field Development: an Application to Water Adsorption on Alumina

Loïc Dumortier,^{†,‡} Céline Chizallet,[¶] Benoit Creton,[†] Theodorus de Bruin,[†] and
Toon Verstraelen^{*,‡}

[†]*IFP Energies nouvelles, 1 et 4 Avenue de Bois-Préau, 92852 Rueil-Malmaison, France*

[‡]*Center for Molecular Modeling (CMM), Ghent University, Technologiepark-Zwijnaarde 46,
B-9052, Zwijnaarde, Belgium*

[¶]*IFP Energies nouvelles, Rond-point de l'échangeur de Solaize, BP3, 69360 Solaize, France*

E-mail: toon.verstraelen@ugent.be

Abstract

ReaxFF is a computationally efficient model for reactive molecular dynamics simulations, which has been applied to a wide variety of chemical systems. When ReaxFF parameters are not yet available for a chemistry of interest, they must be (re)optimized, for which one defines a set of training data that the new ReaxFF parameters should reproduce. ReaxFF training sets typically contain diverse properties with different units, some of which are more abundant (by orders of magnitude) than others. To find the best parameters, one conventionally minimizes a weighted sum of squared errors over all data in the training set. One of the challenges in such numerical optimizations is to assign weights so that the optimized parameters represent a good compromise between all the requirements defined in the training set. This work introduces a new loss function, called Balanced Loss, and a workflow that replaces weight assignment with a more manageable procedure. The training data is divided into categories with corresponding “tolerances”, i.e. acceptable root-mean-square errors for the categories, which define the expectations for the optimized ReaxFF parameters. Through the Log-Sum-Exp form of Balanced Loss, the parameter optimization is also a validation of one’s expectations, providing meaningful feedback that can be used to reconfigure the tolerances if needed. The new methodology is demonstrated with a non-trivial parameterization of ReaxFF for water adsorption on alumina. This results in a new force field that reproduces both rare and frequent properties of a validation set not used for training. We also demonstrate the robustness of the new force field with a molecular dynamics simulation of water desorption from a γ -Al₂O₃ slab model.

1 Introduction

Reactive force fields are widely used in Molecular Dynamics (MD) simulations because they combine low computational cost, close to that of Molecular Mechanics (MM) models, with the ability to describe chemical events, similar to more expensive Quantum Mechanics (QM) methods, such as Density Functional Theory (DFT). Unlike hybrid QM/MM schemes,¹ re-

active force fields handle many simultaneous chemical reactions throughout the simulation cell, not just in one predefined active site. This is advantageous for the direct simulation of reaction networks² of complex chemical processes such as combustion,³ pyrolysis,^{4,5} chemisorption,^{6,7} catalysis,⁷ mechanochemistry,⁸ crack propagation,⁹ nucleation,^{10,11} and so on. ReaxFF is one of the most established reactive force fields and is efficient enough to perform multi-nanosecond MD of systems with thousands of atoms using only a single high-performance compute node.¹²⁻¹⁴ Compared to other popular reactive force fields such as Tersoff,¹⁵ AIREBO-M,¹⁶ or COMB3,¹⁷ ReaxFF has been parameterized for more diverse chemical spaces.¹⁴ More recently, machine learning potentials have also been proposed for reactive MD simulations.¹⁸⁻²⁰ All of these models share the ambition to simulate complex chemical systems at a computational cost that scales like MM models.

The computational efficiency of reactive force fields comes at a price. They are generally empirical models, sometimes inspired by physical principles, whose parameters must be fitted to reproduce a chemistry of interest. Such parameterization is fraught with challenges: the collection of reference data sets for training and validation, the choice of numerical optimization algorithm, the selection of parameters to optimize, the computational burden of the parameter optimization, and so on. Specifically for ReaxFF, many optimization algorithms have been proposed and tested,²¹⁻²⁹ while the design of reference data sets has received much less attention. For example, ReaxFF parameters are rarely published with their training sets in a reusable form, save for a few exceptions.^{8,25,27,28,30,31} However, these data are vital, as they specify the requirements for the optimized parameters and no models will ever outperform the data it was trained on.

A conventional ReaxFF training set consists of various target properties of relevant molecular or periodic structures, including internal coordinates, energy differences and atomic forces. Reaction energies and barriers are obviously important for reactive force fields, but for a training set of N systems, one has at most $N - 1$ independent energy differences and many more internal coordinates and atomic forces. In the context of machine learning po-

tentials, this imbalance is addressed by weighting data categories (typically energies and forces) inversely proportional to their prevalence,³²⁻³⁴ but this practice is less established in the context of ReaxFF. Moreover, in ReaxFF, such weights are often adjusted empirically. For example, one gives more weight to an important subset of the training data in order to prioritize the performance of the trained model for that subset.^{26,35,36} Conversely, the model of interest may also be inherently limited for some subsets of reference data, making it pointless to give high weight to such subsets. These subjective motivations mean that training set design requires expert judgment. To make this task more accessible to a broader audience, this paper introduces a new loss function and an intuitive workflow for reweighting training data, called Balanced Loss. It naturally takes into account data imbalance and inherent strengths and weaknesses of the model being trained. A ReaxFF parameterization is used as a case study in this paper, because we believe ReaxFF can greatly benefit from Balanced Loss, but the methodology is general enough to be applied to other (even non-chemical) parameterizations with similar challenges.^{29,37-42} As software tools and algorithms for (re)parameterizing (reactive) force fields improve,^{24,26-29,43,44} we expect that more practitioners to face the challenge of data imbalance, also for machine learning potentials that are trained on increasingly large and diverse data sets.⁴⁵⁻⁴⁷

Alumina provides a great test case for ReaxFF parameterization because it is a versatile and widely used material in the chemical industry with a complex chemistry,⁴⁸⁻⁵² also at scales out of reach for DFT. Alumina has many known polymorphs, including γ -Al₂O₃, α -Al₂O₃, δ -Al₂O₃ and θ -Al₂O₃,⁵³ of which γ -Al₂O₃ is the most relevant for catalytic applications.^{54,55} For example, alumina selectively adsorbs unwanted elements such as sulfur and can be used as a catalyst for the dehydration of alcohols to ethers and olefins.⁵⁶⁻⁶¹ However, the main application of γ -Al₂O₃ is in the automotive and petrochemical industries, where it serves as a support for other heterogeneous catalysts such as metals, metal sulfides or metal oxides.^{54,62-64} Despite their massive use in industry, the design of alumina-supported catalysts is an empirical process, partly due to the limited fundamental understanding of the

materials involved. For example, the exact structure of γ - Al_2O_3 is still under discussion due to its poor crystallinity.^{54,65} Also, the microscopic mechanisms at the water-alumina interface during support preparation, metal phase impregnation, shaping and use as a catalyst remain unclear.⁶⁶

The formation, stability and structure of γ - Al_2O_3 are controlled by hydration and dehydration processes.^{51,52,67-70} The γ phase is formed upon dehydration of boehmite at temperatures between 700 K and 800 K. Once formed, the γ polymorph remains stable up to 1100 K under dry conditions.^{54,55,71} γ - Al_2O_3 transitions to other polymorphs upon further increase in temperature and/or water partial pressure. Having both Lewis acid and basic sites on the surface, alumina can react with water in several ways depending on temperature, water partial pressure (for gas/solid interfaces) and pH (for liquid/solid interfaces).^{49-52,68,72} Water can adsorb without dissociation by forming an Al-O bond. One of the O-H bonds of water may then dissociate and react with a surface Al-O pair, resulting in two hydroxyl groups, called aluminols. Dissociative adsorption is reported to be more prevalent at crystal surface defects, leading to an “etching”-like degradation at these positions.^{73,74} It is clear that the chemistry at the $\text{H}_2\text{O}/\gamma\text{-Al}_2\text{O}_3$ interface is highly complex and depends on an interplay of multiple microscopic mechanisms and external conditions.

Molecular simulation of the $\text{H}_2\text{O}/\gamma\text{-Al}_2\text{O}_3$ interface is a promising but ambitious method to improve our understanding of widely used supported catalysts and to pave the way towards their rational design. DFT has often been used to model the $\text{H}_2\text{O}/\gamma\text{-Al}_2\text{O}_3$ interface.^{50,52,67,69,70,75,76} Ideally, sufficiently large atomistic models are considered to avoid artificial spatial correlations, to introduce defects at low concentrations, to include both support and catalyst, and to mimic realistic water concentrations.⁷⁷⁻⁷⁹ Because larger models also have a larger configurational space, with many local minima on the potential energy surface, their properties can no longer be simulated with static calculations and one should resort to MD to sample all relevant configurations.⁸⁰ Linear-scaling DFT implementations^{81,82} have enabled ab initio MD simulations of the $\text{H}_2\text{O}/\gamma\text{-Al}_2\text{O}_3$ interface,⁸³⁻⁸⁵ but they are still com-

putationally demanding compared to reactive force fields. Compared to linear-scaling DFT, ReaxFF has a much lower computational cost, allowing for large-scale MD simulations of alumina.⁸⁶⁻⁹⁴ The first alumina and water ReaxFF parameters were proposed by Zhang *et al.*,⁸⁶ and these were later refined and extended by Joshi *et al.* for aluminosilicates and water,^{88,90} which is particularly relevant for simulations of alumina-supported catalysts. However, as shown in the results, the state-of-the-art ReaxFF parameters by Joshi *et al.* poorly reproduce DFT reference data for water adsorption on alumina. This motivated us to demonstrate the relevance of Balanced Loss with a reparameterization of ReaxFF for H₂O/ γ -Al₂O₃ interactions, using DFT data from the literature.^{70,76,83,95}

The rest of the paper is structured as follows. Section 2 contains the methodological details of the study: a brief overview of ReaxFF, the generation of the training and validation data sets, the parameter selection and the optimization algorithm. The Balanced Loss function and workflow are described and motivated in detail in section 3. Section 4 presents the results of the ReaxFF training and validation, and it demonstrates the suitability of the resulting force field for MD simulations. The last section formulates the main conclusions and gives an outlook on future work.

2 Methodology

2.1 ReaxFF Reactive Force Fields

ReaxFF was developed and introduced in 2001 by van Duin *et al.* for reactive MD simulations, initially of hydrocarbons,¹² and has since been regularly extended to other chemistries.¹⁴ Like all force fields, it is a mathematical model of the interactions between atoms in a molecule or a condensed phase, as a function of the Cartesian coordinates of the atomic nuclei. Unlike most classical force fields, it can describe bond breaking and formation.

The ReaxFF potential energy of an atomistic model is defined as:

$$\begin{aligned}
 E_{\text{system}} = & E_{\text{bond}} + E_{\text{over}} + E_{\text{under}} + E_{\text{val}} + E_{\text{tors}} \\
 & + E_{\text{vdW}} + E_{\text{charge}} + E_{\text{specific}}
 \end{aligned}
 \tag{1}$$

where E_{bond} describes the energy of an atom pair in all relevant regimes: bonded, in transition states and dissociated. E_{over} and E_{under} are correction terms for over- and under-coordination, respectively. E_{val} is the valence angle energy and E_{tors} is the torsional angle energy between four different particles. Non-covalent interactions are modeled with E_{charge} and E_{vdW} , the charge and the van der Waals interactions, respectively. The atomic charges are variable and account for polarization and Coulomb forces.^{96,97} In addition to these commonly used energy terms, ReaxFF contains additional contributions for specific use cases, grouped into E_{specific} , which are not used in this work.

The covalent terms depend on bond orders (BO), which are defined for each pair of atoms and allow ReaxFF to describe bond breaking and formation processes in chemical reactions. The uncorrected bond order of a pair of atoms consists of three terms, each corresponding to one type of covalent bond, σ , π and $\pi\pi$:

$$\begin{aligned}
 \text{BO}'_{ij} = & \text{BO}'_{ij,\sigma} + \text{BO}'_{ij,\pi} + \text{BO}'_{ij,\pi\pi} \\
 = & \exp\left(p_{\text{bo},1} \left(\frac{r_{ij}}{r_0^\sigma}\right)^{p_{\text{bo},2}}\right) + \exp\left(p_{\text{bo},3} \left(\frac{r_{ij}}{r_0^\pi}\right)^{p_{\text{bo},4}}\right) + \exp\left(p_{\text{bo},5} \left(\frac{r_{ij}}{r_0^{\pi\pi}}\right)^{p_{\text{bo},6}}\right)
 \end{aligned}
 \tag{2}$$

where $p_{\text{bo},\{x\}}$ represent tunable parameters that can be different for each pair of chemical elements. r_{ij} is the interatomic distance and r_0^σ , r_0^π and $r_0^{\pi\pi}$ are the element-specific σ , π and $\pi\pi$ equilibrium bond lengths, respectively. The expression for the uncorrected bond orders in Eq. (2) features only a small subset of all the adjustable ReaxFF parameters. ReaxFF has additional equations (with more parameters) to convert uncorrected to corrected bond orders, which are then used in expressions for the covalent energy terms. A full description can be found in the AMS documentation⁹⁸ and in the supporting information of Ref. 99.

ReaxFF has been implemented in several software packages. The most established ones are the original “Standalone ReaxFF” distributed by van Duin, the commercial implementation in the Amsterdam Modeling Suite (AMS)¹⁰⁰ and the open-source version in the LAMMPS package.^{101,102} In this paper, the ReaxFF implementation from AMS (release 2023.101) is used. The parameter optimization, discussed below, is implemented with ParAMS,^{43,103} which is a recently developed tool in AMS for the parameterization of approximate potential energy surfaces, such as ReaxFF or Density Functional Tight-Binding (DFTB) models.^{39,104} In addition, the Atomistic Simulation Environment¹⁰⁵ was used for processing DFT calculations in the training and validation sets. Visual Molecular Dynamics (VMD) is used for the 3D visualizations in this work.¹⁰⁶

2.2 Training Set Development

The development of the training set goes through the following steps: (i) the selection of bulk, (hydrated) surface and (hydrated) edge structures, (ii) periodic DFT reference calculations on these structures and (iii) the selection of properties from these calculations as training targets.

(i) Structures. A training set for optimizing ReaxFF parameters requires reference structures and associated training targets, such as internal coordinates or energies, that ReaxFF should reproduce. The reference structures were taken from previous publications^{70,76,83,95} and can be divided into five groups, summarized in Table 1 and described in more detail below. For clarity, the relevant crystal surfaces are shown in Figure 1. Note that γ -Al₂O₃ is industrially the most relevant material, yet other forms of (hydrated) aluminum oxide were included, most notably boehmite, to increase the diversity of the training data. A complete list of structures is provided in Table S1 of the Supporting Information.

- The group of **Bulk Structures** contains 3D-periodic models of boehmite, γ -Al₂O₃ and α -Al₂O₃.⁶⁷

- The group of γ -**Al₂O₃ Surfaces** is based on three different slab models, cut along the (100), (110) or (111) crystal planes. In addition to the bare surfaces, structures are included with an increasing number of water molecules adsorbed on the surface.⁷⁰ All the structures were published before a distinction was made between the lateral (110)_ℓ and basal (110)_b surfaces of γ -Al₂O₃, as shown in Figure 1.^{52,76} The (110) γ -Al₂O₃ surfaces in the training set are in fact all lateral (110)_ℓ surfaces.
- The group of **Boehmite Surfaces** contains slabs with four surface orientations: (101), (010), (100) or (001). Boehmite already contains water in its bulk structure, which is preserved upon cleaving the slabs. In addition to the bare slabs, some have additional water molecules adsorbed.^{83,95}
- The group of γ -**Al₂O₃ Edges** comprises structures that represent the edge between surface orientations (100) and (110). In addition to the bare edge structure, six structures with an increasing number of adsorbed water molecules are included.⁷⁵
- The group of **Small Molecules** contains two structures: a γ -alumina monomer, [Al(OH)₄]⁻H⁺, and water.¹⁰⁷

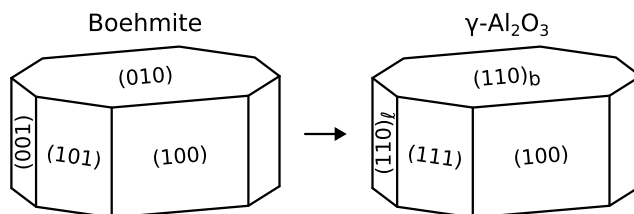


Figure 1: Overview of the crystal surfaces of boehmite and γ -Al₂O₃, with the relation between the two as proposed in Ref. 52.

(ii) Periodic DFT calculations. The geometries of all structures in Table 1 are optimized with DFT using periodic boundary conditions and the Perdew, Burke and Ernzerhof (PBE) exchange-correlation functional as implemented in the Vienna Ab initio Simulation Package

Table 1: Overview of the structures in the training set. For surface and edge structures, the number of structures with additional water adsorbed on the surface is mentioned in the last column.

Group	Structure	Nr. of structures with additional water
Bulk Structures	Bulk α -Al ₂ O ₃	–
	Bulk boehmite	–
	Bulk γ -Al ₂ O ₃	–
γ -Al ₂ O ₃ Surfaces	γ -Al ₂ O ₃ (100)	4
	γ -Al ₂ O ₃ (110)	6
	γ -Al ₂ O ₃ (111)	3
Boehmite Surfaces	Boehmite (101)	1
	Boehmite (010)	0
	Boehmite (100)	2
	Boehmite (001)	1
γ -Al ₂ O ₃ Edges	γ -Al ₂ O ₃ (100-110)	6
Small molecules	[Al(OH) ₄] [–] H ⁺ monomer	–
	Water	–

(VASP) version 5.4.^{108,109} The valence interactions are described with the Projected Augmented Wave (PAW) method.¹¹⁰ An additional *a posteriori* density-dependent dispersion correction dDsC is applied.¹¹¹ The plane wave basis set cutoff is 600 eV, which is increased compared to original works from which the structures were taken,^{70,76,83,95} to improve the precision of the forces and to facilitate the geometry optimizations. The k-point spacing is set to 0.5 \AA^{-1} and a Gaussian smearing is used with a width of 0.05 eV. The convergence criterion for the self-consistent field calculation is set to 1×10^{-5} eV. The geometry optimization is performed with the conjugate gradient algorithm and uses a convergence criterion of 0.02 eV/\AA on the forces. The cell parameters were not allowed to change and were taken from previous works.^{70,76,83,95}

(iii) Property Extraction. The selection of internal coordinates, used as training targets, consists of two phases: an analysis of interatomic distances to determine appropriate cutoffs for relevant atom pairs, followed by a classification and enumeration of all relevant distances and angles.

In phase 1, histograms of all interatomic distances up to 5.0 Å were constructed per pair of chemical elements, as shown in Figure S1 in the supporting information. From these histograms, cutoff distances were derived to classify and enumerate all relevant atom pairs. All OH pairs with a distance below 1.2 Å are classified as covalent O–H bonds. Remaining OH distances below 2.1 Å are identified as O···H hydrogen bonds. The AlO distances below 2.8 Å are treated as Al–O bonds. AlAl distances below 4.0 Å are not directly bonded, but are included because they are relevant for the local structure of alumina. No other distances were included in the training set.

In phase 2, the distances defined in phase 1 are used to construct the final set of internal coordinates. In addition to distances, valence angles are constructed by combining all pairs of bonded atom pairs sharing one central atom. Dihedral angles are not included, because most O–Al–O–X quartets, where X can be H or Al, contain nearly co-linear bonds, making the dihedral angle ill-defined. Furthermore, H–O–H angles are not included because, for reasons of backward compatibility explained in the following section, the corresponding valence angle term parameters are kept fixed at the values of Joshi *et al.*^{88,90} To avoid obvious redundancies in the training set, internal coordinates involving no hydrogen atoms were discarded for structures with additional water molecules, as these internal coordinates already appear in the bare surface and edge structures. The final set comprises four categories of distances (Al–O, Al–Al, O–H and O···H) and six categories of valence angles (O–Al–O, Al–O–Al, Al–O–H, Al–O···H, H–O···H and H···O···H). Note that the last two categories are still relevant to include, unlike H–O–H angles, because hydrogen bonding angles are sensitive to the structure of the boehmite and alumina surfaces.

Histograms of the final selection of internal coordinates can be found in Figures S2 (combined) and S3 (per material) of the Supporting Information. The internal coordinates of boehmite are somewhat similar to those of γ -Al₂O₃, with larger deviations related to hydrogen bonds. Hence, the inclusion of boehmite in the training set increases the diversity of hydrogen bonding information. The prevalence of each class of internal coordinates per

structure is given in Table S1.

Energies in a ReaxFF training set are conventionally formulated as internal energy differences between reactant and product states. A full list of reaction energies in the training set is provided in Table S2 of the Supporting Information. These energies are grouped into five classes, denoted with three-letter codes: **BSH**, **GEH**, **GSH**, **SUR** and **FOR**. A short summary of the included reactions and their classification is given below.

For a given alumina surface or edge structure X, all unique pair of adsorption states are used to construct adsorption energy training data, to avoid bias towards a particular reference state. Let m_i and $m_j > m_i$ be the number of water molecules adsorbed in states X_i and X_j , respectively, then the corresponding adsorption energy in the training set is defined as:

$$\Delta_r E_{\text{ads},X_j,X_i} = \frac{E_{X_j} - E_{X_i}}{m_j - m_i} - E_{\text{H}_2\text{O}} \quad (3)$$

Thus, if there are N states with water adsorbed for a given structure, there are $(N - 1)N/2$ corresponding adsorption energies in the training set. By normalizing the adsorption energies on the number of H_2O molecules added, they all have approximately the same order of magnitude. The adsorption energies were grouped into three classes: adsorption on boehmite surfaces (**BSH**), on $\gamma\text{-Al}_2\text{O}_3$ edges (**GEH**) and on $\gamma\text{-Al}_2\text{O}_3$ surfaces (**GSH**).

While the water adsorption energies are of primary interest, also other energies were included to diversify the training set: the transformation from bulk to a slab models (class **SUR**) and the formation of bulk and slab models from the alumina monomer (class **FOR**) are included. Such “reactions” do not correspond to specific reactive events, but they do provide useful information for the covalent ReaxFF parameters.

The resulting training set contains 12931 distances, 13409 angles, 63 water adsorption energies and 19 other energies, for a total of 26422 training targets. Notably, the geometrical features, such as angles and distances, far outnumber the energy entries in the training set. The categories of internal coordinates and energies will be used in the remainder of the paper for a detailed statistical analysis and in the construction of the Balanced Loss function.

It is worth noting that our training set is considerably larger than those of previous ReaxFF parameterizations, which typically contain hundred to a several thousand training targets.^{8,23,28,30,31,112–114} To the best of our knowledge, the only exception is the ReaxFF model by Trnka *et al.* for enzyme chemistry, which was trained with 385826 entries.²⁵ Note that their training set consists of single-point energies and forces, making it computationally less expensive, whereas ReaxFF is normally trained by optimizing geometries at each iteration of the parameter optimization.²⁹

2.3 Parameter Selection

When calibrating ReaxFF parameters, a careful selection of adjustable parameters must be made. Some parameters can be taken from previous works without refinement, others are not intended to be adjusted, such as the atomic mass, and some parameters are not meaningful for the application of interest. In addition, simply optimizing all parameters would result in an intractable high-dimensional optimization problem. The total number of ReaxFF parameters depends on the number of chemical elements in the system. The parameters are typically grouped into blocks, most of which can be repeated several times for different combinations of chemical elements. Parameter blocks can be independent of chemical elements (41 general parameters), defined per chemical element (32 atomic parameters), per pair (16 bond and 6 off-diagonal parameters), per triplet (7 angle and 4 hydrogen-bond parameters), or per quartet of elements (7 torsion parameters).

In this work, the selection of parameters follows a top-down approach. Initially, all parameters from a literature force field are considered,^{88,90} after which several selection criteria are introduced to fix parameters to their literature values, leaving only the remainder to be refined. The selection process aims for a trade-off between an acceptable dimensionality of the optimization problem and a sufficient model flexibility to obtain a good fit. In the following paragraphs, we motivate our selection criteria, which may be helpful for future ReaxFF calibrations.

Our starting point is the aluminosilicate force field by Joshi *et al.*^{88,90} These ReaxFF parameters were calibrated to improve the description of water adsorption at acid sites, Si–O(H)–Al, in the H-ZSM-5 zeolite.¹¹⁵ The literature `ffield` file contains parameters for 13 chemical elements and one dummy element, resulting in a set of 2961 parameters, many of which are irrelevant to aluminosilicates. For this work, we only consider parameter blocks that contain at least one Al element, and otherwise only allow O or H. All other parameters are kept fixed, including those related to Si, or those describing water.

Ideally, our reparameterization would maintain backward compatibility with the Joshi *et al.* model, changing only parameters specific to alumina and irrelevant to acid sites in zeolites. However, this severely restricts the adjustable parameters to those of atom pairs and valence angles involving at least two Al atoms, namely the Al–Al pairs, and the Al–X–Al and Al–Al–X angles, where X can be Al, O or H. Of this selection, only Al–O–Al angles and Al–Al pairs ($\geq 2.5 \text{ \AA}$) appear in the training set. As a result of this mismatch, no satisfactory reproduction of our training data was possible when imposing backward compatibility. To avoid this mismatch, we made a pragmatic selection that includes some parameters related to acid sites in zeolites, but also excludes parameters that are only remotely related to our training data. This selection includes Al atom parameters, Al–X bond or pair parameters and Al–H–O, Al–O–H, Al–O–Al, H–Al–O and O–Al–O valence angle parameters.

We further narrow down the parameter selection using the recommendations from the ParAMS documentation.^{43,103} In the ParAMS, each parameter is classified with one of the following three labels: “Standard”, “Expert” or “DoNotOptimize”. The first label indicates that the parameter is generally safe to optimize. The second label is used for parameters that should not be changed without a strong motivation. Parameters with the “DoNotOptimize” label should never be touched, *e.g.*, because they contain boolean values or atomic data.¹⁰³ In this paper, only bond and angle parameters with the “Standard” label are considered for optimization.

Finally, some parameters are (de)activated for very specific reasons:

- The atomic parameter r_0^{σ} , which is r_0^{σ} in Eq. (2), for Al is deactivated because it can be overruled by corresponding pair parameters for Al–H and Al–O bonds.
- Because no Al–Al bonds are present, of the Al–Al parameters, only D_e^{σ} is optimized. This introduces some freedom to tune the weak bonding interactions between pairs of Al atoms that are not directly bonded.
- π and $\pi\pi$ bond parameters are deactivated because no such bonds are present in our training data. This includes parameters with labels containing any of the following strings: `pi`, `p_bo3`, `p_bo4`, `p_bo5` or `p_bo6`.
- The following “Expert” parameters were activated to improve the angular energy terms: `p_val3`, `p_val4` and `p_val5`.

These selection criteria result in a subset of 36 activate parameters. For each parameter, lower and upper bounds of suitable values are determined and used to restrict the search space during the parameter optimization. For each parameter, the bounds are set equal to the corresponding range of historical values in the ReaxFF parameter database curated by Software for Chemistry & Materials B.V. (SCM).¹⁰⁰ Subsequently the bounds are extended to also include a window of $\pm 20\%$ around the values from the Joshi *et al.* force field. Note that such choices are subjective for lack of a better alternative: there are no established defaults for the parameter bounds. The list of active parameters and their bounds can be found in Table S3 of the Supporting Information.

2.4 Optimization Settings

ReaxFF parameters are typically calibrated by minimizing a loss function with a numerical optimizer. We have developed a novel loss function for this work, which will be discussed in section 3. Here we focus on the details of the numerical optimization algorithm.

Several optimization algorithms have been proposed to refine ReaxFF parameters. The original method proposed by van Duin was a deterministic algorithm that optimized one

parameter at a time with a parabolic extrapolation.¹¹⁶ More recent algorithms are stochastic, which makes them more robust to the non-trivial structure of a standard ReaxFF loss function, such as many local minima and discontinuities.^{21–25,27} These difficulties arise from the small discontinuities in the ReaxFF energy itself, and the noisy sensitivity of geometry optimizations (while training) to the ReaxFF parameters.^{27,44} These difficulties are still present in this work, and therefore we use a stochastic derivative-free optimizer that has proven its effectiveness, i.e. the Covariance Matrix Adaptation Evolutionary Strategy (CMA-ES).^{27,117–119}

The CMA-ES settings in this work follow the best practices from the literature.^{117–119} The algorithm is repeated 40 times, starting from the Joshi’s parameters, to reduce the risk of getting stuck in an unfavorable local minimum. These repetitions are also used to test the robustness of the new loss function proposed in Section 3. The CMA population size is set to the value recommended by Hansen, $\lfloor 4 + 3 \ln N_{\text{par}} \rfloor = 14$, where $N_{\text{par}} = 36$ is the number of activated force field parameters.^{117–119} ParAMS communicates dimensionless parameters to CMA-ES, by linearly transforming the original parameters so that their bounds all become $[0, 1]$. The initial CMA-ES step size, in these dimensionless parameters, is set to 0.2. This is sufficient to let the algorithm randomize the parameters in the first few CMA iterations, after which it starts to converge, thereby guaranteeing an initial exploration of the parameter space. Each CMA run is terminated after 1000 iterations and the parameters with the lowest loss value are selected for further analysis.

Before evaluating the loss function in each CMA iteration, all structures in the training set are optimized with the parameters generated by CMA. The maximum number of geometry iterations is set to 500, which is much higher than the default value of 30 in ParAMS. For the training set in this work, a lower setting, such as 50, 100 or 200, produces force fields that are overfitted to this lower number of geometry steps. Each CMA run is performed on 18 cores (Intel Xeon Gold 6140), with `ParallelLevels ParameterVectors=14` and `Jobs=2`. This results in a slight over-commitment of the cores, which is normally not recommended, but it

improves the overall efficiency in this case, which can be understood as follows. The CMA-ES algorithm synchronizes after each iteration, resulting in idle time when the members of the population require different CPU times. This is generally the case for ReaxFF, since the number of required geometry steps depends strongly on the parameters. By over-committing the cores, the idle time is reduced, resulting in a more efficient use of resources.

2.5 Validation Set

(i) Structures The validation set is taken from a dataset by Raybaud *et al.*, available on NOMAD, containing alumina structures optimized with VASP, using the same level of theory as the training data,^{52,120} except that a plane-wave cutoff of 400 eV was used. This set contains 53 new γ -Al₂O₃ surface structures not used for parameter optimization, with different numbers of adsorbed water molecules. The surface orientations comprise (001), (111), (110)_ℓ and (110)_b as shown in Fig. 1. The subscripts ℓ and b are used to distinguish between lateral and basal surfaces, respectively, which feature different Brønsted and Lewis acid sites.^{52,76} The set also includes a bulk γ -Al₂O₃ model and an isolated water molecule was added in this work, using consistent VASP settings. A complete list of structures is provided in Table S4 of the Supporting Information.

Recent developments in alumina characterization have revealed an ambiguity in the terminology used in older works. In particular, earlier spinel models considered the (100), (010) and (001) surfaces to be equivalent, but it has recently been shown from non-spinel models that this is not the case.⁵² To remain consistent with published datasets and with the optimizations performed in this work, the notation remains (001) for surfaces with this orientation in the validation set and (100) for surfaces with this orientation in the training set. However, they are structurally equivalent.

(ii) Property Extraction Properties are extracted using the same methodology and classification as described in Section 2.2. The resulting validation set contains 16745 distances,

9513 angles, 101 adsorption energies, and 6 other energies, for a total of 26365 validation targets. Figures S3, S5, S6 and S7 in the Supporting Information show the histograms of these data, whereas Table S5 lists the individual reaction energies. The final force field in this work and the original one by Joshi *et al.*^{88,90} are validated by comparing these geometrical properties and energies to the VASP reference data.

3 Balanced Loss function and optimization workflow

ReaxFF parameters are conventionally calibrated by minimizing a loss function L , which is often a weighted Sum-of-Squares Error (SSE) or Root-Mean-Squared Error (RMSE):

$$L_{\text{SSE}}(\mathbf{x}) = \sum_{i=1}^N w_i s_i(\mathbf{x}) \tag{4}$$

$$L_{\text{RMSE}}(\mathbf{x}) = \sqrt{\frac{1}{N} \sum_{i=1}^N w_i s_i(\mathbf{x})} \tag{5}$$

where s_i are the squared residuals:

$$s_i(\mathbf{x}) = r_i^2(\mathbf{x}) = \left(\frac{y_i - \hat{y}_i(\mathbf{x})}{\sigma_i} \right)^2 \tag{6}$$

and where the sum over i runs over all items in the training set. In every term, the property value y_i is calculated with a reference method (y_i) and ReaxFF (\hat{y}_i). Through the ReaxFF property values, the loss function depends on a vector of adjustable ReaxFF parameter vector \mathbf{x} . Note that CMA-ES is insensitive to the application of any monotonically increasing transformation of the loss function, so from CMA’s perspective, $L_{\text{RMSE}}(\mathbf{x})$ and $L_{\text{SSE}}(\mathbf{x})$ are equivalent.

The constant σ_i is a configurable scaling factor with the same unit as the property of y_i to make the residual r_i dimensionless. In ParAMS, σ_i is only used as a reasonable order of magnitude for the corresponding y_i .¹⁰³ The weight w_i controls the importance of each training

set entry in the total loss function. In principle, one can absorb w_i into σ_i or vice versa. The main motivation for supporting both factors in ParAMS is to cater to different user groups, some of which may prefer one over the other. This may seem surprising, since textbook treatments of the least-squares method do not mention the weights w_i and only introduce σ_i as a measurement error. However, a basic assumption of the standard least-squares method does not hold here: Our data have no measurement errors. Any discrepancies between the training data and ReaxFF are due to systematic errors, mainly in ReaxFF and, in principle, also in the model used to compute the training data.

At first glance, setting the weights seems straightforward: the more important an item in the training set, the higher its weight should be. However, there are different (possibly competing) motivations for adjusting the weights. A first purpose of the weights is to compensate for an imbalance in the training set. For example, our training set contains many more distances and angles than energies, while the energies are also important. This imbalance can be addressed by classifying the data into categories and setting the weight to the inverse of the number of elements in each category. This strategy is common in the context of machine learning potentials, e.g. when atomic forces are much more abundant than molecular energies.³²⁻³⁴ A second purpose of the weights is to emphasize the importance of some residuals. For example, when an initial optimization leads to parameters for which some residuals r_i are perceived to be too large, one may increase the corresponding weights w_i and re-optimize. Assigning different weights to subsets of data is also known in the field of multi-objective optimization as the “scalarization” of multiple objectives into a single loss function.¹²¹ Unlike scalarization methods, multi-objective evolutionary algorithms do not assume any tradeoffs between categories *a priori* and instead find many Pareto-optimal solutions.¹²²

While seemingly intuitive, manual weight adjustment becomes intractable when many weights need to be adjusted differently. Due to the non-linear response of the residuals to the weights,³⁷ multiple combinations of weights must be tried before one reaches the residuals of interest. If the model has insufficient functional flexibility, it may even be impossible to

reach the desired residuals. In addition, when some residuals of interest decrease, others will inevitably increase. It is difficult to predict which residuals will increase and by how much, and this can force the operator to keep adjusting the weights. In practice, this resembles a cat-and-mouse game between weights and residuals. Manually adjusting the weights also provides little insight into the optimization problem: If some residuals are large, there is no straightforward way to understand whether their weights should be increased further, or whether the model is simply unable to reproduce the training data.

It is clear that the development of a training set alone is rarely sufficient to find the optimal parameters. Only if the training data are completely homogeneous, one can simply set all weights equal. This is typically not the case for ReaxFF training set, which contain different types of data, such as distances, angles and energies in this work. Assigning weights to the data is therefore an unavoidable and potentially tedious task before and during a ReaxFF parameter optimization.^{26,35,36}

To simplify the tedious adjustment of weights, we introduce a new method, hereafter called “Balanced Loss”. As will be demonstrated in the results, this method allows for a swift balancing of the training set, and we believe that this methodology will be equally beneficial for other optimization problems facing similar challenges. The Balanced Loss method introduces a new loss function and an intuitive workflow to balance the data and to gain more insight into how well the model can reproduce subsets of the training data.

Balanced Loss requires a classification of the training data into categories. Technically, the categories are C mutually exclusive and exhaustive subsets: $S_c \forall c \in \{1 \dots C\}$. They should be defined so that residuals within a category respond in roughly the same way to a change in the model parameters. For example, one might expect that all O–H bond lengths in a training set, while not exactly the same, do respond similarly to changes in the ReaxFF parameters. With this partitioning, the Balanced Loss function is defined as:

$$L_{\text{BL}} = \tau f^{-1} \left(\sum_{c=1}^C f \left(\frac{R_c}{\tau} \right) \right) \quad (7)$$

where R_c is the RMSE on the entries in category c :

$$R_c = \sqrt{\frac{1}{|S_c|} \sum_{i \in S_c} s_i} \quad (8)$$

L_{BL} is dimensionless by construction. The function f and its inverse must be monotonically increasing functions, and by default $f(x) = \exp(x)$ is used, which will be denoted as the Log-Sum-Exp (LSE) form, referring to the mathematical operations in Eq. (7). To illustrate the benefits of the Log-Sum-Exp form, all parameterizations will be repeated with two other forms of f : $f(x) = x^2$, denoted as Root-Sum-Square (RSS) and $f(x) = x$, denoted as Identity-Sum-Identity (ISI). Note that the RSS form makes Balanced Loss formally equivalent with a standard loss function in Eq. (5), with $w_i = \frac{N}{S_c}$, where c is the category to which training set item i belongs.

By default, L_{BL} is thus a Log-Sum-Exp function, a well-established smooth approximation of the maximum over multiple inputs. It is popular in the machine learning context¹²³ and it has been used for scalarization of multi-objective problems.¹²⁴ Here, the inputs to Log-Sum-Exp are all the R_c values. The hyperparameter τ , sometimes called the effective temperature, controls the smoothness of the approximation of the maximum. In the ‘‘cold’’ limit $\tau \rightarrow 0$, Log-Sum-Exp loses its smoothness and reduces to the maximum over all R_c . The parameter τ appears in two places, such that $L_{\text{BL}} = L_{\text{RMSE}}$ in the trivial case of one category and $w_i = 1 \forall i$. Throughout this paper we have used $\tau = 1$.

Unlike L_{SSE} and L_{RMSE} , user-defined weights w_i are missing from L_{BL} , which implies that σ_i must play a slightly different role. We propose to set each σ_i to the desired accuracy of the corresponding entry y_i in the training set, which resembles its meaning in conventional least-squares methods. To make the distinction with σ_i in other contexts, we call them ‘‘tolerances’’ in the context of Balanced Loss, because they represent the magnitudes of residuals one is willing to tolerate. At this stage, simply defining tolerances may seem like wishful thinking, but it will become clear later that Balanced Loss helps finding a consistent set of ReaxFF

parameters and tolerances. Our definition of σ_i (as the desired accuracy) also facilitates the interpretation of R_c : It expresses, in the RMS sense, the average ratio between the actual and the desired accuracy. In the ideal case, after optimizing the parameters, one obtains $R_c = 1 \forall c$.

Given the interpretation of R_c , the Log-Sum-Exp form of Balanced Loss is easily motivated. If one of the R_c values is much higher than all others, one finds $L_{\text{BL}} \approx R_c$, *i.e.*, category c dominates the loss function. If the optimization algorithm explores a region of the parameter space where category c dominates, it will focus only on reducing R_c , with other categories acting at best as a form of regularization. This is a desirable feature, since category c is then the worst reproduced subset of the training data, and therefore deserves the optimizer’s full attention.

One may also understand the effect of Log-Sum-Exp by comparing the gradients of L_{BL} and L_{RMSE} with respect to the ReaxFF parameters:

$$\frac{\partial L_{\text{BL}}}{\partial x_k} = \sum_{i=1}^N \frac{\partial L_{\text{BL}}}{\partial s_i} \frac{\partial s_i}{\partial x_k} \quad (9)$$

$$\frac{\partial L_{\text{RMSE}}}{\partial x_k} = \sum_{i=1}^N \frac{\partial L_{\text{RMSE}}}{\partial s_i} \frac{\partial s_i}{\partial x_k} \quad (10)$$

Both loss gradients are linear combinations of the gradients of squared residuals, $\frac{\partial s_i}{\partial x_k}$, but they combine them with different “weights”:

$$\frac{\partial L_{\text{BL}}}{\partial s_i} = \frac{\exp\left(\frac{R_d}{\tau}\right)}{\sum_{c=1}^C \exp\left(\frac{R_c}{\tau}\right)} \frac{\tau}{2|S_d|R_d} \quad \text{with} \quad i \in S_d \quad (11)$$

$$\frac{\partial L_{\text{RMSE}}}{\partial s_i} = \frac{w_i}{2NL_{\text{RMSE}}} \quad (12)$$

In the case of L_{RMSE} , the weight $\frac{\partial L_{\text{RMSE}}}{\partial s_i}$ is simply proportional to the user-defined weight

w_i . For Balanced Loss, however, the weight $\frac{\partial L_{\text{BL}}}{\partial s_i}$ contains a new and crucial factor:

$$P_d = \frac{\exp \frac{R_d}{\tau}}{\sum_{c=1}^C \exp \frac{R_c}{\tau}} \quad (13)$$

with

$$\sum_{d=1}^C P_d = 1. \quad (14)$$

This factor is known as SoftMax, a continuous generalization of the ArgMax function, used to identify the position of a maximum in an ordered list.¹²⁵ This shows how Balanced Loss borrows a strategy from reinforcement learning, known as the Gradient Bandit Algorithm: At each iteration in the optimization, the most violated subset of the training data determines the action,¹²⁶ in this context action being the direction in which the parameters must evolve. The analogy between P_d (in L_{BL}) and the user-defined weights w_i (in L_{RMSE}) also suggests another interpretation. Instead of a human operator tuning the weights w_i , as in the cat-and-mouse metaphor introduced above, Balanced Loss adjusts the weights algorithmically within a single optimization run.

So far, we have assumed that one simply sets the tolerances σ_i to the desired accuracy of the corresponding y_i . However, such a choice may be subjective and incompatible with the capabilities of the ReaxFF model to be trained. In practice, we recommend such “naive” tolerances σ_i as a first guess. Parameter optimization can then be used to test these expectations. To do so, we recommend the following workflow:

W1. First gather all the elements of a conventional parameter optimization: (i) the model, (ii) the training data, (iii) a selection of parameters to optimize and their bounds, (iv) an initial guess of the parameters, and (v) an optimization algorithm. In this paper, all these elements are described in Section 2.

W2. Then define the additional elements needed for Balanced Loss: the categories of train-

ing data and an initial configuration of the tolerances σ_i . Such choices are domain-specific, but a few general recommendations can be given, in addition to the ones discussed above. It is convenient to have data with consistent units within one category c and to assign the same tolerance to all its members, for which the symbol σ_c will be used below. Furthermore, it is useful to introduce categories for data that deserve special attention, e.g. with key properties for the intended application of the force field, or with properties that are harder to reproduce than others. By placing these data in separate categories, their RMSEs are easily monitored and large errors within these categories will be prioritized during the optimization.

For ReaxFF, one can introduce different categories for distances, angles and energies. In this paper, the categories are more fine-grained: All internal coordinates are classified by the chemical elements and the bond types involved. In fact, we categorize all training data as they were introduced in Section 2.2: the 4 bond categories are Al–O, Al–Al, O–H and O \cdots H, the 6 angle categories are O–Al–O, Al–O–Al, Al–O–H, Al–O \cdots H, H–O \cdots H and H \cdots O \cdots H, and the energy categories are **BSH**, **GEH**, **GSH**, **SUR** and **FOR**. Note that a regular covalent bond is denoted by minus sign (–) and a hydrogen bond by three dots (\cdots). The tolerances σ_c will be described in Section 4.

W3. Finally, minimize the Balanced Loss function and analyze the R_c values of the optimal parameters. When one category keeps dominating the loss function throughout the optimization, the only possible explanation is that the corresponding tolerances σ_c were set too small. There is no way to lower R_c because L_{BL} already ignores all other categories. The only option left is to accept that the model cannot reproduce items in category c with the desired accuracy, and to adjust one’s expectations by increasing the corresponding tolerances σ_c . One can now repeat the parameter optimization and re-evaluate the result, possibly repeating the exercise a few times. Unlike tuning the weights in a conventional loss function, these repeated optimizations provide insight:

They inform the human operator about the capabilities of the model and help manage expectations. It may also happen that some R_c end up well below 1, in which case we do not recommend decreasing the corresponding σ_c . Such a fortuitous outcome should not affect the desired accuracy.

Note that steps W2 and W3 in the above workflow involve (possibly subjective) human decisions, and therefore cannot be replaced by an autonomous algorithm. This is an unavoidable aspect of multi-objective problems: One has to decide on a compromise between different categories. The overall goal of Balanced Loss is to facilitate finding suitable compromises.

4 Results and Discussion

4.1 Balanced Loss Optimization Procedure

This section illustrates how the optimization workflow of Balanced Loss leads to a competitive ReaxFF parameterization, using the alumina training set as a realistic example. In addition to the final force field, the intermediate steps provide insight into the capabilities of ReaxFF.

Table 2: Tolerances used in the Balanced Loss optimization

Category	Unit	Initial σ_c	Final σ_c
Al-O	Å	0.05	0.07
Al-Al	Å	0.05	0.10
O-H	Å	0.05	0.05
O...H	Å	0.05	0.12
Al-O-Al	deg	2.0	5.0
Al-O-H	deg	2.0	5.0
O-Al-O	deg	2.0	5.0
Al-O...H	deg	2.0	7.0
H-O...H	deg	2.0	7.0
H...O...H	deg	2.0	7.0
BSH	kcal mol ⁻¹	1.25	4.0
GEH	kcal mol ⁻¹	1.25	4.0
GSH	kcal mol ⁻¹	1.25	4.0
SUR	kcal mol ⁻¹	1.25	3.0
FOR	kcal mol ⁻¹	1.25	3.0

The data in the training set, described in Section 2.2, have been grouped into categories as described in Section 3 and as summarized in the leftmost column of Table 2. The optimizations are carried out in two stages, initial and final, which differ only in the tolerances σ_c .

Each entry is given an initial chemically relevant tolerance, σ_c , equal to the default sigma value from ParAMS, as shown in Table 2. With these tolerances, the ReaxFF parameters were optimized 40 times using different random seeds to produce independent solutions. Figure 2(a) shows the evolution of the Balanced Loss during the 40 CMA runs. Figure 2(c) presents the $R_c\sigma_c$ values (category RMSEs with units) for the 40 optimized parameter vectors. The curves and data points are colored according to the loss value of the best parameter vector of each run. Of the 40 CMA runs in the initial stage, two are clearly worse than all others, presumably converging to unfavorable local minima. All 38 remaining runs produce comparable RMSE values, but are not identical, which is the expected behavior. ReaxFF loss functions are known to exhibit many local minima and apparent noise due to high sensitivity of the geometry optimizations in the training set to the ReaxFF parameters.²⁷ Adsorption energies in the categories **BSH** and **GSH** are the highest relative to their tolerance, σ_c . The performances in all other categories have less effect on the optimized parameters, simply because these errors are closer to their tolerance. This means that, in this initial stage, the CMA runs train almost exclusively on the adsorption energies. It is therefore highly unlikely to find ReaxFF parameters that can further lower RMSE on the adsorption energies, let alone reach the tolerance of $1.25 \text{ kcal mol}^{-1}$. Also, for all other categories, the initial tolerances seem too optimistic, which will be addressed in the next stage.

For the second (and final) stage, the tolerances are revised, as shown in the last column of Table 2, to be more consistent with what ReaxFF could achieve in the initial stage. Without Balanced Loss, these tolerances can only be set by expert judgment, which is greatly facilitated here by the feedback from the initial stage. Figure 2(b) shows that the revised tolerances result in more consistent loss values across all 40 parameterizations. This

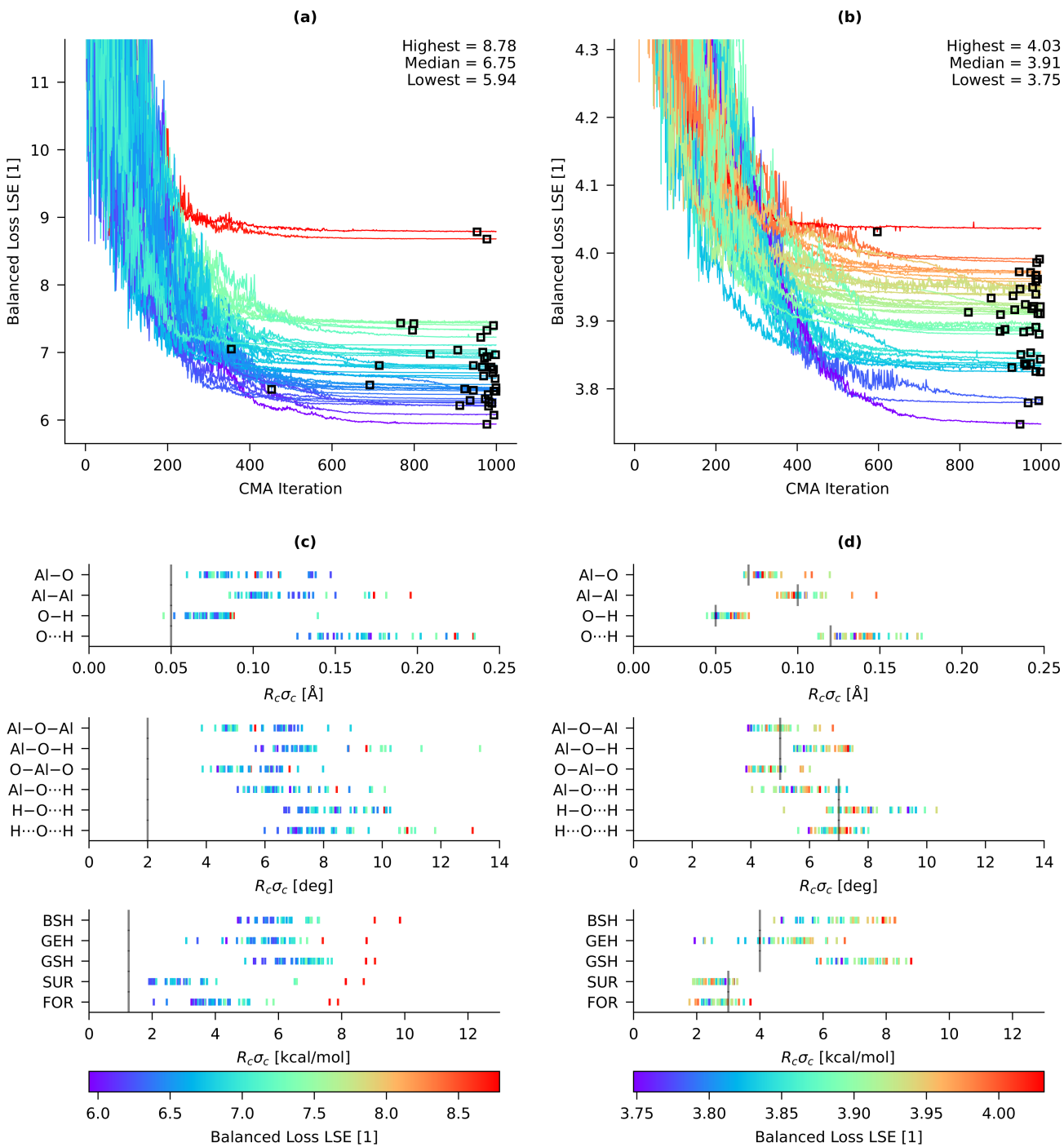


Figure 2: The Balanced Loss as a function of CMA iteration (lowest value within the population) of the 40 parameterizations in the initial (a) and final (b) stage. The lowest value along each trajectory is indicated by a black square. The dimensioned category RMSEs, $R_c\sigma_c$, of the best parameter vector of each of the 40 parameterizations in the initial (c) and final (d) stage. All data are color coded by the loss value of the best point along the trajectory. The color bar of panel (c)/(d) is also applicable to panel (a)/(b). Grey vertical lines in panel (c)/(d) denote the tolerances for the corresponding category.

is also reflected in the RMSEs in Figure 2(d), most of which exhibit less scatter. In other words, for most categories, the 40 parameterizations in the final stage are comparable, with the category **GEH** being the most notable exception. Note that the absolute value of the Balanced Loss values cannot be compared between Figures 2(a) and 2(b), because the two optimization stages use different tolerances. One could slightly tweak the tolerances further to bring them closer to the errors on the training set, but this would amount to relatively small adjustments that we do not expect to lead to significant improvements.

To illustrate the importance of the Log-Sum-Exp form of Balanced Loss, we have performed the 40 CMA optimizations in six different ways: with initial and final tolerances and using different functions f : $f(x) = \exp(x)$ (Log-Sum-Exp or LSE, the default, same results as above), $f(x) = x^2$ (Root-Sum-Square or RSS) and $f(x) = x$ (Identity-Sum-Identity or ISI). For comparison, the LSE form of Balanced Loss is computed for all the 240 optimized parameter vectors, and their distribution is shown in Figure 3(a). In the initial stage, the function f has a significant influence. The choice of the function f determines the compromise between the RMSEs of the individual categories: In the case of RSS and ISI, the parameterization no longer exclusively prioritizes the adsorption energies in the categories **BSH** and **GSH**, resulting in higher RMSEs for these categories, as illustrated in Figure 3(b). The results in this figure do not reveal whether the poor performance of ReaxFF for the categories **BSH** and **GSH** can be remedied by giving these categories a higher weight in the loss function, or whether they are high due to intrinsic limitations of the model. The Log-Sum-Exp form automatically resolves this ambiguity. Since this form approximates the maximum over all R_c , this loss function is dominated by the categories **BSH** and **GSH**, resulting in the lowest possible RMSE for these categories. It is simply impossible to give these categories a higher weight, leaving no other option than to assign more humble tolerances.

Figure 3(a) reveals two additional insights. First, the results become less sensitive to the choice of the function f in the final stage. The RMSEs for all categories are close to the final tolerances, meaning that the argument of the function f (for the optimized parameters)

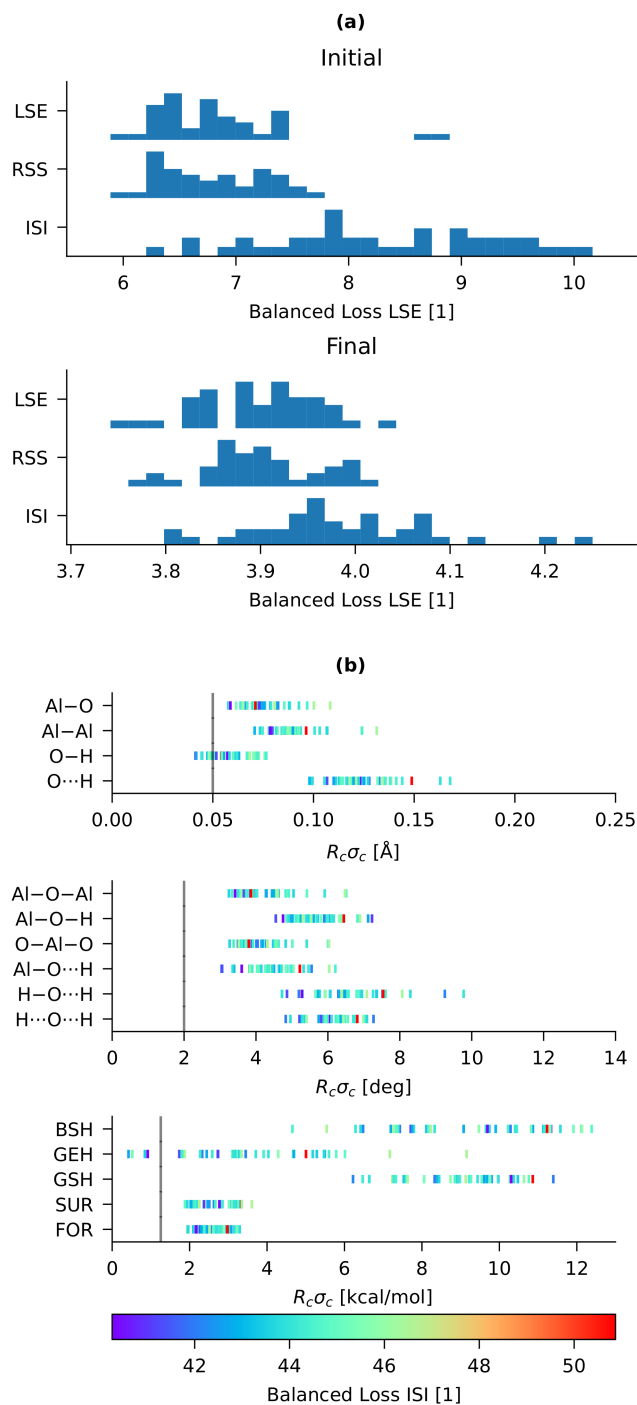


Figure 3: (a) Distribution of Balanced Loss values, computed with $f(x) = \exp(x)$, for parameter vectors optimized with different functions f in Eq. (7): $f(x) = \exp(x)$ (LSE), $f(x) = x^2$ (RSS) and $f(x) = x$ (ISI). The histograms are computed for both the initial and final tolerances defined in Table 2. (b) The dimensioned category RMSEs, $R_c\sigma_c$, of the best parameter vector of each of the 40 parameterizations in the initial stage using $f(x) = x$ (ISI).

is close to one, reducing the importance of the non-linearity of f . Second, with $f(x) = x^2$ (RSS), the loss function is mathematically equivalent to Eq. (5), a standard loss functions used for ReaxFF. This implies that the optimized parameters in this work can also be found with a more conventional loss function, when the weights and sigmas are set consistently with the tolerances in Balanced Loss. Hence, the added value of Balanced Loss is essentially the feedback provided from the initial stage, which facilitates the configuration of the tolerances.

Figure 4 shows the distribution of the 40 optimized parameter vectors, after transforming them to their dimensionless form. Although the 40 CMA runs converge to approximately the same Balanced Loss value, the corresponding parameters are not necessarily similar. Some parameters, such as `Al.0:D_e^sigma` or `Al.0:p_ovun1`, have a delineated range of optimal values. However, most parameters can be found across the entire interval of allowed values. This does not mean that all these parameters are completely random: They could be correlated, which is not apparent in the individual histograms. In any case, the optimal parameters are degenerate to some degree, which has also been observed in previous ReaxFF parameterizations on other chemical systems.^{21,27,31,44}

Since ReaxFF is at least partially inspired by physical principles, one might hope that all parameters always converge to the same values. However, Sethna *et al.* have extensively shown in their work on “sloppy models” that broad parameter distributions are virtually always found for models with more than a few parameters, across different scientific disciplines.^{127–130} This is a universal pattern, regardless of the degree of physical interpretation that the model parameters may have. It is observed that some degrees of freedom in the parameter space of complex models are systematically ill-defined, not due to a lack of data, but because nearly the same model predictions (for all possible inputs) are found for different parameter vectors. As a consequence, predictions on unseen data are robust, despite uncertainties in the parameters. For the Electronegativity Equalization Method (EEM), which is included in ReaxFF, this parameter degeneracy has been investigated in more detail.¹³¹ ReaxFF also has the characteristics of “a sloppy model”, as illustrated by Figure S8 in the

Supporting Information: All the optimized parameter vectors of the 40 CMA runs (LSE, final stage) perform reasonably well for the validation set, despite the fact that they represent different local minima in the parameter space. This in itself is not a limitation when the model is used for simulations, but it obviously makes any direct interpretation of the parameters impossible.

It is also noticeable that several parameters have a high probability of converging close to the bounds. One might deduce that the parameter bounds are too narrow and the optimizer is trying to move the parameters to an optimum beyond the bounds, but this is not the only possible cause. Note that the components of the best parameter vector over all 40 runs, the circles in Figure 4, are not necessarily close to the bounds, even if the remaining near-optimal values cluster near the edges. Examples of this pattern are “Al.O:p_be1” and “Al.O.H:Theta_0,0”. A deeper investigation, beyond the scope of the current work, is needed to understand why a disproportionate number of near-optimal solutions is found near the bounds. For example, this could also be related to an optimizer inefficiency when the parameters approach their bounds, and addressing this problem may make the optimization more efficient. It should also be noted that some initial parameter values start off close to the interval bounds regardless of the boundary extension as explained in Section 2.3. Since some of the initial parameters have values close to zero, the effect of the boundary extension is negligible. The most prominent examples are “Al.O:p_be2”, “Al.H.O:p_val1”, “Al.H.O:p_val2” and “Al.O.H:p_val2”.

For the remainder of this work, the best parameter vector from the final stage is used for all calculations, i.e. corresponding to the lowest square in Figure 2(b) and the circles in Figure 4. The selected parameters are given in the last column of Table S3 in the Supporting Information.

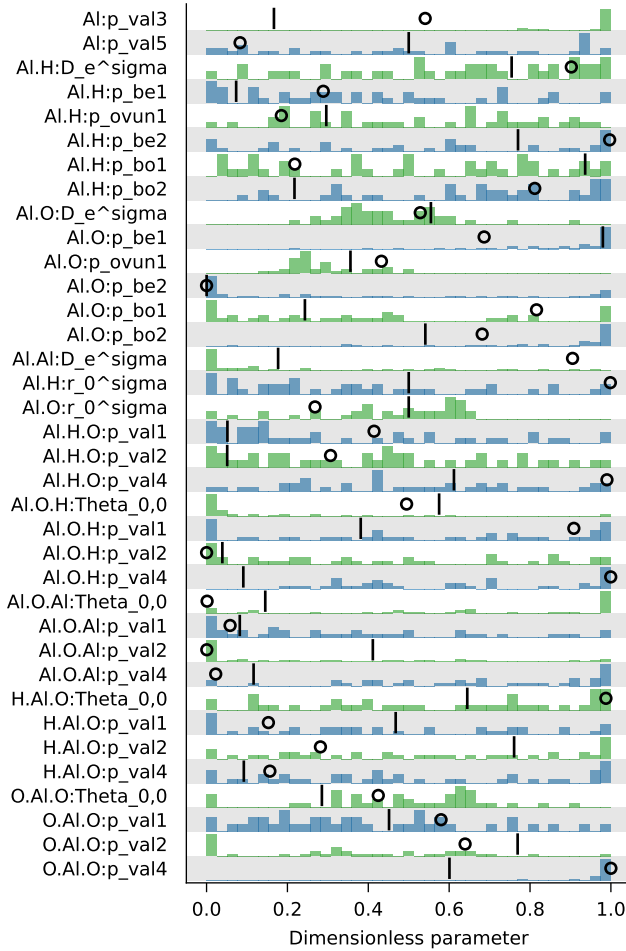


Figure 4: Histograms of the 36 components of the 40 optimized dimensionless parameter vectors in the final stage. The parameter components are made dimensionless by a linear transformation, such that zero corresponds to the lower bound and one corresponds to the upper bound. The bounds are listed in Table S3 in the Supporting Information. The initial values are marked with vertical black bars. The values corresponding to the lowest loss (over all 40 runs) are marked with circles.

4.2 Force field validation

Figure 5 offers a first visual impression of how the new force field improves the prediction of dissociative water adsorption on alumina. It shows a high-hydration structure of the γ -Al₂O₃ (001) slab model, labeled `gamma_surf-001_03w` in the validation set, geometry-optimized with the reference method (DFT calculation with VASP), the initial force field by Joshi *et al.*⁹⁰ and the new force field in this work. The Joshi *et al.* force field predicts a severe deformation of the alumina structure, and already desorbs water molecules in this static calculation while all water should be adsorbed according to reference calculation. In contrast, the new force field in this work predicts a geometry that is visually deviating only slightly from the DFT reference, and the water molecules remain adsorbed on the surface.

The performance of the new force field can be evaluated more in detail by analyzing the distributions of categorized data in the training and validation sets, and their deviations from the DFT reference. Table 3 shows the RMSEs between force field and reference data, for each category, for the training and validation set, and for the initial force field by Joshi *et al.*^{88,90} and the one optimized in this work. To make the RMSEs directly comparable, only data related to γ -Al₂O₃ were taken from the training set since the validation set also contains only γ -Al₂O₃. In addition, only data categories (rows) are included that exist in both data sets. For reference, also the standard deviations on the reference data per category are reported. Figure 6 shows parity plots for all categories of internal coordinates in the validation set. In addition, water adsorption energies on γ -Al₂O₃ surfaces in the training and validation sets are shown in Figure 7. Not all data categories from the training set exist for the validation set, because the validation set is focused on adsorption on γ -Al₂O₃ only. This is reflected in the Table 3, Figure 6 and Figure 7 by only considering γ -Al₂O₃ structures. Table S6 and Figure S3 in the Supporting Information contain the results omitted here, i.e. not involving γ -Al₂O₃ surfaces, for which a direct comparison to the validation set is not possible.

The RMSEs in Table 3 show that new force field significantly reduces the errors on the bond lengths compared to the Joshi *et al.* force field.^{88,90} A subset of the bonds is broken after

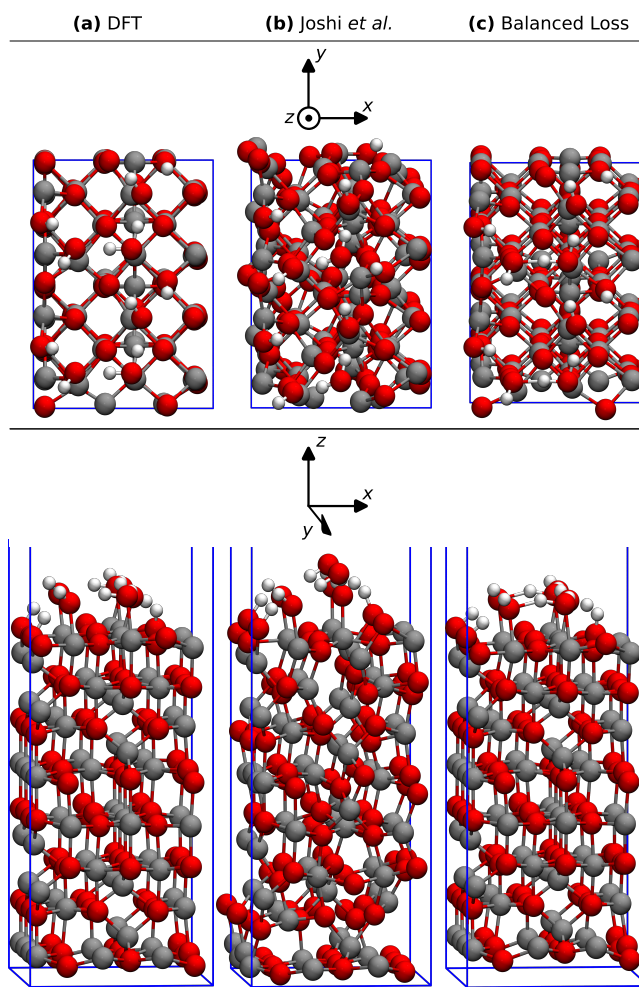


Figure 5: Optimized structures of the γ -Al₂O₃ (001) surface from the validation set at an OH coverage of 13.0 nm⁻², computed with different models: (a) DFT reference, (b) ReaxFF parameters by Joshi *et al.* and (c) ReaxFF parameters obtained with Balanced Loss. Al=gray, O=red, H=white.

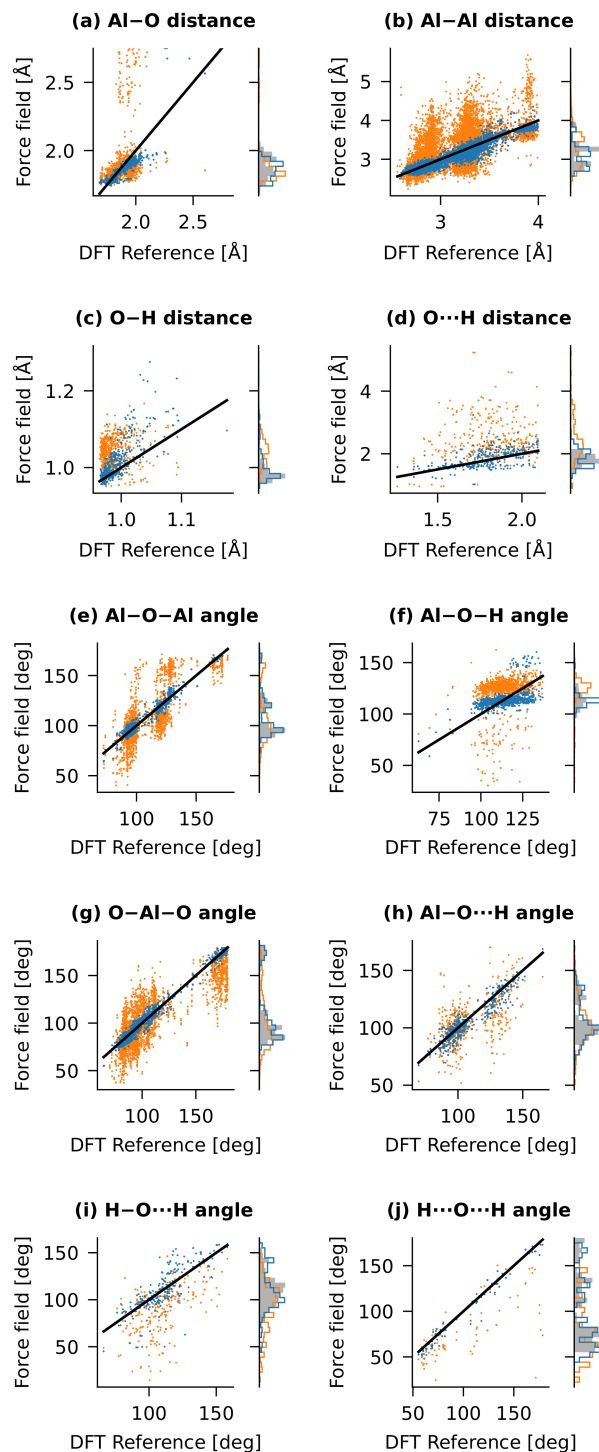


Figure 6: Parity plots of the reference internal coordinates from the validation set versus the force field predictions: initial parameters by Joshi *et al.*^{88,90} (orange) and optimal parameters obtained with Balanced loss (blue). Distances: (a) Al–O, (b) Al–Al, (c) O–H and (d) O···H. Angles: (e) Al–O–Al, (f) Al–O–H, (g) O–Al–O, (h) Al–O···H, (i) Al–O···H and (j) Al···O···H. The parity line is plotted as a black solid line. In panels (a) and (c) the vertical axis is manually limited to only show bonded distances. The initial parameters from Joshi result in many broken bonds, which are omitted for the sake of clarity.

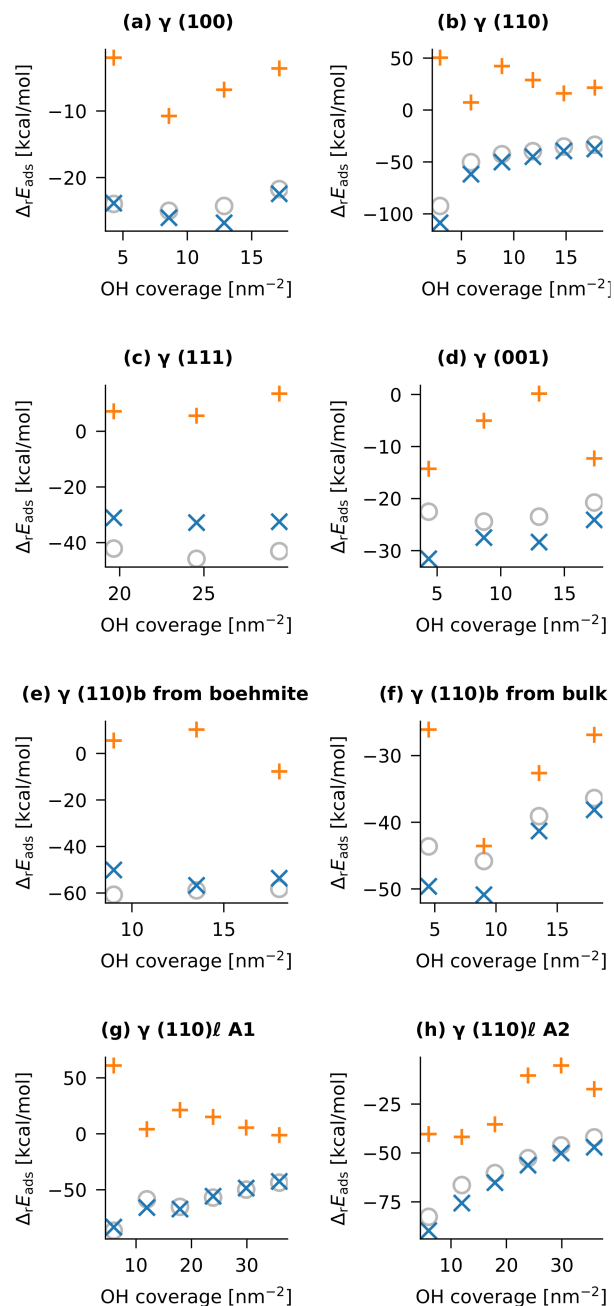


Figure 7: Water adsorption energy per water molecule on $\gamma\text{-Al}_2\text{O}_3$ surfaces as a function of the OH coverage, using the bare surface as the reference, i.e. using $m_i = 0$ in Eq. (3). Results are computed with DFT (gray circle), Joshi FF (orange plus), FF from this work (blue cross). Panels (a) to (c) are adsorption energies from the training set, whereas (d) to (h) are derived from the validation set. The nomenclature of the surfaces in the validation set is described in Ref. 52.

Table 3: Comparison of root-mean-square-errors (RMSEs) of the initial force field by Joshi *et al.*^{88,90} and the force field optimized in this work (BL). The RMSEs are computed for training and validation sets and are grouped per data category. For reference, the standard deviation (SD) on the reference data is included.

Category	Unit	Training				Validation			
		Ref. SD	Joshi RMSE	BL RMSE	#	Ref. SD	Joshi RMSE	BL RMSE	#
Al–O	Å	0.16	0.45	0.09	1405	0.10	0.40	0.06	2102
Al–Al	Å	0.30	0.40	0.11	6759	0.31	0.40	0.11	13588
O–H	Å	0.03	0.31	0.07	352	0.02	0.18	0.06	704
O···H	Å	0.18	0.85	0.17	203	0.18	0.90	0.25	351
Al–O–Al	deg	21.2	17.0	4.4	1756	20.0	16.6	3.8	2744
Al–O–H	deg	12.2	20.4	6.9	598	9.3	18.7	8.3	1217
O–Al–O	deg	29.4	16.7	4.5	2943	30.9	17.4	3.9	4656
Al–O···H	deg	18.4	16.9	6.5	301	17.6	17.6	6.6	554
H–O···H	deg	17.5	27.4	12.7	142	17.3	29.4	14.7	254
H···O···H	deg	31.1	28.9	4.4	65	38.0	33.7	7.7	88
GSH	kcal mol ⁻¹	15.0	55.7	6.6	37	16.4	54.4	8.3	101
SUR	kcal mol ⁻¹	6.1	11.3	2.9	8	1.4	4.7	1.4	6

geometry optimization with the force fields, which is not fully visible in Figures 6(a) and 6(c), because this would require an impractical scale for the vertical axes. In the validation set, 14.3% of the Al–O bonds and 1.1% of the O–H bonds are broken with the Joshi *et al.* force field. With the new force field proposed here, these percentages reduce to 0.0% and 0.3%, respectively. These percentages are consistent with the visualization in Figure 5(b) and confirm that the Joshi γ -Al₂O₃ surfaces force field cannot preserve the structural integrity of the (hydrated) γ -Al₂O₃ slabs. By consequence, this force field also performs poorly for other categories (angles and energies), for which a correct bonding topology is required.

The parity plots of the distances in Figures 6(a), 6(c) and 6(d) also reveal that even the new force field captures the variations in bond lengths only approximately. This is also confirmed by the fact that the RMSEs of the distances in Table 3 are of the same order as the standard deviation on the distances in the reference data. For the O–H and O···H distances, this was to be expected, because the corresponding bond parameters in ReaxFF were not re-optimized for the sake of compatibility with the silicate parameters in the Joshi *et*

al. force field. For the Al–O distances, the performance is slightly better, which is consistent with the fact that several Al–O parameters were re-optimized.

The new force field also improves upon the Joshi *et al.* force field in terms of valence angles, again with a somewhat better performance when no hydrogen atoms are involved. It is remarkable that the multimodal distributions of the Al–O–Al, O–Al–O and Al–O···H angles are reproduced well by the new force field, despite only having a single energy term for these angles in the ReaxFF force field. Also the improvements of the H–O···H and H···O···H angles, compared to the initial force field, are remarkable, because no corresponding valence angle of hydrogen bonding terms were reparameterized.

In line with the previous categories, also the RMSEs on the energies are significantly smaller with the new force field. Before discussing the adsorption energies, it should be noted that the category **SUR** was mainly introduced to improve the diversity of the training set. (It comprises reaction energies between bulk and slab models, normalized on the number of Al atoms.) A few data points in the same category can be derived from the validation structures and are included here for the sake of completeness. The error on these data points has also decreased compared to the initial force field, confirming the ability of Balanced Loss to account for underrepresented categories in the training set.

The new force field reduces the error on the adsorption energies (category **GSH**) by more than a factor 6 in the validation set. The improvements are also immediately clear in Figure 7, which shows the adsorption energy on γ -Al₂O₃ surfaces as a function of OH coverage. In most cases, the new force field predicts the correct trends in the adsorption energy, with some exceptions at low OH coverage in Figures 7(d) and 7(f). For the (001) and the (110)_b slabs in the validation set, it is unclear why these surfaces exhibit larger errors in adsorption energy at low coverage. The Joshi *et al.* force field incorrectly predicts water desorption for 12 out of 53 surface structures in the validation set, which hampers reliable energy predictions. With the new force field, this problem is far less prevalent: Only one water molecule (out of six) from only one surface structure spontaneously desorbs. The new force field can also

predict the magnitude of the adsorption energy, with an RMSE of $8.3 \text{ kcal mol}^{-1}$, compared to a standard deviation of $16.4 \text{ kcal mol}^{-1}$ of the adsorption energies in the validation set.

For all categories of data discussed above, the errors on static calculations are very similar for the training and the validation sets, indicating that the significant improvements of the new ReaxFF force field generalize to structures not used for training. The errors on distances, valence angles and energy differences are also comparable to those reported for previous ReaxFF models.^{8,25,132–135}

Because the training set only includes equilibrium geometries, it should be tested to what extent the new parameters can also reproduce non-equilibrium energies. To this end, a constant-temperature DFT molecular dynamics run was performed on structure `gamma_surf-1101_A1_06w` from the validation set, using the same level of theory as the training data. An elevated temperature of 1000 K stimulates the desorption of water, which is observed during the first 200 fs. Section S2 of the Supporting Information presents a detailed comparison of the DFT and ReaxFF energies computed for snapshots from this trajectory. In summary, the instantaneous DFT adsorption energy computed with Eq. (3) as a function of time is reproduced qualitatively by the ReaxFF parameters obtained with Balanced Loss: The relative error of about 25 % over the first 200 fs is comparable to the RMSE on the training set for GSH category. Our new parameters also show a clear improvement compared to the ReaxFF energies obtained with the parameters of Joshi *et al.* The thermal energy fluctuations due to vibrations within the alumina slab are not well reproduced, which is expected, since no corresponding data was used for training.

Despite our improvements, it remains interesting to explore further refinements, e.g. to further reduce errors in adsorption energies or to improve the vibrational states of alumina. One avenue is to activate more parameters during the training that are now fixed for the sake of backward compatibility. Giving up backward compatibility would only be useful when extending the chemical space of the training set to aluminosilicates and water, such that all parameters of the Joshi *et al.* force field can be re-optimized. However, this would

be a daunting enterprise, because the current training set size is already computationally demanding: A single CMA run in this work already took more than 24 hours. In addition to the increased cost of the training set, more active parameters also imply more local minima and a slower convergence of CMA-ES, further exacerbating the computational cost. This avenue is therefore only feasible when one can drastically speed up the training of ReaxFF parameters. It is encouraging that efficiency gains were reported in recent publications, e.g. by parallel optimization management,⁴⁴ or by machine learning surrogates of the loss function.^{28,136,137} One may also reduce the dimensionality of the parameter space through sensitivity analysis to speed up the CMA runs.³¹

As a final check of the new force field, a molecular dynamics (MD) simulation is performed on $(110)_\ell$ γ - Al_2O_3 slab with a cross section of 6.0 nm^2 , a thickness of 1.8 nm and surrounded by a vacuum layer of 5.7 nm wide. In the initial structure, the maximal number of water molecules is dissociatively adsorbed on both sides of the slab, such that the chemical formula is $\text{Al}_{504}\text{O}_{864}\text{H}_{216}$. The MD simulation follows a NVT -ensemble and uses a Nosé-Hoover thermostat¹³⁸ with a time step of 0.2 fs , a temperature of 500 K , a time-constant of 500 ps and a fixed periodic box size. Figure 8 shows the initial and final states of the MD trajectory, as well as the evolution of the kinetic energy, total energy (kinetic + potential) and the conserved quantity. The conserved quantity (green) exhibits a slow linear increase, which is acceptable for long ReaxFF MD simulations at a constant temperature. ReaxFF forces are imperfect due to numerical convergence of the variable charges and small discontinuities in the ReaxFF energy surface. Such small force errors are practically tiny random kicks on the nuclei, which slowly pump energy into the system, but this is easily compensated for by the thermostat and results in a slowly increasing conserved quantity. The 3D visualizations show that some of the water molecules desorb, as expected at a temperature of 500 K . This test shows that the new force field can also be used for MD simulations, even though it is only trained on optimized geometries. A complete study of water adsorption, with larger slabs, different alumina surfaces and temperatures, goes beyond the scope of this

work. We expect that the new force field will make such simulations possible, at time and length scales that are infeasible for DFT methods.

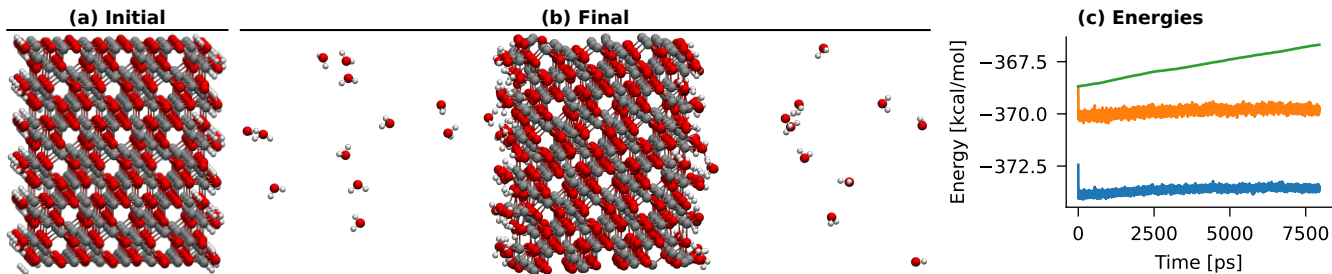


Figure 8: The initial (a) and final (b) states of a constant-temperature MD trajectory of a $(110)_\ell \gamma\text{-Al}_2\text{O}_3$ with water initially adsorbed on the surface. Al=gray, O=red, H=white. See text for details. (c) The kinetic energy (blue), total energy (kinetic + potential, orange) and the conserved quantity (green).

5 Conclusion and Outlook

This work addresses the difficulty of assigning fitting weights (or their inverses, often called sigmas) in a conventional ReaxFF loss function. Balanced Loss is proposed as a new cost function as well as a workflow to reformulate the weight assignment in terms of more manageable concepts. One starts by classifying the training data into meaningful categories with a corresponding tolerance, which is the root-mean-square error (between ReaxFF predictions and reference data in that category) that one is willing to tolerate. When the error on one category exceeds the corresponding tolerance more than other categories, the Log-Sum-Exp form of Balanced Loss guarantees that this error will completely dominate the loss function, effectively forcing the optimizer to reduce this error first. If one or more of such dominating categories remain after the parameters converge, it is guaranteed that these errors cannot be reduced further at the expense of making larger errors in other categories. As a result, the parameter optimization also assesses whether ReaxFF can meet the expectations defined by the tolerances. If necessary, the expectations can be adjusted, followed by a new parameter optimization. The methodology is applied to a realistic and challenging reparameterization

of ReaxFF for water adsorption on alumina surfaces. This not only results in a competitive force field, but also provides insight into the performance that can be expected from ReaxFF for each category of training data.

The new force field derived in this work is a refinement of the alumina parameters in the aluminosilicate force field of Joshi *et al.*^{88,90} The training and validation data consisted of geometry and energy data from previous Density Functional Theory (DFT) studies of water adsorption on boehmite and γ -Al₂O₃ surfaces. While γ -Al₂O₃ is industrially the most relevant, boehmite structures were included in the training set to improve the data diversity. Parameter selection focused on maintaining backward compatibility with the ReaxFF model of Joshi *et al.* as much as possible, while still activating sufficient parameters to reproduce the training data. Covariance Matrix Adaptation (CMA) is used to minimize Balanced Loss as a function of the selected parameters. 40 independent CMA runs were performed to test the robustness of the optimized parameters. Of all these runs, the result with the lowest error on the training set is used for validation. Static calculations confirm that the optimized force field produces very similar errors on the γ -Al₂O₃ properties present in the training and validation sets. The force field can be used for MD simulations, and we expect it to be applicable to extensive simulations of water adsorption on alumina surfaces, at time and length scales inaccessible to DFT methods.

This study also revealed several challenges and new avenues for future method development. Obviously, it should be validated whether the Balanced Loss workflow is equally helpful for other ReaxFF parameterizations. Even beyond the scope of ReaxFF, Balanced Loss may facilitate optimization problems involving multiple (possibly competing) categories of training data. In addition, this study confirmed known pitfalls of ReaxFF parameterization and suggested new ones. Despite our careful and relatively small selection of parameters, the minimum of the loss function is still degenerate, suggesting that the number of active parameters can be reduced further with a sensitivity analysis. Finally, it was observed that parameters often converge to near-optimal values close to the bounds. A better understand-

ing of this phenomenon may help to speed up the convergence to better parameters.

6 Data and Code availability

A data set as made available at <https://doi.org/10.5281/zenodo.10491516> comprising: the training and validation data, the results of the 240 CMA optimizations, and scripts used to select parameters, convert datasets and perform the training and validation.

Acknowledgement

The authors thank the company Software for Chemistry & Materials B.V. (SCM) for providing an AMS developer license at no cost. In particular, we are grateful to Matti Hellström and Tomáš Trnka from SCM for their technical support. The authors also thank members of the Center for Molecular Modelling at Ghent University, especially Tom Braeckvelt, Leonid Komissarov and Michael Gustavo as well as Pascal Raybaud from IFP Energies nouvelles for the insightful discussions. Computational resources and services used were provided by Ghent University (Stevin and Hortense Supercomputer Infrastructures), the VSC (Flemish Supercomputer Center), funded by the Research Foundation-Flanders (FWO), and IFP Energies nouvelles (ENER440). Funding was provided by IFPEN and UGent (BOF/24J/2023/121). T.V. Acknowledges the Special Research Fund (BOF) of Ghent University for its continuous support.

Supporting Information Available

The Supporting Information contains two files:

- A PDF document with (i) additional figures and tables describing the training and validation sets, (ii) the ReaxFF parameters selected for optimization, and (iii) additional performance metrics on the training set that have no counterpart in the validation set.

- A ZIP file with the optimized parameters used for the force field validation, and example input files for the MD simulations in this work.

References

- (1) Brunk, E.; Rothlisberger, U. Mixed Quantum Mechanical/Molecular Mechanical Molecular Dynamics Simulations of Biological Systems in Ground and Electronically Excited States. *Chem. Rev.* **2015**, *115*, 6217–6263.
- (2) Döntgen, M.; Przybylski-Freund, M.-D.; Kröger, L. C.; Kopp, W. A.; Ismail, A. E.; Leonhard, K. Automated Discovery of Reaction Pathways, Rate Constants, and Transition States Using Reactive Molecular Dynamics Simulations. *J. Chem. Theory Comput.* **2015**, *11*, 2517–2524.
- (3) Chenoweth, K.; van Duin, A. C. T.; Dasgupta, S.; III, W. A. G. Initiation Mechanisms and Kinetics of Pyrolysis and Combustion of JP-10 Hydrocarbon Jet Fuel. *J. Phys. Chem. A* **2009**, *113*, 1740–1746.
- (4) Ding, J.; Zhang, L.; Zhang, Y.; Han, K.-L. A Reactive Molecular Dynamics Study of *n*-Heptane Pyrolysis at High Temperature. *J. Phys. Chem. A* **2013**, *117*, 3266–3278.
- (5) Li, X.; Zheng, M.; Ren, C.; Guo, L. ReaxFF Molecular Dynamics Simulations of Thermal Reactivity of Various Fuels in Pyrolysis and Combustion. *Energy & Fuels* **2021**, *35*, 11707–11739.
- (6) Fogarty, J. C.; Aktulga, H. M.; Grama, A. Y.; van Duin, A. C. T.; Pandit, S. A. A reactive molecular dynamics simulation of the silica-water interface. *J. Chem. Phys.* **2010**, *132*, 174704.
- (7) Mueller, J. E.; van Duin, A. C. T.; Goddard, W. A. Application of the ReaxFF

- Reactive Force Field to Reactive Dynamics of Hydrocarbon Chemisorption and Decomposition. *J. Phys. Chem. C* **2010**, *114*, 5675–5685.
- (8) Müller, J.; Hartke, B. reaxFF Reactive Force Field for Disulfide Mechanochemistry, Fitted to Multireference ab Initio Data. *J. Chem. Theory Comput.* **2016**, *12*, 3913–3925.
- (9) Rimsza, J. M.; Jones, R. E.; Criscenti, L. J. Crack propagation in silica from reactive classical molecular dynamics simulations. *J. Am. Ceram. Soc.* **2017**, *101*, 1488–1499.
- (10) Mao, Q.; van Duin, A. C.; Luo, K. Formation of incipient soot particles from polycyclic aromatic hydrocarbons: A ReaxFF molecular dynamics study. *Carbon* **2017**, *121*, 380–388.
- (11) Lei, T.; Guo, W.; Liu, Q.; Jiao, H.; Cao, D.-B.; Teng, B.; Li, Y.-W.; Liu, X.; Wen, X.-D. Mechanism of Graphene Formation via Detonation Synthesis: A DFTB Nanoreactor Approach. *J. Chem. Theory Comput.* **2019**, *15*, 3654–3665.
- (12) van Duin, A. C. T.; Dasgupta, S.; Lorant, F.; Goddard, W. A. ReaxFF: A Reactive Force Field for Hydrocarbons. *J. Phys. Chem. A* **2001**, *105*, 9396–9409.
- (13) van Duin, A. C. T.; Strachan, A.; Stewman, S.; Zhang, Q.; Xu, X.; Goddard, W. A. ReaxFF_{SiO} Reactive Force Field for Silicon and Silicon Oxide Systems. *J. Phys. Chem. A* **2003**, *107*, 3803–3811.
- (14) Senftle, T. P.; Hong, S.; Islam, M. M.; Kylasa, S. B.; Zheng, Y.; Shin, Y. K.; Junkermeier, C.; Engel-Herbert, R.; Janik, M. J.; Aktulga, H. M. et al. The ReaxFF reactive force-field: development, applications and future directions. *npj Comput. Mater.* **2016**, *2*, 15011.
- (15) Tersoff, J. Empirical Interatomic Potential for Carbon, with Applications to Amorphous Carbon. *Phys. Rev. Lett.* **1988**, *61*, 2879–2882.

- (16) O'Connor, T. C.; Andzelm, J.; Robbins, M. O. AIREBO-M: A reactive model for hydrocarbons at extreme pressures. *J. Chem. Phys.* **2015**, *142*, 024903.
- (17) Zhang, D.; Fonseca, A. F.; Liang, T.; Phillpot, S. R.; Sinnott, S. B. Dynamics of graphene/Al interfaces using COMB3 potentials. *Phys. Rev. Mater.* **2019**, *3*, 114002.
- (18) Rowe, P.; Deringer, V. L.; Gasparotto, P.; Csányi, G.; Michaelides, A. An accurate and transferable machine learning potential for carbon. *J. Chem. Phys.* **2020**, *153*, 034702.
- (19) Xue, L.-Y.; Guo, F.; Wen, Y.-S.; Feng, S.-Q.; Huang, X.-N.; Guo, L.; Li, H.-S.; Cui, S.-X.; Zhang, G.-Q.; Wang, Q.-L. ReaxFF-MPNN machine learning potential: a combination of reactive force field and message passing neural networks. *Phys. Chem. Chem. Phys.* **2021**, *23*, 19457–19464.
- (20) Schreiner, M.; Bhowmik, A.; Vegge, T.; Busk, J.; Winther, O. Transition1x - a dataset for building generalizable reactive machine learning potentials. *Sci. Data* **2022**, *9*, 779.
- (21) Pahari, P.; Chaturvedi, S. Determination of best-fit potential parameters for a reactive force field using a genetic algorithm. *J. Mol. Model.* **2011**, *18*, 1049–1061.
- (22) Deetz, J. D.; Faller, R. Parallel Optimization of a Reactive Force Field for Polycondensation of Alkoxysilanes. *J. Phys. Chem. B* **2014**, *118*, 10966–10978.
- (23) Jaramillo-Botero, A.; Naserifar, S.; Goddard, W. A. General Multiobjective Force Field Optimization Framework, with Application to Reactive Force Fields for Silicon Carbide. *J. Chem. Theory Comput.* **2014**, *10*, 1426–1439.
- (24) Dittner, M.; Müller, J.; Aktulga, H. M.; Hartke, B. Efficient global optimization of reactive force-field parameters. *J. Comput. Chem.* **2015**, *36*, 1550–1561.
- (25) Trnka, T.; Tvaroška, I.; Koča, J. Automated Training of ReaxFF Reactive Force Fields for Energetics of Enzymatic Reactions. *J. Chem. Theory Comput.* **2017**, *14*, 291–302.

- (26) Furman, D.; Carmeli, B.; Zeiri, Y.; Kosloff, R. Enhanced Particle Swarm Optimization Algorithm: Efficient Training of ReaxFF Reactive Force Fields. *J. Chem. Theory Comput.* **2018**, *14*, 3100–3112.
- (27) Shchygol, G.; Yakovlev, A.; Trnka, T.; van Duin, A. C. T.; Verstraelen, T. ReaxFF Parameter Optimization with Monte-Carlo and Evolutionary Algorithms: Guidelines and Insights. *J. Chem. Theory Comput.* **2019**, *15*, 6799–6812.
- (28) Sengul, M. Y.; Song, Y.; Nayir, N.; Gao, Y.; Hung, Y.; Dasgupta, T.; van Duin, A. C. T. INDEEDopt: a deep learning-based ReaxFF parameterization framework. *npj Comput. Mater.* **2021**, *7*, 68.
- (29) Kaymak, M. C.; Rahnamoun, A.; O’Hearn, K. A.; van Duin, A. C. T.; Merz Jr., K. M.; Aktulga, H. M. JAX-ReaxFF: A Gradient-Based Framework for Fast Optimization of Reactive Force Fields. *J. Chem. Theory Comput.* **2022**, *18*, 5181–5194.
- (30) Komissarov, L.; Krep, L.; Schmalz, F.; Kopp, W. A.; Leonhard, K.; Verstraelen, T. A Reactive Molecular Dynamics Study of Chlorinated Organic Compounds. Part I: Force Field Development. *ChemPhysChem* **2023**, *24*, e202200786.
- (31) Gustavo, M. F.; Hellström, M.; Verstraelen, T. Sensitivity Analysis for ReaxFF Reparametrization Using the Hilbert–Schmidt Independence Criterion. *J. Chem. Theory Comput.* **2023**, *19*, 2557–2573.
- (32) Wang, H.; Zhang, L.; Han, J.; E, W. DeePMD-kit: A deep learning package for many-body potential energy representation and molecular dynamics. *Comput. Phys. Commun.* **2018**, *228*, 178–184.
- (33) Unke, O. T.; Meuwly, M. PhysNet: A Neural Network for Predicting Energies, Forces, Dipole Moments, and Partial Charges. *J. Chem. Theory Comput.* **2019**, *15*, 3678–3693.

- (34) Cools-Ceuppens, M.; Dambre, J.; Verstraelen, T. Modeling Electronic Response Properties with an Explicit-Electron Machine Learning Potential. *J. Chem. Theory Comput.* **2022**, *18*, 1672–1691.
- (35) Fedkin, M. V.; Shin, Y. K.; Dasgupta, N.; Yeon, J.; Zhang, W.; van Duin, D.; van Duin, A. C. T.; Mori, K.; Fujiwara, A.; Machida, M. et al. Development of the ReaxFF Methodology for Electrolyte–Water Systems. *J. Phys. Chem. A* **2019**, *123*, 2125–2141.
- (36) Brown, I.; Smith, R.; Kenny, S. D. A ReaxFF potential for Al–ZnO systems. *Model. Simul. Mater. Sci. Eng.* **2022**, *30*, 035001.
- (37) Verstraelen, T.; Sukhomlinov, S. V.; Van Speybroeck, V.; Waroquier, M.; Smirnov, K. S. Computation of Charge Distribution and Electrostatic Potential in Silicates with the Use of Chemical Potential Equalization Models. *J. Phys. Chem. C* **2012**, *116*, 490–504.
- (38) Bureekaew, S.; Amirjalayer, S.; Tafipolsky, M.; Spickermann, C.; Roy, T. K.; Schmid, R. MOF-FF – A flexible first-principles derived force field for metal-organic frameworks. *Phys. Status Solidi B* **2013**, *250*, 1128–1141.
- (39) Grimme, S.; Bannwarth, C.; Shushkov, P. A Robust and Accurate Tight-Binding Quantum Chemical Method for Structures, Vibrational Frequencies, and Noncovalent Interactions of Large Molecular Systems Parametrized for All spd-Block Elements ($Z = 1–86$). *J. Chem. Theory Comput.* **2017**, *13*, 1989–2009.
- (40) Komissarov, L.; Verstraelen, T. Improving the Silicon Interactions of GFN-xTB. *J. Chem. Inf. Model.* **2021**, *61*, 5931–5937.
- (41) Li, J.; Song, X.; Li, P.; Herzfeld, J. A Carbon Is a Carbon Is a Carbon: Orbital-Free Simulations of Hydrocarbon Chemistry without Resort to Atom Types. *J. Phys. Chem. A* **2022**, *126*, 8468–8475.

- (42) Włodarczyk, A.; Uchroński, M.; Podsiadły-Paszkowska, A.; Irek, J.; Szyja, B. M. Mixing ReaxFF parameters for transition metal oxides using force-matching method. *J. Mol. Model.* **2022**, *28*, 8.
- (43) Komissarov, L.; Rüger, R.; Hellström, M.; Verstraelen, T. ParAMS: Parameter Optimization for Atomistic and Molecular Simulations. *J. Chem. Inf. Model.* **2021**, *61*, 3737–3743.
- (44) Gustavo, M. F.; Verstraelen, T. GloMPO (Globally Managed Parallel Optimization): a tool for expensive, black-box optimizations, application to ReaxFF reparameterizations. *J. Cheminformatics* **2022**, *14*, 7.
- (45) Smith, J. S.; Isayev, O.; Roitberg, A. E. ANI-1: an extensible neural network potential with DFT accuracy at force field computational cost. *Chem. Sci.* **2017**, *8*, 3192–3203.
- (46) Chen, C.; Ong, S. P. A universal graph deep learning interatomic potential for the periodic table. *Nat. Comput. Sci.* **2022**, *2*, 718–728.
- (47) Takamoto, S.; Shinagawa, C.; Motoki, D.; Nakago, K.; Li, W.; Kurata, I.; Watanabe, T.; Yayama, Y.; Iriguchi, H.; Asano, Y. et al. Towards universal neural network potential for material discovery applicable to arbitrary combination of 45 elements. *Nat. Commun.* **2022**, *13*, 2991.
- (48) Hart, L. D.; Lense, E. *Alumina Chemicals: Science and Technology Handbook*; John Wiley & Sons, 1990.
- (49) Lefèvre, G.; Duc, M.; Lepeut, P.; Caplain, R.; Fédoroff, M. Hydration of γ -Alumina in Water and Its Effects on Surface Reactivity. *Langmuir* **2002**, *18*, 7530–7537.
- (50) Arrouvel, C.; Digne, M.; Breysse, M.; Toulhoat, H.; Raybaud, P. Effects of morphology on surface hydroxyl concentration: a DFT comparison of anatase–TiO₂ and γ -alumina catalytic supports. *J. Catal.* **2004**, *222*, 152–166.

- (51) Lagauche, M.; Larmier, K.; Jolimaitre, E.; Barthelet, K.; Chizallet, C.; Favergeon, L.; Pijolat, M. Thermodynamic Characterization of the Hydroxyl Group on the γ -Alumina Surface by the Energy Distribution Function. *J. Phys. Chem. C* **2017**, *121*, 16770–16782.
- (52) Pigeon, T.; Chizallet, C.; Raybaud, P. Revisiting γ -alumina surface models through the topotactic transformation of boehmite surfaces. *J. Catal.* **2022**, *405*, 140–151.
- (53) Levin, I.; Brandon, D. Metastable Alumina Polymorphs: Crystal Structures and Transition Sequences. *J. Am. Ceram. Soc.* **1998**, *81*, 1995–2012.
- (54) Trueba, M.; Trasatti, S. P. γ -Alumina as a Support for Catalysts: A Review of Fundamental Aspects. *Eur. J. Inorg. Chem.* **2005**, *2005*, 3393–3403.
- (55) Euzen, P.; Raybaud, P.; Krokidis, X.; Toulhoat, H.; Le Loarer, J.-L.; Jolivet, J.-P.; Froidefond, C. In *Handbook of Porous Solids*; Schüth, F., Sing, K. S. W., Weitkamp, J., Eds.; John Wiley & Sons, Ltd, 2002; pp 1591–1677.
- (56) Knözinger, H. Dehydration of Alcohols on Aluminum Oxide. *Angew. Chem. Int. Ed. Engl.* **1968**, *7*, 791–805.
- (57) Knözinger, H.; Bühl, H.; Kochloeff, K. The dehydration of alcohols on alumina: XIV. Reactivity and mechanism. *J. Catal.* **1972**, *24*, 57–68.
- (58) Phung, T. K.; Lagazzo, A.; Rivero Crespo, M. Á.; Sánchez Escribano, V.; Busca, G. A study of commercial transition aluminas and of their catalytic activity in the dehydration of ethanol. *J. Catal.* **2014**, *311*, 102–113.
- (59) Kohl, A. L.; Nielsen, R. B. In *Gas Purification (Fifth Edition)*; Kohl, A. L., Nielsen, R. B., Eds.; Gulf Professional Publishing: Houston, 1997; pp 670–730.
- (60) Larmier, K.; Chizallet, C.; Cadran, N.; Maury, S.; Abboud, J.; Lamic-Humblot, A.-F.; Marceau, E.; Lauron-Pernot, H. Mechanistic Investigation of Isopropanol Conversion

- on Alumina Catalysts: Location of Active Sites for Alkene/Ether Production. *ACS Catal.* **2015**, *5*, 4423–4437.
- (61) Jain, J. R.; Pillai, C. N. Catalytic dehydration of alcohols over alumina: Mechanism of ether formation. *J. Catal.* **1967**, *9*, 322–330.
- (62) Raybaud, P.; Toulhoat, H. *Catalysis by Transition Metal Sulphides: From Molecular Theory to Industrial Application*; Editions TECHNIP, 2013.
- (63) Copéret, C.; Comas-Vives, A.; Conley, M. P.; Estes, D. P.; Fedorov, A.; Mougel, V.; Nagae, H.; Núñez-Zarur, F.; Zhizhko, P. A. Surface Organometallic and Coordination Chemistry toward Single-Site Heterogeneous Catalysts: Strategies, Methods, Structures, and Activities. *Chem. Rev.* **2016**, *116*, 323–421.
- (64) Boudart, M. In *Advances in Catalysis*; Eley, D. D., Pines, H., Weisz, P. B., Eds.; Academic Press, 1969; pp 153–166.
- (65) Prins, R. On the structure of γ -Al₂O₃. *J. Catal.* **2020**, *392*, 336–346.
- (66) Valero, M. C.; Raybaud, P. Computational chemistry approaches for the preparation of supported catalysts: Progress and challenges. *J. Catal.* **2020**, *391*, 539–547.
- (67) Krokidis, X.; Raybaud, P.; Gobichon, A.-E.; Rebours, B.; Euzen, P.; Toulhoat, H. Theoretical Study of the Dehydration Process of Boehmite to γ -Alumina. *J. Phys. Chem. B* **2001**, *105*, 5121–5130.
- (68) Wischert, R.; Laurent, P.; Copéret, C.; Delbecq, F.; Sautet, P. γ -Alumina: the essential and unexpected role of water for the structure, stability, and reactivity of "defect" sites. *J. Am. Chem. Soc.* **2012**, *134*, 14430–14449.
- (69) Digne, M.; Sautet, P.; Raybaud, P.; Euzen, P.; Toulhoat, H. Hydroxyl Groups on γ -Alumina Surfaces: A DFT Study. *J. Catal.* **2002**, *211*, 1–5.

- (70) Digne, M.; Sautet, P.; Raybaud, P.; Euzen, P.; Toulhoat, H. Use of DFT to achieve a rational understanding of acid–basic properties of γ -alumina surfaces. *J. Catal.* **2004**, *226*, 54–68.
- (71) Paglia, G.; Buckley, C. E.; Rohl, A. L.; Hart, R. D.; Winter, K.; Studer, A. J.; Hunter, B. A.; Hanna, J. V. Boehmite Derived γ -Alumina System. 1. Structural Evolution with Temperature, with the Identification and Structural Determination of a New Transition Phase, γ' -Alumina. *Chem. Mater.* **2004**, *16*, 220–236.
- (72) Réocreux, R.; Girel, É.; Clabaut, P.; Tuel, A.; Besson, M.; Chaumonnot, A.; Cabiac, A.; Sautet, P.; Michel, C. Reactivity of shape-controlled crystals and metadynamics simulations locate the weak spots of alumina in water. *Nat. Commun.* **2019**, *10*, 3139.
- (73) Mardilovich, P. P.; Govyadinov, A. N.; Mukhurov, N. I.; Rzhetskii, A. M.; Paterson, R. New and modified anodic alumina membranes Part I. Thermotreatment of anodic alumina membranes. *J. Membr. Sci.* **1995**, *98*, 131–142.
- (74) Brown, G. E.; Henrich, V. E.; Casey, W. H.; Clark, D. L.; Eggleston, C.; Felmy, A.; Goodman, D. W.; Grätzel, M.; Maciel, G.; McCarthy, M. I. et al. Metal Oxide Surfaces and Their Interactions with Aqueous Solutions and Microbial Organisms. *Chem. Rev.* **1999**, *99*, 77–174.
- (75) Batista, A. T. F.; Wisser, D.; Pigeon, T.; Gajan, D.; Diehl, F.; Rivallan, M.; Catita, L.; Gay, A.-S.; Lesage, A.; Chizallet, C. et al. Beyond γ -Al₂O₃ crystallite surfaces: The hidden features of edges revealed by solid-state ¹H NMR and DFT calculations. *J. Catal.* **2019**, *378*, 140–143.
- (76) Batista, A.; Pigeon, T.; Meyet, J.; Wisser, D.; Rivallan, M.; Gajan, D.; Catita, L.; Diehl, F.; Gay, A.; Chizallet, C. et al. Structure, Location and Spatial Proximities of

Hydroxyls on γ -Alumina Crystallites by High-Resolution Solid-State NMR and DFT Modelling: Why Edges hold the Key. *ACS Catal.* **2023**, *13*, 6536–6548.

- (77) Pitman, M. C.; van Duin, A. C. T. Dynamics of Confined Reactive Water in Smectite Clay–Zeolite Composites. *J. Am. Chem. Soc.* **2012**, *134*, 3042–3053.
- (78) Rimsza, J. M.; Yeon, J.; van Duin, A. C. T.; Du, J. Water Interactions with Nanoporous Silica: Comparison of ReaxFF and ab Initio based Molecular Dynamics Simulations. *J. Phys. Chem. C* **2016**, *120*, 24803–24816.
- (79) Porter, A. J.; O’Malley, A. J. A Classical Molecular Dynamics Study on the Effect of Si/Al Ratio and Silanol Nest Defects on Water Diffusion in Zeolite HY. *J. Phys. Chem. C* **2021**, *125*, 11567–11579.
- (80) van Gunsteren, W. F.; Berendsen, H. J. C. Computer Simulation of Molecular Dynamics: Methodology, Applications, and Perspectives in Chemistry. *Angew. Chem. Int. Ed. Engl.* **1990**, *29*, 992–1023.
- (81) Nakata, A.; Baker, J. S.; Mujahed, S. Y.; Poulton, J. T. L.; Arapan, S.; Lin, J.; Raza, Z.; Yadav, S.; Truflandier, L.; Miyazaki, T. et al. Large scale and linear scaling DFT with the CONQUEST code. *J. Chem. Phys.* **2020**, *152*, 164112.
- (82) Kühne, T. D.; Iannuzzi, M.; Ben, M. D.; Rybkin, V. V.; Seewald, P.; Stein, F.; Laino, T.; Khaliullin, R. Z.; Schütt, O.; Schiffmann, F. et al. CP2K: An electronic structure and molecular dynamics software package - Quickstep: Efficient and accurate electronic structure calculations. *J. Chem. Phys.* **2020**, *152*, 194103.
- (83) Raybaud, P.; Digne, M.; Iftimie, R.; Wellens, W.; Euzen, P.; Toulhoat, H. Morphology and Surface Properties of Boehmite (γ -AlOOH): A Density Functional Theory Study. *J. Catal.* **2001**, *201*, 236–246.

- (84) Motta, A.; Gaigeot, M.-P.; Costa, D. AIMD Evidence of Inner Sphere Adsorption of Glycine on a Stepped (101) Boehmite AlOOH Surface. *J. Phys. Chem. C* **2012**, *116*, 23418–23427.
- (85) Ngouana-Wakou, B. F.; Cornette, P.; Corral Valero, M.; Costa, D.; Raybaud, P. An Atomistic Description of the γ -Alumina/Water Interface Revealed by Ab Initio Molecular Dynamics. *J. Phys. Chem. C* **2017**, *121*, 10351–10363.
- (86) Zhang, Q.; Çağ m, T.; van Duin, A.; Goddard, W. A.; Qi, Y.; Hector, L. G. Adhesion and nonwetting-wetting transition in the Al/ α – Al₂O₃ interface. *Phys. Rev. B* **2004**, *69*, 045423.
- (87) Russo, M. F.; Li, R.; Mench, M.; van Duin, A. C. Molecular dynamic simulation of aluminum–water reactions using the ReaxFF reactive force field. *Int. J. Hydrog. Energy* **2011**, *36*, 5828–5835.
- (88) Joshi, K. L.; van Duin, A. C. T. Molecular Dynamics Study on the Influence of Additives on the High-Temperature Structural and Acidic Properties of ZSM-5 Zeolite. *Energy & Fuels* **2013**, *27*, 4481–4488.
- (89) Sen, F. G.; Alpas, A. T.; van Duin, A. C. T.; Qi, Y. Oxidation-assisted ductility of aluminium nanowires. *Nat. Commun.* **2014**, *5*, 3959.
- (90) Joshi, K. L.; Psfogiannakis, G.; Duin, A. C. T. v.; Raman, S. Reactive molecular simulations of protonation of water clusters and depletion of acidity in H-ZSM-5 zeolite. *Phys. Chem. Chem. Phys.* **2014**, *16*, 18433–18441.
- (91) Hong, S.; van Duin, A. C. Molecular Dynamics Simulations of the Oxidation of Aluminum Nanoparticles using the ReaxFF Reactive Force Field. *J. Phys. Chem. C* **2015**, *119*, 17876–17886.

- (92) Gunkelmann, N.; Bringa, E. M.; Rosandi, Y. Molecular Dynamics Simulations of Aluminum Foams under Tension: Influence of Oxidation. *J. Phys. Chem. C* **2018**, *122*, 26243–26250.
- (93) Ramírez, M.; González, R. I.; Baltazar, S. E.; Rojas-Nunez, J.; Allende, S.; Valdivia, J. A.; Rogan, J.; Kiwi, M.; Valencia, F. J. Thermal stability of aluminum oxide nanoparticles: role of oxygen concentration. *Inorg. Chem. Front.* **2019**, *6*, 1701–1706.
- (94) Rosandi, Y.; Luu, H.-T.; Urbassek, H. M.; Gunkelmann, N. Molecular dynamics simulations of the mechanical behavior of alumina coated aluminum nanowires under tension and compression. *RSC Adv.* **2020**, *10*, 14353–14359.
- (95) Chiche, D.; Chizallet, C.; Durupthy, O.; Chanéac, C.; Revel, R.; Raybaud, P.; Jolivert, J.-P. Growth of boehmite particles in the presence of xylitol: morphology oriented by the nest effect of hydrogen bonding. *Phys. Chem. Chem. Phys.* **2009**, *11*, 11310–11323.
- (96) Mortier, W. J.; Ghosh, S. K.; Shankar, S. Electronegativity-equalization method for the calculation of atomic charges in molecules. *J. Am. Chem. Soc.* **1986**, *108*, 4315–4320.
- (97) Verstraelen, T.; Ayers, P. W.; Van Speybroeck, V.; Waroquier, M. ACKS2: atom-condensed Kohn-Sham DFT approximated to second order. *J. Chem. Phys.* **2013**, *138*, 074108.
- (98) ReaxFF force field format specification. https://www.scm.com/doc/ReaxFF/ffield_descrp.html, Accessed on June 21, 2023.
- (99) Chenoweth, K.; van Duin, A. C. T.; Goddard, W. A. ReaxFF Reactive Force Field for Molecular Dynamics Simulations of Hydrocarbon Oxidation. *J. Phys. Chem. A* **2008**, *112*, 1040–1053.

- (100) The Amsterdam Modeling Suite. <https://www.scm.com/amsterdam-modeling-suite>, Accessed on June 21, 2023.
- (101) Plimpton, S. Fast Parallel Algorithms for Short-Range Molecular Dynamics. *J. Comput. Phys.* **1995**, *117*, 1–19.
- (102) Thompson, A. P.; Aktulga, H. M.; Berger, R.; Bolintineanu, D. S.; Brown, W. M.; Crozier, P. S.; in 't Veld, P. J.; Kohlmeyer, A.; Moore, S. G.; Nguyen, T. D. et al. LAMMPS - a flexible simulation tool for particle-based materials modeling at the atomic, meso, and continuum scales. *Comput. Phys. Commun.* **2022**, *271*, 108171.
- (103) ParAMS 2023.101 documentation. <https://www.scm.com/doc/params>, Accessed on June 21, 2023.
- (104) Gaus, M.; Cui, Q.; Elstner, M. DFTB3: Extension of the Self-Consistent-Charge Density-Functional Tight-Binding Method (SCC-DFTB). *J. Chem. Theory Comput.* **2011**, *7*, 931–948.
- (105) Larsen, A. H.; Mortensen, J. J.; Blomqvist, J.; Castelli, I. E.; Christensen, R.; Dułak, M.; Friis, J.; Groves, M. N.; Hammer, B.; Hargus, C. et al. The atomic simulation environment—a Python library for working with atoms. *J. Phys.: Condens. Matter* **2017**, *29*, 273002.
- (106) Humphrey, W.; Dalke, A.; Schulten, K. VMD: Visual molecular dynamics. *J. Mol. Graph.* **1996**, *14*, 33–38.
- (107) Kennes, K.; Kubarev, A.; Demaret, C.; Trops, L.; Delpoux, O.; Rivallan, M.; Guillon, E.; Méthivier, A.; de Bruin, T.; Gomez, A. et al. Multiscale Visualization and Quantification of the Effect of Binders on the Acidity of Shaped Zeolites. *ACS Catal.* **2022**, *12*, 6794–6808.

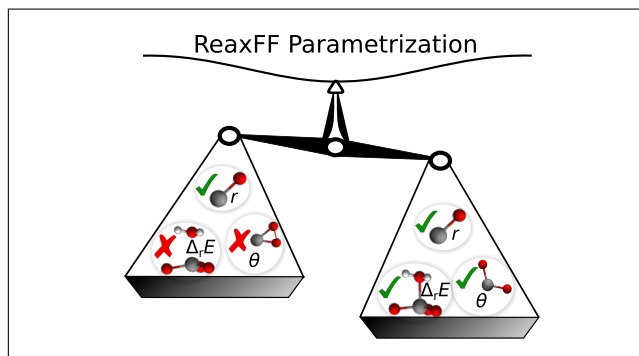
- (108) Perdew, J. P.; Ernzerhof, M.; Burke, K. Rationale for mixing exact exchange with density functional approximations. *J. Chem. Phys.* **1996**, *105*, 9982–9985.
- (109) Hafner, J. Ab-initio simulations of materials using VASP: Density-functional theory and beyond. *J. Comput. Chem.* **2008**, *29*, 2044–2078.
- (110) Blöchl, P. E. Projector augmented-wave method. *Phys. Rev. B* **1994**, *50*, 17953–17979.
- (111) Steinmann, S. N.; Corminboeuf, C. Comprehensive Benchmarking of a Density-Dependent Dispersion Correction. *J. Chem. Theory Comput.* **2011**, *7*, 3567–3577.
- (112) LaBrosse, M. R.; Johnson, J. K.; van Duin, A. C. T. Development of a Transferable Reactive Force Field for Cobalt. *J. Phys. Chem. A* **2010**, *114*, 5855–5861.
- (113) Iype, E.; Hutter, M.; Jansen, A. P. J.; Nedeá, S. V.; Rindt, C. C. M. Parameterization of a reactive force field using a Monte Carlo algorithm. *J. Comput. Chem.* **2013**, *34*, 1143–1154.
- (114) Boes, J. R.; Groenenboom, M. C.; Keith, J. A.; Kitchin, J. R. Neural network and ReaxFF comparison for Au properties. *Int. J. Quantum Chem.* **2016**, *116*, 979–987.
- (115) Kokotailo, G. T.; Lawton, S. L.; Olson, D. H.; Meier, W. M. Structure of synthetic zeolite ZSM-5. *Nature* **1978**, *272*, 437–438.
- (116) van Duin, A. C. T.; Baas, J. M. A.; van de Graaf, B. Delft molecular mechanics: a new approach to hydrocarbon force fields. Inclusion of a geometry-dependent charge calculation. *J. Chem. Soc. Faraday Trans.* **1994**, *90*, 2881.
- (117) Hansen, N. In *Towards a new evolutionary computation. Advances on estimation of distribution algorithms*; Lozano, J. A., Larrañaga, P., Inza, I., Bengoetxea, E., Eds.; Springer: Berlin, Heidelberg, 2006; pp 75–102.

- (118) Hansen, N.; Müller, S. D.; Koumoutsakos, P. Reducing the Time Complexity of the Derandomized Evolution Strategy with Covariance Matrix Adaptation (CMA-ES). *Evol. Comput.* **2003**, *11*, 1–18.
- (119) Hansen, N. The CMA Evolution Strategy: A Tutorial. 2023; arXiv:1604.00772.
- (120) Raybaud, P.; Chizallet, C.; Pigeon, T. NOMAD dataset: Gamma-Alumina surfaces. 2021; <https://doi.org/10.17172/NOMAD/2021.11.10-1>, Accessed on November 16, 2022.
- (121) Giagkiozis, I.; Fleming, P. Methods for multi-objective optimization: An analysis. *Inf. Sci.* **2015**, *293*, 338–350.
- (122) Tian, Y.; Si, L.; Zhang, X.; Cheng, R.; He, C.; Tan, K. C.; Jin, Y. Evolutionary Large-Scale Multi-Objective Optimization: A Survey. *ACM Comput. Surv.* **2021**, *54*, 1–34.
- (123) Blanchard, P.; Higham, D. J.; Higham, N. J. Accurately computing the log-sum-exp and softmax functions. *IMA J. Numer. Anal.* **2021**, *41*, 2311–2330.
- (124) Palaz, D.; Synnaeve, G.; Collobert, R. Jointly Learning to Locate and Classify Words Using Convolutional Networks. Proc. Interspeech 2016. 2016; pp 2741–2745.
- (125) Nian, R.; Liu, J.; Huang, B. A review On reinforcement learning: Introduction and applications in industrial process control. *Comput. Chem. Eng.* **2020**, *139*, 106886.
- (126) Sutton, R. S.; Barto, A. G. *Reinforcement Learning: an introduction*; MIT Press, 2018; Chapter Gradient Bandit Algorithms, pp 37–40.
- (127) Brown, K. S.; Sethna, J. P. Statistical mechanical approaches to models with many poorly known parameters. *Phys. Rev. E* **2003**, *68*, 021904.

- (128) Waterfall, J. J.; Casey, F. P.; Gutenkunst, R. N.; Brown, K. S.; Myers, C. R.; Brouwer, P. W.; Elser, V.; Sethna, J. P. Sloppy-Model Universality Class and the Vandermonde Matrix. *Phys. Rev. Lett.* **2006**, *97*, 150601.
- (129) Gutenkunst, R. N.; Waterfall, J. J.; Casey, F. P.; Brown, K. S.; Myers, C. R.; Sethna, J. P. Universally Sloppy Parameter Sensitivities in Systems Biology Models. *PLoS Comput. Biol.* **2007**, *3*, e189.
- (130) Transtrum, M. K.; Machta, B. B.; Brown, K. S.; Daniels, B. C.; Myers, C. R.; Sethna, J. P. Perspective: Slowness and emergent theories in physics, biology, and beyond. *J. Chem. Phys.* **2015**, *143*, 010901.
- (131) Verstraelen, T.; Bultinck, P.; Van Speybroeck, V.; Ayers, P. W.; Van Neck, D.; Waroquier, M. The Significance of Parameters in Charge Equilibration Models. *J. Chem. Theory Comput.* **2011**, *7*, 1750–1764.
- (132) Rahaman, O.; van Duin, A. C. T.; Bryantsev, V. S.; Mueller, J. E.; Solares, S. D.; Goddard, W. A. I.; Doren, D. J. Development of a ReaxFF Reactive Force Field for Aqueous Chloride and Copper Chloride. *J. Phys. Chem. A* **2010**, *114*, 3556–3568.
- (133) Goken, E. G.; Joshi, K. L.; Russo, M. F.; van Duin, A. C. T.; Castleman, A. W. Effect of Formic Acid Addition on Water Cluster Stability and Structure. *J. Phys. Chem. A* **2011**, *115*, 4657–4664.
- (134) Hu, X.; Schuster, J.; Schulz, S. E. Multiparameter and Parallel Optimization of ReaxFF Reactive Force Field for Modeling the Atomic Layer Deposition of Copper. *J. Phys. Chem. C* **2017**, *121*, 28077–28089.
- (135) Bertels, L. W.; Newcomb, L. B.; Alaghemandi, M.; Green, J. R.; Head-Gordon, M. Benchmarking the Performance of the ReaxFF Reactive Force Field on Hydrogen Combustion Systems. *J. Phys. Chem. A* **2020**, *124*, 5631–5645.

- (136) Daksha, C. M.; Yeon, J.; Chowdhury, S. C.; Gillespie Jr., J. W. Automated ReaxFF parametrization using machine learning. *Comput. Mater. Sci.* **2021**, *187*, 110107.
- (137) Yeon, J.; Chowdhury, S. C.; Daksha, C. M.; Gillespie, J. W. Development of Mg/Al/Si/O ReaxFF Parameters for Magnesium Aluminosilicate Glass Using an Artificial Neural Network-Assisted Genetic Algorithm. *J. Phys. Chem. C* **2021**, *125*, 18380–18394.
- (138) Evans, D. J.; Holian, B. L. The Nose–Hoover thermostat. *J. Chem. Phys.* **1985**, *83*, 4069–4074.

TOC Graphic



Supporting Information for

Managing Expectations and Imbalanced Training Data in Reactive Force Field Development: an Application to Water Adsorption on Alumina

Loïc Dumortier,^{†,‡} Céline Chizallet,[¶] Benoit Creton,[†] Theodorus de Bruin,[†] and
Toon Verstraelen^{*,‡}

[†]*IFP Energies nouvelles, 1 et 4 Avenue de Bois-Préau, 92852 Rueil-Malmaison, France*

[‡]*Center for Molecular Modeling (CMM), Ghent University, Technologiepark-Zwijnaarde 46,
B-9052, Zwijnaarde, Belgium*

[¶]*IFP Energies nouvelles, Rond-point de l'échangeur de Solaize, BP3, 69360 Solaize, France*

E-mail: toon.verstraelen@ugent.be

Contents

S1 Additional Display Items	3
S2 Comparison of Non-Equilibrium ReaxFF and DFT energies	29
References	32

S1 Additional Display Items

Table S1: Structures in the training set and contributions to each category of data. Bonds are represented by pairs of chemical elements, angles by triplets. The symbol \cdots denotes a hydrogen bond. Internal coordinates with oxygen not bound to aluminum are discarded. For hydrated alumina surfaces and edges, and for boehmite surfaces, the internal coordinates without hydrogen are not considered.

Structure	Chem. Form.	O-H	O \cdots H	Al-O	Al-Al	O-Al-O	Al-O-Al	Al-O-H	Al-O \cdots H	H-O \cdots H	H \cdots O \cdots H
alpha_bulk	Al ₁₂ O ₁₈			72	84	180	108				
boehm_bulk	Al ₃₂ O ₆₄ H ₃₂	32	32	192	128	480	224	64	64	32	
boehm_surf-001_00w	Al ₄₈ O ₉₆ H ₄₈	48	32	272	160	640	288	96	64	32	
boehm_surf-001_08w	Al ₄₈ O ₁₁₂ H ₈₀	80	40		160			160	80	40	
boehm_surf-010_00w	Al ₇₂ O ₁₄₄ H ₇₂	72	48	432	288	1080	504	144	96	48	
boehm_surf-100_00w	Al ₄₈ O ₉₆ H ₄₈	48	48	256	160	576	272	80	80	48	
boehm_surf-100_12w	Al ₄₈ O ₁₂₀ H ₉₆	96	80		160			128	112	96	24
boehm_surf-100_16w	Al ₄₈ O ₁₂₈ H ₁₁₂	112	89		160			144	137	98	24
boehm_surf-101_00w	Al ₄₈ O ₉₆ H ₄₈	49	33	254	168	560	250	100	68	18	6
boehm_surf-101_12w	Al ₄₈ O ₁₂₀ H ₉₆	96	66		156			156	102	72	18
gamma_bulk	Al ₁₆ O ₂₄			88	88	204	120				
gamma_edge-100-110_00w	Al ₉₆ O ₁₄₄			481	424	1003	598				
gamma_edge-100-110_01w	Al ₉₆ O ₁₄₅ H ₂	2			425			3			
gamma_edge-100-110_02w	Al ₉₆ O ₁₄₆ H ₄	4	1		426			6	2		
gamma_edge-100-110_03w	Al ₉₆ O ₁₄₇ H ₆	6	2		422			10	4		
gamma_edge-100-110_04w	Al ₉₆ O ₁₄₈ H ₈	8	3		426			13	6		1
gamma_edge-100-110_05w	Al ₉₆ O ₁₄₉ H ₁₀	10	4		424			17	8		2
gamma_edge-100-110_07w	Al ₉₆ O ₁₅₁ H ₁₄	14	7		424			23	13	2	2
gamma_surf-100_00w	Al ₆₄ O ₉₆			320	280	656	384				
gamma_surf-100_01w	Al ₆₄ O ₁₀₀ H ₈	8	4		284			16	4	4	
gamma_surf-100_02w	Al ₆₄ O ₁₀₄ H ₁₆	16	8		282			24	8	8	4
gamma_surf-100_03w	Al ₆₄ O ₁₀₈ H ₂₄	24	16		280			40	16	16	8
gamma_surf-100_04w	Al ₆₄ O ₁₁₂ H ₃₂	32	20		280			52	28	20	8
gamma_surf-110_00w	Al ₆₄ O ₉₆			304	240	600	368				
gamma_surf-110_01w	Al ₆₄ O ₁₀₀ H ₈	8	4		232			16	8		
gamma_surf-110_02w	Al ₆₄ O ₁₀₄ H ₁₆	16	8		240			24	16		
gamma_surf-110_03w	Al ₆₄ O ₁₀₈ H ₂₄	24	12		240			44	16	8	4
gamma_surf-110_04w	Al ₆₄ O ₁₁₂ H ₃₂	32	24		240			52	44	12	8
gamma_surf-110_05w	Al ₆₄ O ₁₁₆ H ₄₀	40	28		240			60	52	12	12
gamma_surf-110_06w	Al ₆₄ O ₁₂₀ H ₄₈	48	32		236			88	32	32	12
gamma_surf-111_00w	Al ₄₀ O ₆₀			212	190	480	286				
gamma_surf-111_04w	Al ₃₂ O ₅₆ H ₁₆	16	8		144			30	14	6	
gamma_surf-111_05w	Al ₃₂ O ₅₈ H ₂₀	20	10		146			36	14	10	2
gamma_surf-111_06w	Al ₃₂ O ₆₀ H ₂₄	24	12		146			44	16	12	2
monomer	AlO ₄ H ₅	5		4		6		5			
water	O H ₂										
total		990	671	2887	8383	6465	3402	1675	1104	626	137

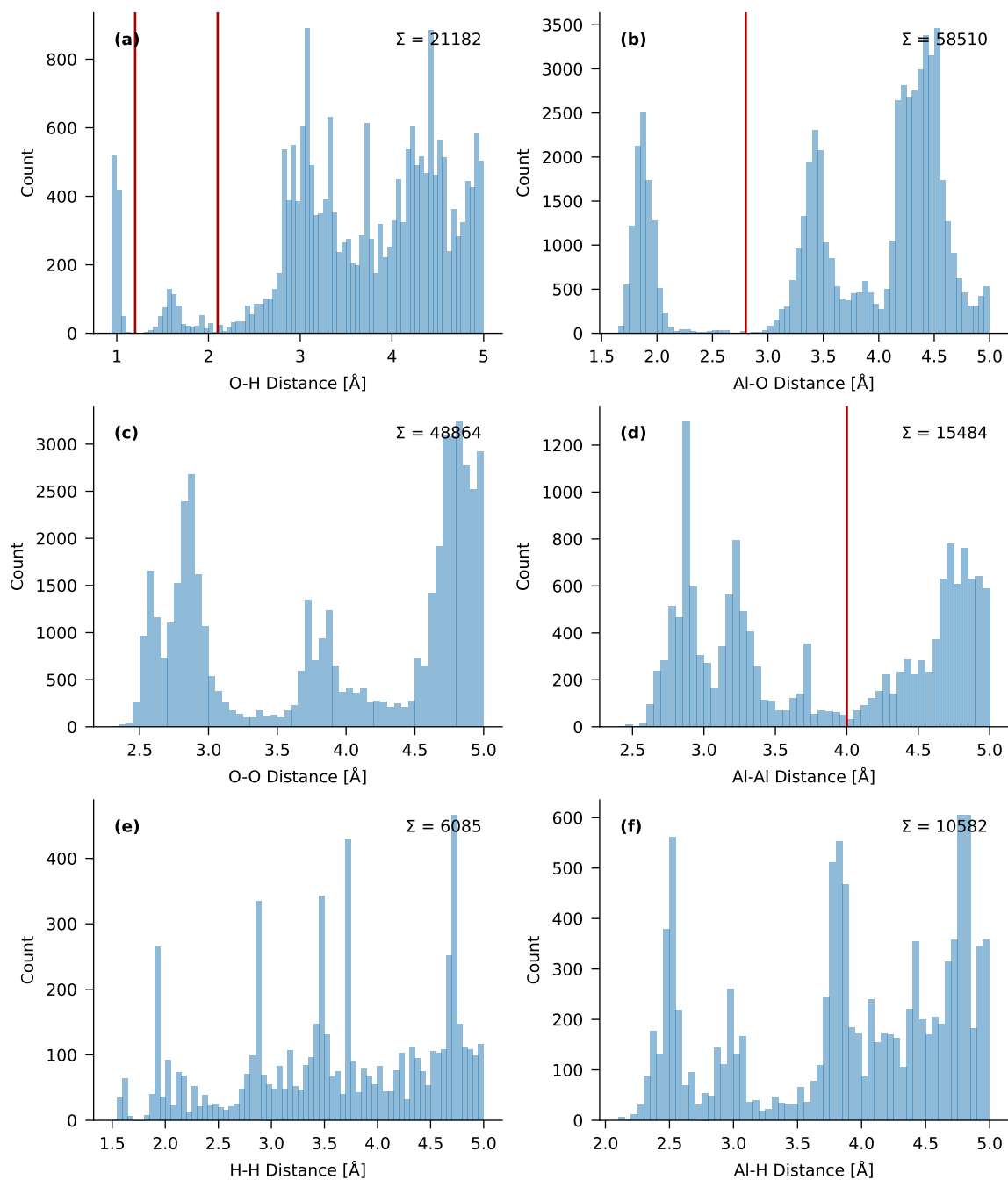


Figure S1: Histograms of all interatomic distances in the training set up to 5 Å, grouped per pair of chemical elements. Cutoffs for OH and AlO pairs depicted as vertical red lines: 1.2 Å for O–H bonds, 2.1 Å for hydrogen bonds and 2.8 Å for Al–O bonds. See main text for a more detailed description.

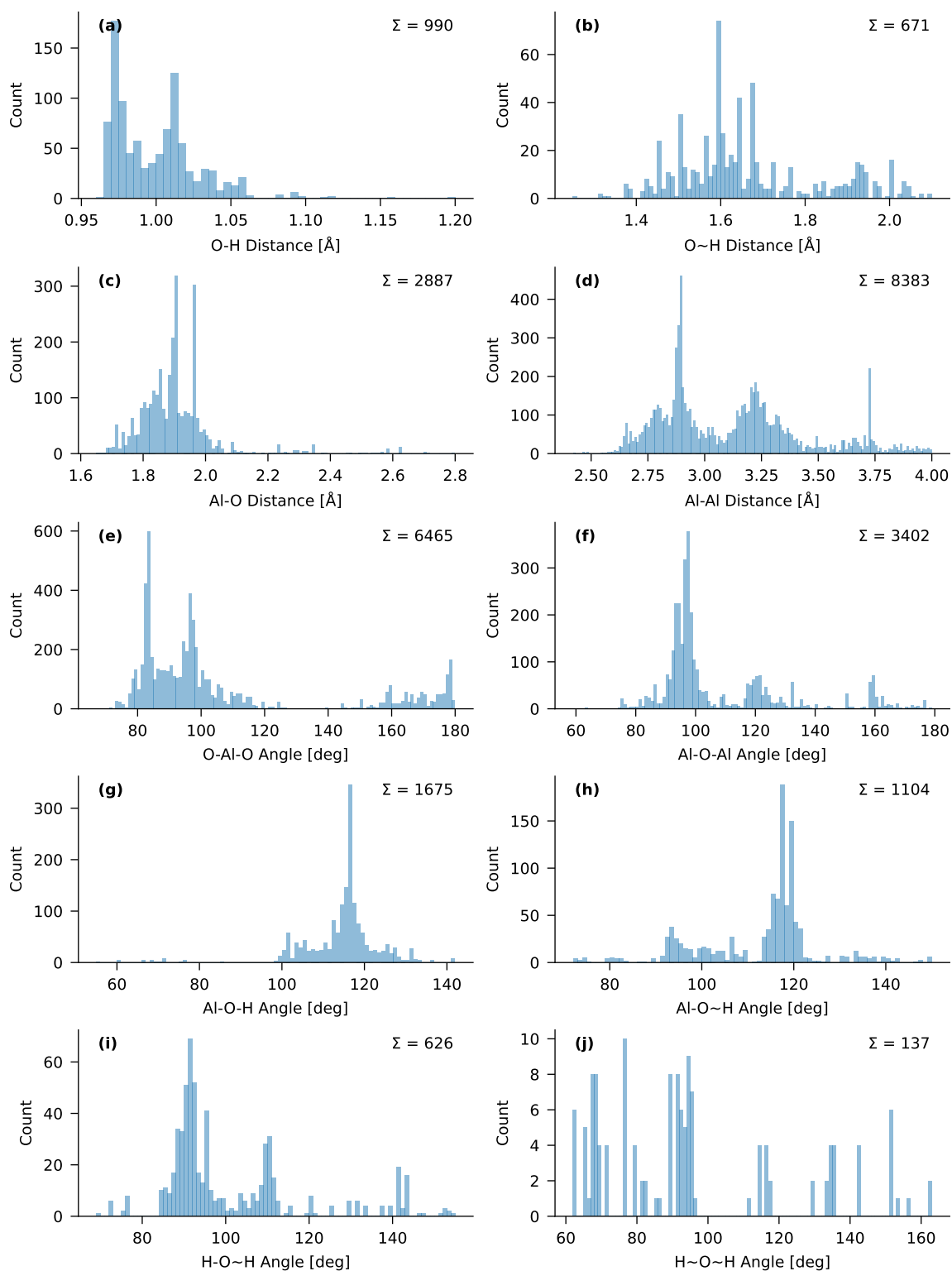


Figure S2: Histograms of internal coordinates in the training set. In the labels on the horizontal axis, a dash represents a regular bond and a tilde represents a hydrogen bond.

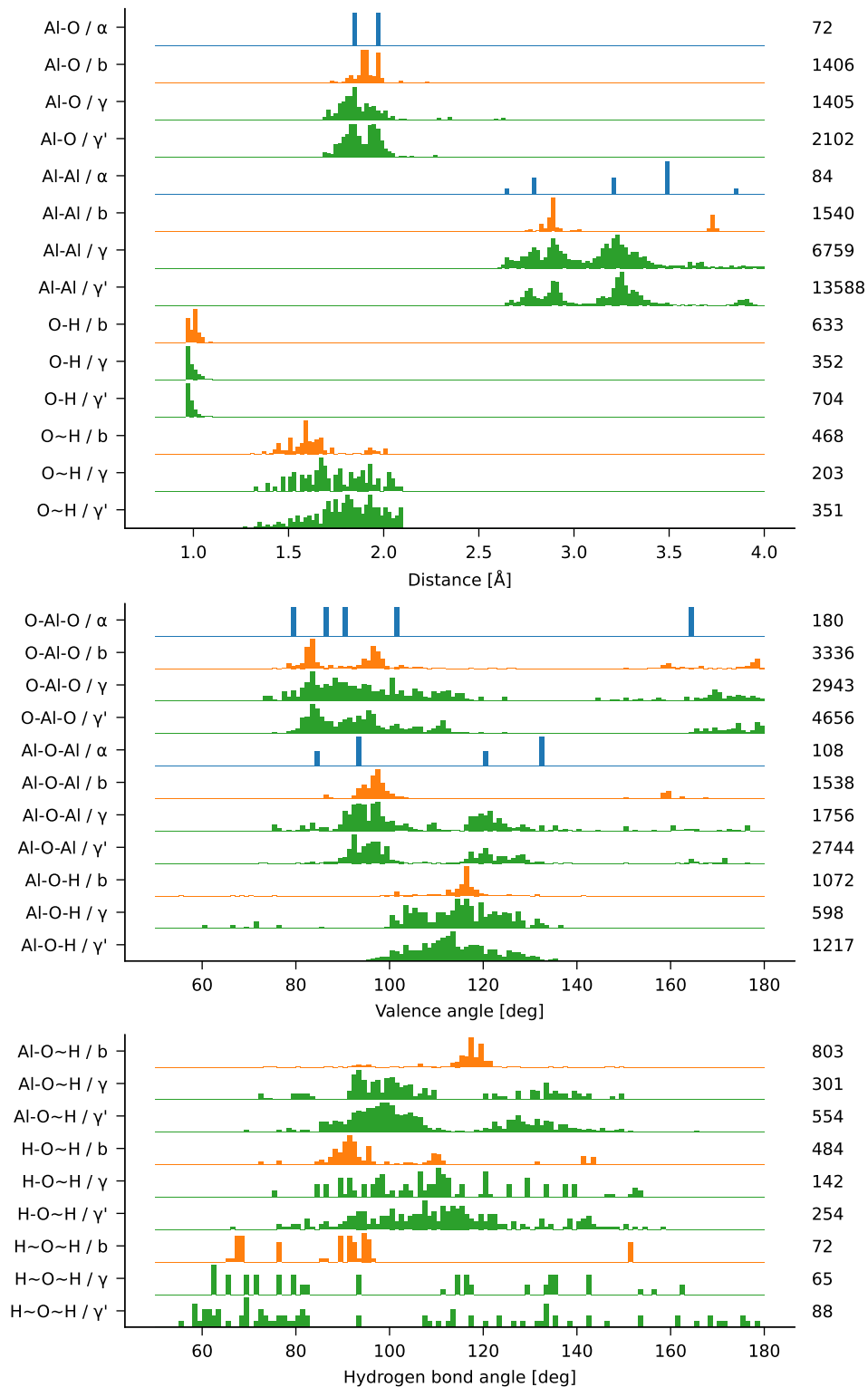


Figure S3: Histograms of internal coordinates, using the notation of Figure S2, per material. Histograms for the training set: $\alpha = \alpha\text{-Al}_2\text{O}_3$ (blue), b = boehmite (orange), $\gamma = \gamma\text{-Al}_2\text{O}_3$ (green). Histograms for the validation set: $\gamma' = \gamma\text{-Al}_2\text{O}_3$ (green). The number of internal coordinates within each class is shown to the right of the corresponding histogram.

Table S2: Overview of all chemical equations in the training set. Reactants are given negative coefficients. For each reaction, three reaction energies are in kcal mol^{-1} : the reference DFT result (R), the prediction with the Joshi force field (J) and the prediction with the new force field in this work (B). Water adsorption energies are normalized to the number of water molecules. All other reaction energies are normalized on the number of Al atoms. The categories are defined in the main text.

Category	Coeff.	Structure	Chem. Form.	Reaction energy
BSH	$-1/16\times$	boehm_surf-001_00w	$\text{Al}_{48} \text{O}_{96} \text{H}_{48}$	R -24.7
	$-1\times$	water	O H_2	J 28.0
	$1/16\times$	boehm_surf-001_08w	$\text{Al}_{48} \text{O}_{112} \text{H}_{80}$	B -21.9
BSH	$-1/24\times$	boehm_surf-100_00w	$\text{Al}_{48} \text{O}_{96} \text{H}_{48}$	R -46.0
	$-1\times$	water	O H_2	J -1.7
	$1/24\times$	boehm_surf-100_12w	$\text{Al}_{48} \text{O}_{120} \text{H}_{96}$	B -38.0
BSH	$-1/32\times$	boehm_surf-100_00w	$\text{Al}_{48} \text{O}_{96} \text{H}_{48}$	R -38.0
	$-1\times$	water	O H_2	J -4.2
	$1/32\times$	boehm_surf-100_16w	$\text{Al}_{48} \text{O}_{128} \text{H}_{112}$	B -32.2
BSH	$-1/8\times$	boehm_surf-100_12w	$\text{Al}_{48} \text{O}_{120} \text{H}_{96}$	R -14.0
	$-1\times$	water	O H_2	J -11.9
	$1/8\times$	boehm_surf-100_16w	$\text{Al}_{48} \text{O}_{128} \text{H}_{112}$	B -15.1
BSH	$-1/24\times$	boehm_surf-101_00w	$\text{Al}_{48} \text{O}_{96} \text{H}_{48}$	R -41.0
	$-1\times$	water	O H_2	J -4.3
	$1/24\times$	boehm_surf-101_12w	$\text{Al}_{48} \text{O}_{120} \text{H}_{96}$	B -39.3
GEH	$-1\times$	gamma_edge-100-110_00w	$\text{Al}_{96} \text{O}_{144}$	R -104.1
	$-1\times$	water	O H_2	J -101.6
	$1\times$	gamma_edge-100-110_01w	$\text{Al}_{96} \text{O}_{145} \text{H}_2$	B -103.0
GEH	$-1/2\times$	gamma_edge-100-110_00w	$\text{Al}_{96} \text{O}_{144}$	R -81.2
	$-1\times$	water	O H_2	J -86.6
	$1/2\times$	gamma_edge-100-110_02w	$\text{Al}_{96} \text{O}_{146} \text{H}_4$	B -80.3
GEH	$-1\times$	gamma_edge-100-110_01w	$\text{Al}_{96} \text{O}_{145} \text{H}_2$	R -58.3
	$-1\times$	water	O H_2	J -71.5
	$1\times$	gamma_edge-100-110_02w	$\text{Al}_{96} \text{O}_{146} \text{H}_4$	B -57.5
GEH	$-1/3\times$	gamma_edge-100-110_00w	$\text{Al}_{96} \text{O}_{144}$	R -72.1
	$-1\times$	water	O H_2	J -18.0
	$1/3\times$	gamma_edge-100-110_03w	$\text{Al}_{96} \text{O}_{147} \text{H}_6$	B -71.2
GEH	$-1/2\times$	gamma_edge-100-110_01w	$\text{Al}_{96} \text{O}_{145} \text{H}_2$	R -56.1
	$-1\times$	water	O H_2	J 23.8
	$1/2\times$	gamma_edge-100-110_03w	$\text{Al}_{96} \text{O}_{147} \text{H}_6$	B -55.3
GEH	$-1\times$	gamma_edge-100-110_02w	$\text{Al}_{96} \text{O}_{146} \text{H}_4$	R -53.9
	$-1\times$	water	O H_2	J 119.1
	$1\times$	gamma_edge-100-110_03w	$\text{Al}_{96} \text{O}_{147} \text{H}_6$	B -53.0
GEH	$-1/4\times$	gamma_edge-100-110_00w	$\text{Al}_{96} \text{O}_{144}$	R -67.5
	$-1\times$	water	O H_2	J -71.0

	1/4×	gamma_edge-100-110_04w	Al ₉₆ O ₁₄₈ H ₈	B	-67.0
GEH	-1/3×	gamma_edge-100-110_01w	Al ₉₆ O ₁₄₅ H ₂	R	-55.3
	-1×	water	O H ₂	J	-60.8
	1/3×	gamma_edge-100-110_04w	Al ₉₆ O ₁₄₈ H ₈	B	-55.0
GEH	-1/2×	gamma_edge-100-110_02w	Al ₉₆ O ₁₄₆ H ₄	R	-53.9
	-1×	water	O H ₂	J	-55.4
	1/2×	gamma_edge-100-110_04w	Al ₉₆ O ₁₄₈ H ₈	B	-53.7
GEH	-1×	gamma_edge-100-110_03w	Al ₉₆ O ₁₄₇ H ₆	R	-53.8
	-1×	water	O H ₂	J	-230.0
	1×	gamma_edge-100-110_04w	Al ₉₆ O ₁₄₈ H ₈	B	-54.5
GEH	-1/5×	gamma_edge-100-110_00w	Al ₉₆ O ₁₄₄	R	-63.3
	-1×	water	O H ₂	J	-22.9
	1/5×	gamma_edge-100-110_05w	Al ₉₆ O ₁₄₉ H ₁₀	B	-63.8
GEH	-1/4×	gamma_edge-100-110_01w	Al ₉₆ O ₁₄₅ H ₂	R	-53.1
	-1×	water	O H ₂	J	-3.2
	1/4×	gamma_edge-100-110_05w	Al ₉₆ O ₁₄₉ H ₁₀	B	-54.0
GEH	-1/3×	gamma_edge-100-110_02w	Al ₉₆ O ₁₄₆ H ₄	R	-51.4
	-1×	water	O H ₂	J	19.5
	1/3×	gamma_edge-100-110_05w	Al ₉₆ O ₁₄₉ H ₁₀	B	-52.8
GEH	-1/2×	gamma_edge-100-110_03w	Al ₉₆ O ₁₄₇ H ₆	R	-50.2
	-1×	water	O H ₂	J	-30.3
	1/2×	gamma_edge-100-110_05w	Al ₉₆ O ₁₄₉ H ₁₀	B	-52.7
GEH	-1×	gamma_edge-100-110_04w	Al ₉₆ O ₁₄₈ H ₈	R	-46.6
	-1×	water	O H ₂	J	169.4
	1×	gamma_edge-100-110_05w	Al ₉₆ O ₁₄₉ H ₁₀	B	-51.0
GEH	-1/7×	gamma_edge-100-110_00w	Al ₉₆ O ₁₄₄	R	-55.8
	-1×	water	O H ₂	J	-12.6
	1/7×	gamma_edge-100-110_07w	Al ₉₆ O ₁₅₁ H ₁₄	B	-57.1
GEH	-1/6×	gamma_edge-100-110_01w	Al ₉₆ O ₁₄₅ H ₂	R	-47.8
	-1×	water	O H ₂	J	2.2
	1/6×	gamma_edge-100-110_07w	Al ₉₆ O ₁₅₁ H ₁₄	B	-49.5
GEH	-1/5×	gamma_edge-100-110_02w	Al ₉₆ O ₁₄₆ H ₄	R	-45.7
	-1×	water	O H ₂	J	16.9
	1/5×	gamma_edge-100-110_07w	Al ₉₆ O ₁₅₁ H ₁₄	B	-47.9
GEH	-1/4×	gamma_edge-100-110_03w	Al ₉₆ O ₁₄₇ H ₆	R	-43.6
	-1×	water	O H ₂	J	-8.6
	1/4×	gamma_edge-100-110_07w	Al ₉₆ O ₁₅₁ H ₁₄	B	-46.6
GEH	-1/3×	gamma_edge-100-110_04w	Al ₉₆ O ₁₄₈ H ₈	R	-40.2
	-1×	water	O H ₂	J	65.1
	1/3×	gamma_edge-100-110_07w	Al ₉₆ O ₁₅₁ H ₁₄	B	-43.9
GEH	-1/2×	gamma_edge-100-110_05w	Al ₉₆ O ₁₄₉ H ₁₀	R	-37.0
	-1×	water	O H ₂	J	13.0
	1/2×	gamma_edge-100-110_07w	Al ₉₆ O ₁₅₁ H ₁₄	B	-40.4
GSH	-1/4×	gamma_surf-100_00w	Al ₆₄ O ₉₆	R	-24.0

	-1×	water	O H ₂	J	-2.0
	1/4×	gamma_surf-100_01w	Al ₆₄ O ₁₀₀ H ₈	B	-23.8
GSH	-1/8×	gamma_surf-100_00w	Al ₆₄ O ₉₆	R	-25.0
	-1×	water	O H ₂	J	-10.7
	1/8×	gamma_surf-100_02w	Al ₆₄ O ₁₀₄ H ₁₆	B	-26.0
GSH	-1/4×	gamma_surf-100_01w	Al ₆₄ O ₁₀₀ H ₈	R	-26.0
	-1×	water	O H ₂	J	-19.5
	1/4×	gamma_surf-100_02w	Al ₆₄ O ₁₀₄ H ₁₆	B	-28.2
GSH	-1/12×	gamma_surf-100_00w	Al ₆₄ O ₉₆	R	-24.3
	-1×	water	O H ₂	J	-6.8
	1/12×	gamma_surf-100_03w	Al ₆₄ O ₁₀₈ H ₂₄	B	-26.8
GSH	-1/8×	gamma_surf-100_01w	Al ₆₄ O ₁₀₀ H ₈	R	-24.4
	-1×	water	O H ₂	J	-9.2
	1/8×	gamma_surf-100_03w	Al ₆₄ O ₁₀₈ H ₂₄	B	-28.3
GSH	-1/4×	gamma_surf-100_02w	Al ₆₄ O ₁₀₄ H ₁₆	R	-22.8
	-1×	water	O H ₂	J	1.1
	1/4×	gamma_surf-100_03w	Al ₆₄ O ₁₀₈ H ₂₄	B	-28.3
GSH	-1/16×	gamma_surf-100_00w	Al ₆₄ O ₉₆	R	-21.7
	-1×	water	O H ₂	J	-3.6
	1/16×	gamma_surf-100_04w	Al ₆₄ O ₁₁₂ H ₃₂	B	-22.4
GSH	-1/12×	gamma_surf-100_01w	Al ₆₄ O ₁₀₀ H ₈	R	-21.0
	-1×	water	O H ₂	J	-4.1
	1/12×	gamma_surf-100_04w	Al ₆₄ O ₁₁₂ H ₃₂	B	-22.0
GSH	-1/8×	gamma_surf-100_02w	Al ₆₄ O ₁₀₄ H ₁₆	R	-18.5
	-1×	water	O H ₂	J	3.5
	1/8×	gamma_surf-100_04w	Al ₆₄ O ₁₁₂ H ₃₂	B	-18.8
GSH	-1/4×	gamma_surf-100_03w	Al ₆₄ O ₁₀₈ H ₂₄	R	-14.1
	-1×	water	O H ₂	J	6.0
	1/4×	gamma_surf-100_04w	Al ₆₄ O ₁₁₂ H ₃₂	B	-9.3
GSH	-1/4×	gamma_surf-110_00w	Al ₆₄ O ₉₆	R	-92.4
	-1×	water	O H ₂	J	50.4
	1/4×	gamma_surf-110_01w	Al ₆₄ O ₁₀₀ H ₈	B	-108.6
GSH	-1/8×	gamma_surf-110_00w	Al ₆₄ O ₉₆	R	-50.2
	-1×	water	O H ₂	J	7.3
	1/8×	gamma_surf-110_02w	Al ₆₄ O ₁₀₄ H ₁₆	B	-61.8
GSH	-1/4×	gamma_surf-110_01w	Al ₆₄ O ₁₀₀ H ₈	R	-8.0
	-1×	water	O H ₂	J	-35.8
	1/4×	gamma_surf-110_02w	Al ₆₄ O ₁₀₄ H ₁₆	B	-15.0
GSH	-1/12×	gamma_surf-110_00w	Al ₆₄ O ₉₆	R	-42.5
	-1×	water	O H ₂	J	42.3
	1/12×	gamma_surf-110_03w	Al ₆₄ O ₁₀₈ H ₂₄	B	-50.1
GSH	-1/8×	gamma_surf-110_01w	Al ₆₄ O ₁₀₀ H ₈	R	-17.6
	-1×	water	O H ₂	J	38.2
	1/8×	gamma_surf-110_03w	Al ₆₄ O ₁₀₈ H ₂₄	B	-20.8

GSH	-1/4×	gamma_surf-110_02w	Al ₆₄ O ₁₀₄ H ₁₆	R	-27.2
	-1×	water	O H ₂	J	112.3
	1/4×	gamma_surf-110_03w	Al ₆₄ O ₁₀₈ H ₂₄	B	-26.7
GSH	-1/16×	gamma_surf-110_00w	Al ₆₄ O ₉₆	R	-39.6
	-1×	water	O H ₂	J	28.9
	1/16×	gamma_surf-110_04w	Al ₆₄ O ₁₁₂ H ₃₂	B	-44.9
GSH	-1/12×	gamma_surf-110_01w	Al ₆₄ O ₁₀₀ H ₈	R	-22.1
	-1×	water	O H ₂	J	21.7
	1/12×	gamma_surf-110_04w	Al ₆₄ O ₁₁₂ H ₃₂	B	-23.7
GSH	-1/8×	gamma_surf-110_02w	Al ₆₄ O ₁₀₄ H ₁₆	R	-29.1
	-1×	water	O H ₂	J	50.5
	1/8×	gamma_surf-110_04w	Al ₆₄ O ₁₁₂ H ₃₂	B	-28.1
GSH	-1/4×	gamma_surf-110_03w	Al ₆₄ O ₁₀₈ H ₂₄	R	-31.0
	-1×	water	O H ₂	J	-11.3
	1/4×	gamma_surf-110_04w	Al ₆₄ O ₁₁₂ H ₃₂	B	-29.5
GSH	-1/20×	gamma_surf-110_00w	Al ₆₄ O ₉₆	R	-35.2
	-1×	water	O H ₂	J	16.0
	1/20×	gamma_surf-110_05w	Al ₆₄ O ₁₁₆ H ₄₀	B	-39.4
GSH	-1/16×	gamma_surf-110_01w	Al ₆₄ O ₁₀₀ H ₈	R	-20.9
	-1×	water	O H ₂	J	7.4
	1/16×	gamma_surf-110_05w	Al ₆₄ O ₁₁₆ H ₄₀	B	-22.1
GSH	-1/12×	gamma_surf-110_02w	Al ₆₄ O ₁₀₄ H ₁₆	R	-25.1
	-1×	water	O H ₂	J	21.9
	1/12×	gamma_surf-110_05w	Al ₆₄ O ₁₁₆ H ₄₀	B	-24.5
GSH	-1/8×	gamma_surf-110_03w	Al ₆₄ O ₁₀₈ H ₂₄	R	-24.1
	-1×	water	O H ₂	J	-23.4
	1/8×	gamma_surf-110_05w	Al ₆₄ O ₁₁₆ H ₄₀	B	-23.4
GSH	-1/4×	gamma_surf-110_04w	Al ₆₄ O ₁₁₂ H ₃₂	R	-17.3
	-1×	water	O H ₂	J	-35.4
	1/4×	gamma_surf-110_05w	Al ₆₄ O ₁₁₆ H ₄₀	B	-17.2
GSH	-1/24×	gamma_surf-110_00w	Al ₆₄ O ₉₆	R	-33.5
	-1×	water	O H ₂	J	21.5
	1/24×	gamma_surf-110_06w	Al ₆₄ O ₁₂₀ H ₄₈	B	-37.5
GSH	-1/20×	gamma_surf-110_01w	Al ₆₄ O ₁₀₀ H ₈	R	-21.7
	-1×	water	O H ₂	J	15.8
	1/20×	gamma_surf-110_06w	Al ₆₄ O ₁₂₀ H ₄₈	B	-23.3
GSH	-1/16×	gamma_surf-110_02w	Al ₆₄ O ₁₀₄ H ₁₆	R	-25.1
	-1×	water	O H ₂	J	28.7
	1/16×	gamma_surf-110_06w	Al ₆₄ O ₁₂₀ H ₄₈	B	-25.3
GSH	-1/12×	gamma_surf-110_03w	Al ₆₄ O ₁₀₈ H ₂₄	R	-24.4
	-1×	water	O H ₂	J	0.8
	1/12×	gamma_surf-110_06w	Al ₆₄ O ₁₂₀ H ₄₈	B	-24.9
GSH	-1/8×	gamma_surf-110_04w	Al ₆₄ O ₁₁₂ H ₃₂	R	-21.1
	-1×	water	O H ₂	J	6.8

	1/8×	gamma_surf-110_06w	Al ₆₄ O ₁₂₀ H ₄₈	B	-22.6
GSH	-1/4×	gamma_surf-110_05w	Al ₆₄ O ₁₁₆ H ₄₀	R	-24.9
	-1×	water	O H ₂	J	49.1
	1/4×	gamma_surf-110_06w	Al ₆₄ O ₁₂₀ H ₄₈	B	-27.9
GSH	-1/10×	gamma_surf-111_00w	Al ₄₀ O ₆₀	R	-42.1
	-1×	water	O H ₂	J	7.2
	1/8×	gamma_surf-111_04w	Al ₃₂ O ₅₆ H ₁₆	B	-31.1
GSH	-2/25×	gamma_surf-111_00w	Al ₄₀ O ₆₀	R	-45.8
	-1×	water	O H ₂	J	5.6
	1/10×	gamma_surf-111_05w	Al ₃₂ O ₅₈ H ₂₀	B	-32.8
GSH	-1/2×	gamma_surf-111_04w	Al ₃₂ O ₅₆ H ₁₆	R	-60.5
	-1×	water	O H ₂	J	-0.7
	1/2×	gamma_surf-111_05w	Al ₃₂ O ₅₈ H ₂₀	B	-39.8
GSH	-1/15×	gamma_surf-111_00w	Al ₄₀ O ₆₀	R	-43.1
	-1×	water	O H ₂	J	13.5
	1/12×	gamma_surf-111_06w	Al ₃₂ O ₆₀ H ₂₄	B	-32.5
GSH	-1/4×	gamma_surf-111_04w	Al ₃₂ O ₅₆ H ₁₆	R	-45.0
	-1×	water	O H ₂	J	26.2
	1/4×	gamma_surf-111_06w	Al ₃₂ O ₆₀ H ₂₄	B	-35.3
GSH	-1/2×	gamma_surf-111_05w	Al ₃₂ O ₅₈ H ₂₀	R	-29.4
	-1×	water	O H ₂	J	53.2
	1/2×	gamma_surf-111_06w	Al ₃₂ O ₆₀ H ₂₄	B	-30.9
SUR	-1/32×	boehm_bulk	Al ₃₂ O ₆₄ H ₃₂	R	11.2
	1/48×	boehm_surf-001_00w	Al ₄₈ O ₉₆ H ₄₈	J	5.5
				B	9.0
SUR	-1/32×	boehm_bulk	Al ₃₂ O ₆₄ H ₃₂	R	2.9
	1/72×	boehm_surf-010_00w	Al ₇₂ O ₁₄₄ H ₇₂	J	2.1
				B	3.1
SUR	-1/32×	boehm_bulk	Al ₃₂ O ₆₄ H ₃₂	R	23.0
	1/48×	boehm_surf-100_00w	Al ₄₈ O ₉₆ H ₄₈	J	-0.4
				B	19.1
SUR	-1/32×	boehm_bulk	Al ₃₂ O ₆₄ H ₃₂	R	18.6
	1/48×	boehm_surf-101_00w	Al ₄₈ O ₉₆ H ₄₈	J	7.5
				B	16.4
SUR	-1/16×	gamma_bulk	Al ₁₆ O ₂₄	R	13.5
	1/96×	gamma_edge-100-110_00w	Al ₉₆ O ₁₄₄	J	7.0
				B	14.0
SUR	-1/16×	gamma_bulk	Al ₁₆ O ₂₄	R	10.4
	1/64×	gamma_surf-100_00w	Al ₆₄ O ₉₆	J	6.6
				B	13.0
SUR	-1/16×	gamma_bulk	Al ₁₆ O ₂₄	R	21.2
	1/64×	gamma_surf-110_00w	Al ₆₄ O ₉₆	J	7.4
				B	26.6
SUR	-1/16×	gamma_bulk	Al ₁₆ O ₂₄	R	13.5

	1/40×	gamma_surf-111_00w	Al ₄₀ O ₆₀	J	5.6
				B	11.1
FOR	-1×	monomer	Al O ₄ H ₅	R	-27.8
	1/12×	alpha_bulk	Al ₁₂ O ₁₈	J	-44.9
	5/2×	water	O H ₂	B	-31.9
FOR	-1×	monomer	Al O ₄ H ₅	R	-38.8
	1/32×	boehm_bulk	Al ₃₂ O ₆₄ H ₃₂	J	-38.6
	2×	water	O H ₂	B	-36.5
FOR	-1×	monomer	Al O ₄ H ₅	R	-27.6
	1/48×	boehm_surf-001_00w	Al ₄₈ O ₉₆ H ₄₈	J	-33.1
	2×	water	O H ₂	B	-27.4
FOR	-1×	monomer	Al O ₄ H ₅	R	-35.9
	1/72×	boehm_surf-010_00w	Al ₇₂ O ₁₄₄ H ₇₂	J	-36.5
	2×	water	O H ₂	B	-33.4
FOR	-1×	monomer	Al O ₄ H ₅	R	-15.8
	1/48×	boehm_surf-100_00w	Al ₄₈ O ₉₆ H ₄₈	J	-39.0
	2×	water	O H ₂	B	-17.4
FOR	-1×	monomer	Al O ₄ H ₅	R	-20.2
	1/48×	boehm_surf-101_00w	Al ₄₈ O ₉₆ H ₄₈	J	-31.1
	2×	water	O H ₂	B	-20.1
FOR	-1×	monomer	Al O ₄ H ₅	R	-25.3
	1/16×	gamma_bulk	Al ₁₆ O ₂₄	J	-48.6
	5/2×	water	O H ₂	B	-26.4
FOR	-1×	monomer	Al O ₄ H ₅	R	-11.7
	1/96×	gamma_edge-100-110_00w	Al ₉₆ O ₁₄₄	J	-41.6
	5/2×	water	O H ₂	B	-12.4
FOR	-1×	monomer	Al O ₄ H ₅	R	-14.8
	1/64×	gamma_surf-100_00w	Al ₆₄ O ₉₆	J	-42.0
	5/2×	water	O H ₂	B	-13.4
FOR	-1×	monomer	Al O ₄ H ₅	R	-4.1
	1/64×	gamma_surf-110_00w	Al ₆₄ O ₉₆	J	-41.2
	5/2×	water	O H ₂	B	0.2
FOR	-1×	monomer	Al O ₄ H ₅	R	-11.7
	1/40×	gamma_surf-111_00w	Al ₄₀ O ₆₀	J	-43.0
	5/2×	water	O H ₂	B	-15.3

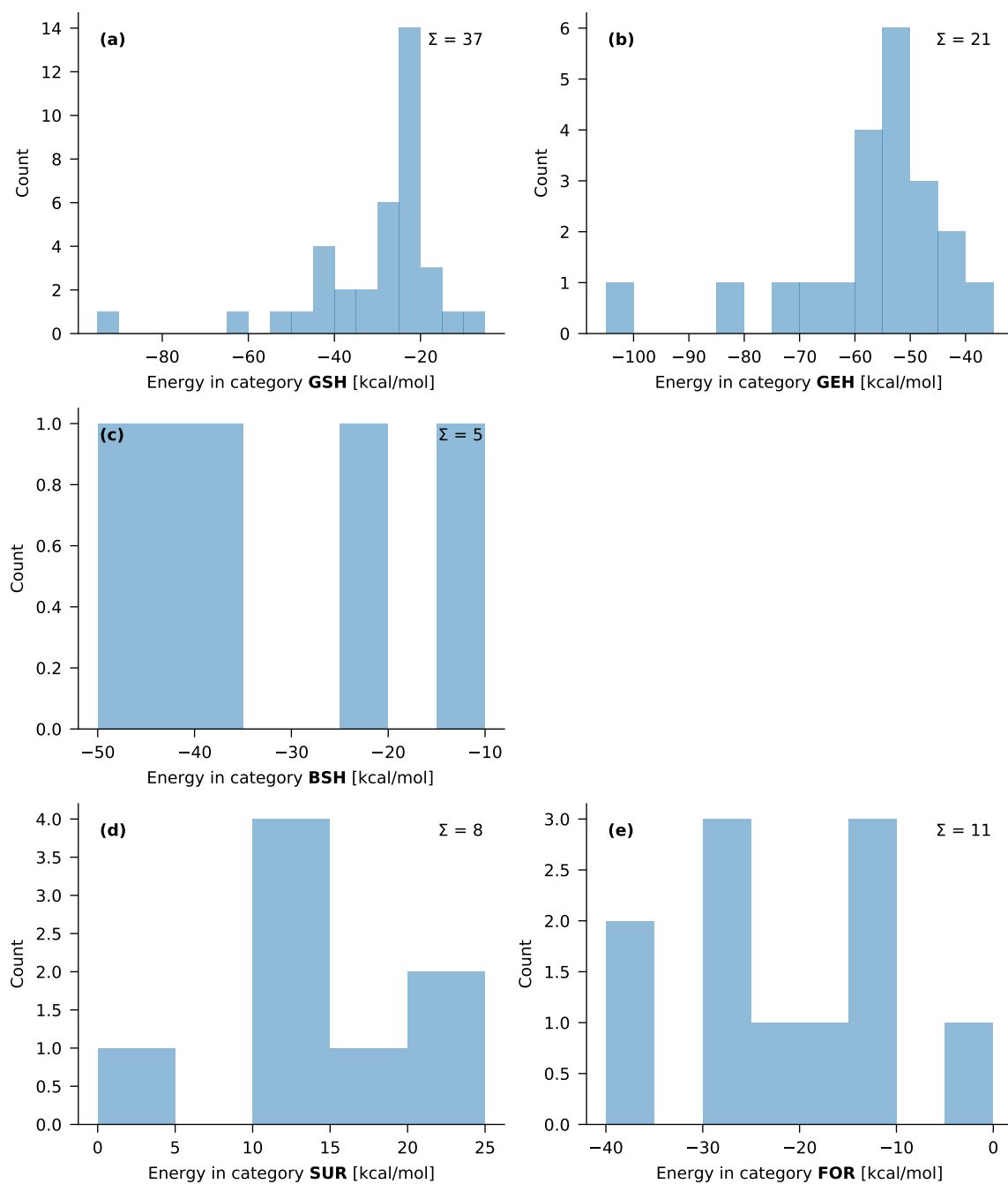


Figure S4: Histograms of reaction energies in the training set.

Table S3: List of activated parameters and their corresponding block, initial values from 1 and bounds.

Name	Unit	Atoms	Block	Joshi 2014	Lower bound	Upper bound	This work
p_val3	1	Al	ATM	1.5000	1.2000	3.0000	2.9993
p_val5	1	Al	ATM	2.5791	2.0633	3.0949	2.4980
D_e ^{sigma}	kcal mol ⁻¹	Al-H	BND	92.8579	0.8579	122.7844	77.1779
p_be1	1	Al-H	BND	-0.6528	-0.7834	1.0000	-0.7823
p_ovun1	1	Al-H	BND	0.1551	0.0100	0.5000	0.3089
p_be2	1	Al-H	BND	10.0663	0.2281	13.0000	2.0985
p_bo1	1	Al-H	BND	-0.0842	-0.3320	-0.0674	-0.1398
p_bo2	1	Al-H	BND	7.1758	5.0015	15.0000	11.7930
D_e ^{sigma}	kcal mol ⁻¹	Al-O	BND	182.0654	118.9203	232.7313	166.4329
p_be1	1	Al-O	BND	-0.0920	-1.0000	-0.0736	-0.0963
p_ovun1	1	Al-O	BND	0.1688	0.0100	0.4562	0.1457
p_be2	1	Al-O	BND	0.0010	0.0008	1.5477	0.7025
p_bo1	1	Al-O	BND	-0.1959	-0.2351	-0.0740	-0.2053
p_bo2	1	Al-O	BND	6.0894	4.6533	7.3073	7.1635
D_e ^{sigma}	kcal mol ⁻¹	Al-Al	BND	34.0777	27.2622	65.7742	31.9434
r_0 ^{sigma}	Å	Al-H	OFD	1.7276	1.3821	2.0731	1.4893
r_0 ^{sigma}	Å	Al-O	OFD	1.5646	1.2517	1.8775	1.6172
p_val1	1	Al-H-O	ANG	4.2750	3.4200	20.0000	19.7283
p_val2	1	Al-H-O	ANG	1.0250	0.8200	4.8339	3.9208
p_val4	1	Al-H-O	ANG	1.4750	1.0100	1.7700	1.0931
Theta_0,0	deg	Al-O-H	ANG	88.6163	64.6197	106.3396	66.0975
p_val1	1	Al-O-H	ANG	10.1310	4.2037	19.7491	16.7556
p_val2	1	Al-O-H	ANG	1.6896	1.3517	10.0000	2.4332
p_val4	1	Al-O-H	ANG	1.0000	0.8000	3.0000	1.4778
Theta_0,0	deg	Al-O-Al	ANG	13.8580	5.2474	64.5513	64.5486
p_val1	1	Al-O-Al	ANG	12.3669	9.8935	40.0000	12.8201
p_val2	1	Al-O-Al	ANG	4.4355	0.5527	9.9945	7.0734
p_val4	1	Al-O-Al	ANG	1.1908	0.9526	3.0000	2.9786
Theta_0,0	deg	H-Al-O	ANG	41.8108	0.0000	64.8437	9.7233
p_val1	1	H-Al-O	ANG	17.3800	5.4547	30.9495	23.4162
p_val2	1	H-Al-O	ANG	2.6618	0.9702	3.1942	3.0390
p_val4	1	H-Al-O	ANG	1.0100	0.8080	3.0000	1.0218
Theta_0,0	deg	O-Al-O	ANG	55.4358	43.7395	84.7469	61.5592
p_val1	1	O-Al-O	ANG	22.1089	7.3926	40.0000	24.2337
p_val2	1	O-Al-O	ANG	3.7402	1.2450	4.4882	1.2622
p_val4	1	O-Al-O	ANG	2.2064	1.0123	3.0000	2.9975

Table S4: Structures in the validation set and contributions to each category of data. Bonds are represented by pairs of chemical elements, angles by triplets. The symbol \cdots denotes a hydrogen bond. Internal coordinates with oxygen not bound to aluminum are discarded. For hydrated alumina surfaces, the internal coordinates without hydrogen are not considered.

Structure	Chem. Form.	O-H	O \cdots H	Al-O	Al-Al	O-Al-O	Al-O-Al	Al-O-H	Al-O \cdots H	H-O \cdots H	H \cdots O \cdots H
gamma_bulk	Al ₃₂ O ₄₈			176	176	408	240				
gamma_surf-001_00w	Al ₆₄ O ₉₆			336	316	736	432				
gamma_surf-001_01w	Al ₆₄ O ₉₈ H ₄	4	2		316			8	2	2	
gamma_surf-001_02w	Al ₆₄ O ₁₀₀ H ₈	8	4		318			12	4	4	2
gamma_surf-001_03w	Al ₆₄ O ₁₀₂ H ₁₂	12	8		316			20	8	8	4
gamma_surf-001_04w	Al ₆₄ O ₁₀₄ H ₁₆	16	10		316			26	14	10	4
gamma_surf-110b_from_boehm_00w	Al ₈₀ O ₁₂₀			414	416	902	532				
gamma_surf-110b_from_boehm_02w	Al ₈₀ O ₁₂₄ H ₈	8			436			16			
gamma_surf-110b_from_boehm_03w	Al ₈₀ O ₁₂₆ H ₁₂	12			436			22			
gamma_surf-110b_from_boehm_04w	Al ₈₀ O ₁₂₈ H ₁₆	16	8		436			24	8	8	
gamma_surf-110b_from_bulk_00w	Al ₆₄ O ₉₆			336	324	744	440				
gamma_surf-110b_from_bulk_02w	Al ₆₄ O ₉₈ H ₄	4	2		324			6	4		
gamma_surf-110b_from_bulk_04w	Al ₆₄ O ₁₀₀ H ₈	8	4		324			12	4	4	
gamma_surf-110b_from_bulk_06w	Al ₆₄ O ₁₀₂ H ₁₂	12	6		324			16	10	4	
gamma_surf-110b_from_bulk_08w	Al ₆₄ O ₁₀₄ H ₁₆	16	10		324			20	18	6	2
gamma_surf-1101_A1_00w	Al ₄₈ O ₇₂			250	238	552	324				
gamma_surf-1101_A1_01w	Al ₄₈ O ₇₄ H ₄	4	2		234			8	4		
gamma_surf-1101_A1_02w	Al ₄₈ O ₇₆ H ₈	8	4		240			14	6	2	
gamma_surf-1101_A1_03w	Al ₄₈ O ₇₈ H ₁₂	12	4		240			22	6	4	
gamma_surf-1101_A1_04w	Al ₄₈ O ₈₀ H ₁₆	16	12		236			26	22	6	4
gamma_surf-1101_A1_05w	Al ₄₈ O ₈₂ H ₂₀	20	14		236			30	26	8	4
gamma_surf-1101_A1_06w	Al ₄₈ O ₈₄ H ₂₄	24	17		236			30	37	4	9
gamma_surf-1101_A2_00w	Al ₅₆ O ₈₄			296	276	660	392				
gamma_surf-1101_A2_01w	Al ₅₆ O ₈₆ H ₄	4	2		274			8	4		
gamma_surf-1101_A2_02w	Al ₅₆ O ₈₈ H ₈	8	4		282			14	8		2
gamma_surf-1101_A2_03w	Al ₅₆ O ₉₀ H ₁₂	12	7		284			20	11	5	1
gamma_surf-1101_A2_04w	Al ₅₆ O ₉₂ H ₁₆	16	10		284			24	18	8	
gamma_surf-1101_A2_05w	Al ₅₆ O ₉₄ H ₂₀	20	14		282			26	30	4	6
gamma_surf-1101_A2_06w	Al ₅₆ O ₉₆ H ₂₄	24	18		282			30	38	6	8
gamma_surf-1101_L1_04w	Al ₄₈ O ₈₀ H ₁₆	16	6		240			32	12	4	
gamma_surf-1101_L2_00w	Al ₅₆ O ₈₄			294	286	654	384				
gamma_surf-1101_L2_01w	Al ₅₆ O ₈₆ H ₄	4	2		276			8	4		
gamma_surf-1101_L2_02w	Al ₅₆ O ₈₈ H ₈	8	4		282			14	8		2
gamma_surf-1101_L2_03w	Al ₅₆ O ₉₀ H ₁₂	12	4		282			22	10	2	
gamma_surf-1101_L2_04w	Al ₅₆ O ₉₂ H ₁₆	16	6		282			32	16	2	
gamma_surf-111_D1_03w	Al ₃₂ O ₅₄ H ₁₂	12	5		144			22	6	4	2
gamma_surf-111_D1_04w	Al ₃₂ O ₅₆ H ₁₆	16	5		146			30	6	5	2
gamma_surf-111_D1_05w	Al ₃₂ O ₅₈ H ₂₀	20	10		146			36	14	10	2
gamma_surf-111_D1_06w	Al ₃₂ O ₆₀ H ₂₄	24	14		146			44	17	14	5
gamma_surf-111_D2_03w	Al ₃₂ O ₅₄ H ₁₂	12	8		144			22	12	4	2
gamma_surf-111_D2_04w	Al ₃₂ O ₅₆ H ₁₆	16	9		146			30	14	7	2

gamma_surf-111_D2_05w	Al ₃₂ O ₅₈ H ₂₀	20	12		146			36	15	12	6
gamma_surf-111_D2_06w	Al ₃₂ O ₆₀ H ₂₄	24	15		146			44	18	15	6
gamma_surf-111_P1_1_05w	Al ₄₀ O ₇₀ H ₂₀	20	3		184			43	6	3	
gamma_surf-111_P1_1_06w	Al ₄₀ O ₇₂ H ₂₄	24	4		178			54	8	4	
gamma_surf-111_P1_2_03w	Al ₄₀ O ₆₆ H ₁₂	12	2		178			24	4	2	
gamma_surf-111_P1_2_04w	Al ₄₀ O ₆₈ H ₁₆	16	4		178			34	8	4	
gamma_surf-111_P1_2_05w	Al ₄₀ O ₇₀ H ₂₀	20	5		178			44	10	5	
gamma_surf-111_P1_2_06w	Al ₄₀ O ₇₂ H ₂₄	24	2		182			54	4	2	
gamma_surf-111_P2_1_05w	Al ₄₀ O ₇₀ H ₂₀	20	14		196			27	15	13	4
gamma_surf-111_P2_1_06w	Al ₄₀ O ₇₂ H ₂₄	24	16		200			38	16	16	4
gamma_surf-111_P2_2_04w	Al ₄₀ O ₆₈ H ₁₆	16	10		194			26	16	6	
gamma_surf-111_P2_2_05w	Al ₄₀ O ₇₀ H ₂₀	20	14		190			32	18	12	3
gamma_surf-111_P2_2_06w	Al ₄₀ O ₇₂ H ₂₄	24	15		192			35	15	15	2
water	O H ₂										
total		704	351	2102	13 588	4656	2744	1217	554	254	88

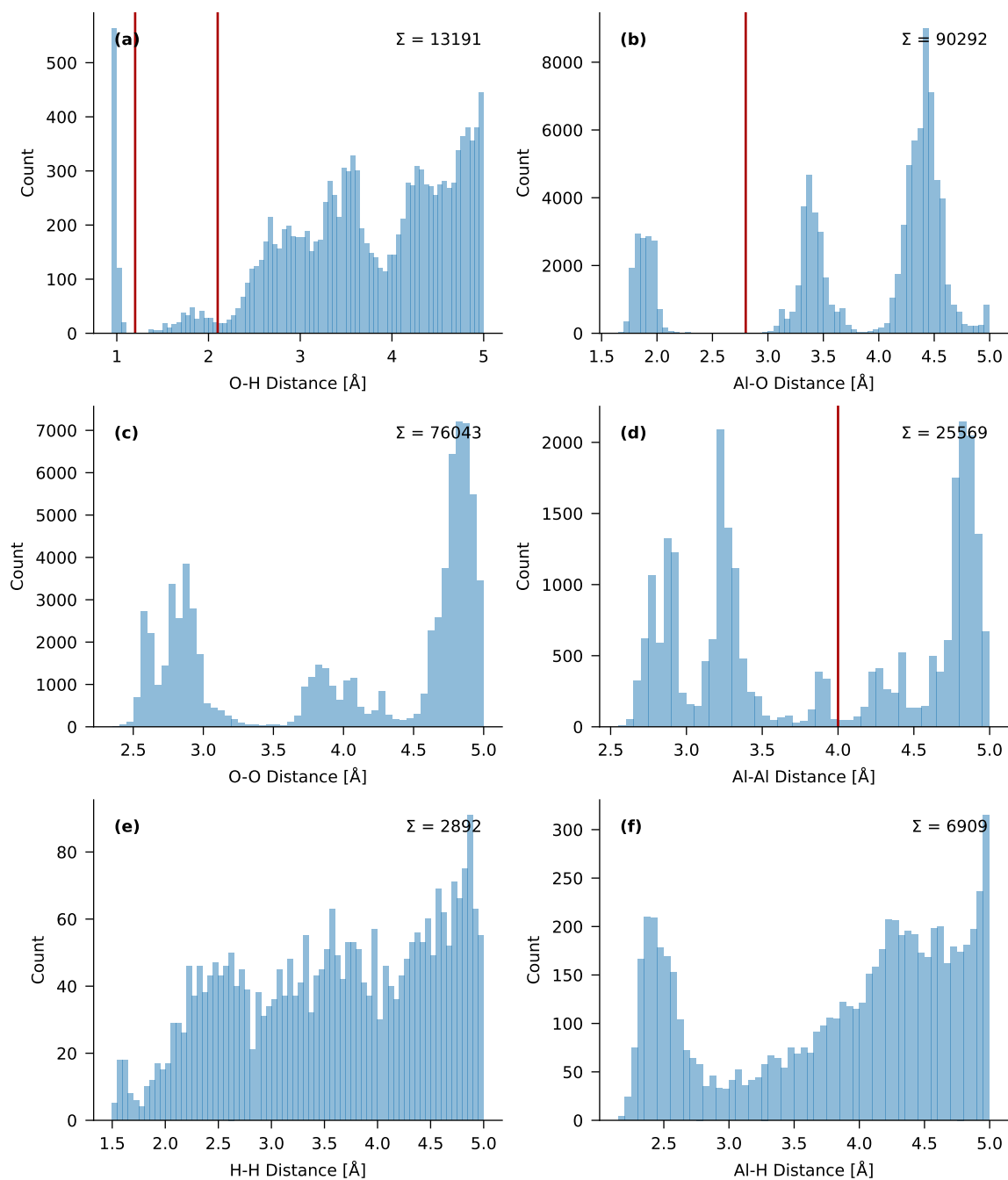


Figure S5: Histograms of all interatomic distances in the validation set up to 5 Å, grouped per pair of chemical elements. Cutoffs for OH and AlO pairs depicted as vertical red lines: 1.2 Å for O–H bonds, 2.1 Å for hydrogen bonds and 2.8 Å for Al–O bonds. See main text for a more detailed description.

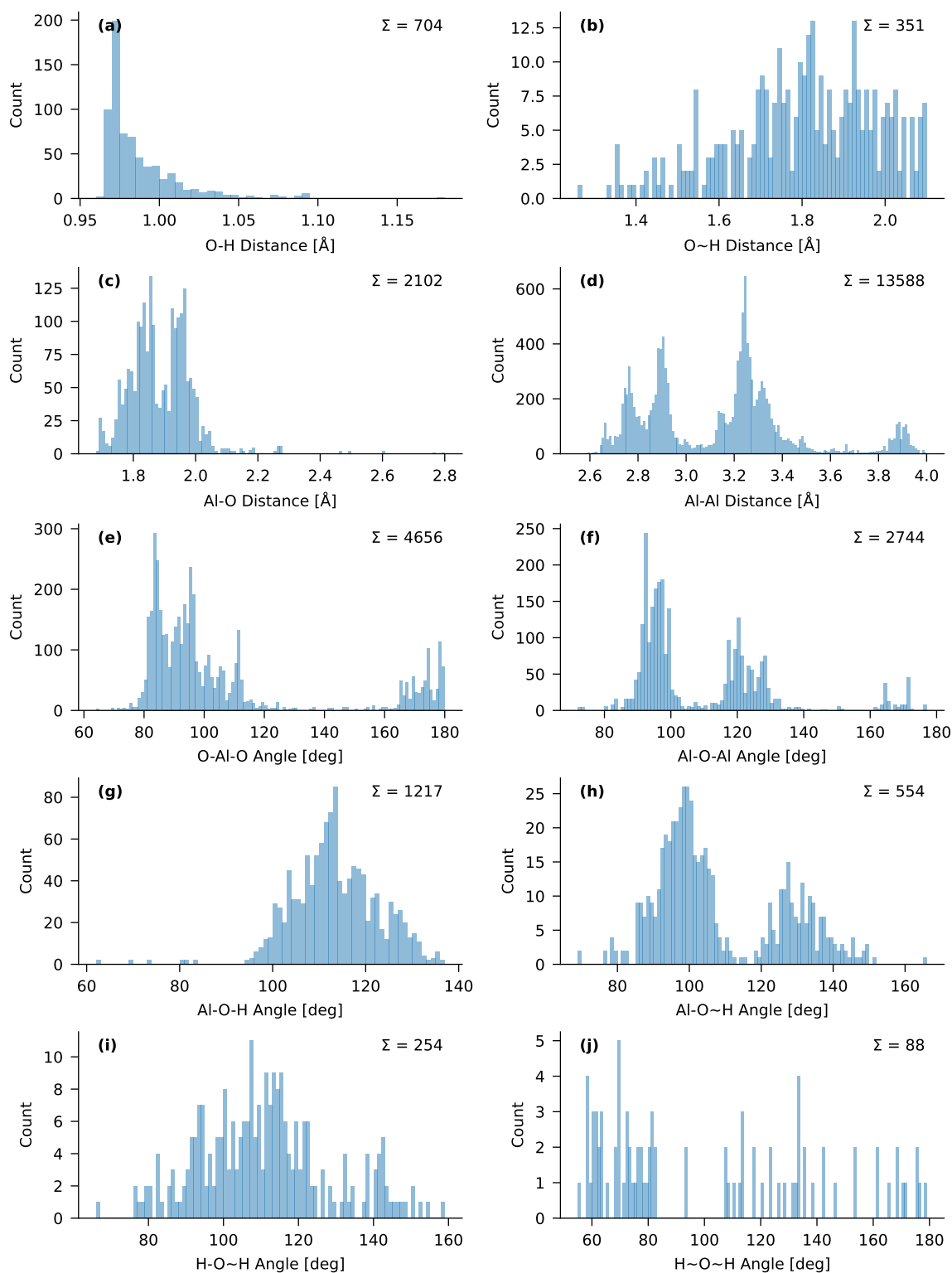


Figure S6: Histograms of internal coordinates in the validation set. In the labels on the horizontal axis, a dash represents a regular bond and a tilde represents a hydrogen bond.

Table S5: Overview of all chemical equations in the validation set. Reactants are given negative coefficients. For each reaction, three reaction energies are in kcal mol⁻¹: the reference DFT result (R), the prediction with the Joshi force field (J) and the prediction with the new force field in this work (B). Water adsorption energies are normalized to the number of water molecules. All other reaction energies are normalized on the number of Al atoms. The categories are defined in the main text.

Category	Coeff.	Structure	Chem. Form.	Reaction energy
GSH	-1/2×	gamma_surf-001_00w	Al ₆₄ O ₉₆	R -22.5
	-1×	water	O H ₂	J -14.3
	1/2×	gamma_surf-001_01w	Al ₆₄ O ₉₈ H ₄	B -31.6
GSH	-1/4×	gamma_surf-001_00w	Al ₆₄ O ₉₆	R -24.4
	-1×	water	O H ₂	J -5.0
	1/4×	gamma_surf-001_02w	Al ₆₄ O ₁₀₀ H ₈	B -27.5
GSH	-1/2×	gamma_surf-001_01w	Al ₆₄ O ₉₈ H ₄	R -26.3
	-1×	water	O H ₂	J 4.2
	1/2×	gamma_surf-001_02w	Al ₆₄ O ₁₀₀ H ₈	B -23.4
GSH	-1/6×	gamma_surf-001_00w	Al ₆₄ O ₉₆	R -23.5
	-1×	water	O H ₂	J 0.2
	1/6×	gamma_surf-001_03w	Al ₆₄ O ₁₀₂ H ₁₂	B -28.4
GSH	-1/4×	gamma_surf-001_01w	Al ₆₄ O ₉₈ H ₄	R -24.0
	-1×	water	O H ₂	J 7.4
	1/4×	gamma_surf-001_03w	Al ₆₄ O ₁₀₂ H ₁₂	B -26.8
GSH	-1/2×	gamma_surf-001_02w	Al ₆₄ O ₁₀₀ H ₈	R -21.6
	-1×	water	O H ₂	J 10.6
	1/2×	gamma_surf-001_03w	Al ₆₄ O ₁₀₂ H ₁₂	B -30.1
GSH	-1/8×	gamma_surf-001_00w	Al ₆₄ O ₉₆	R -20.8
	-1×	water	O H ₂	J -12.3
	1/8×	gamma_surf-001_04w	Al ₆₄ O ₁₀₄ H ₁₆	B -24.1
GSH	-1/6×	gamma_surf-001_01w	Al ₆₄ O ₉₈ H ₄	R -20.2
	-1×	water	O H ₂	J -11.6
	1/6×	gamma_surf-001_04w	Al ₆₄ O ₁₀₄ H ₁₆	B -21.6
GSH	-1/4×	gamma_surf-001_02w	Al ₆₄ O ₁₀₀ H ₈	R -17.1
	-1×	water	O H ₂	J -19.5
	1/4×	gamma_surf-001_04w	Al ₆₄ O ₁₀₄ H ₁₆	B -20.7
GSH	-1/2×	gamma_surf-001_03w	Al ₆₄ O ₁₀₂ H ₁₂	R -12.6
	-1×	water	O H ₂	J -49.7
	1/2×	gamma_surf-001_04w	Al ₆₄ O ₁₀₄ H ₁₆	B -11.3
GSH	-1/4×	gamma_surf-110b_from_boehm_00w	Al ₈₀ O ₁₂₀	R -60.7
	-1×	water	O H ₂	J 5.5
	1/4×	gamma_surf-110b_from_boehm_02w	Al ₈₀ O ₁₂₄ H ₈	B -50.1
GSH	-1/6×	gamma_surf-110b_from_boehm_00w	Al ₈₀ O ₁₂₀	R -58.9
	-1×	water	O H ₂	J 10.3

	1/6×	gamma_surf-110b_from_boehm_03w	Al ₈₀ O ₁₂₆ H ₁₂	B	-56.7
GSH	-1/2×	gamma_surf-110b_from_boehm_02w	Al ₈₀ O ₁₂₄ H ₈	R	-55.1
	-1×	water	O H ₂	J	19.7
	1/2×	gamma_surf-110b_from_boehm_03w	Al ₈₀ O ₁₂₆ H ₁₂	B	-70.0
GSH	-1/8×	gamma_surf-110b_from_boehm_00w	Al ₈₀ O ₁₂₀	R	-58.2
	-1×	water	O H ₂	J	-7.7
	1/8×	gamma_surf-110b_from_boehm_04w	Al ₈₀ O ₁₂₈ H ₁₆	B	-53.6
GSH	-1/4×	gamma_surf-110b_from_boehm_02w	Al ₈₀ O ₁₂₄ H ₈	R	-55.7
	-1×	water	O H ₂	J	-21.0
	1/4×	gamma_surf-110b_from_boehm_04w	Al ₈₀ O ₁₂₈ H ₁₆	B	-57.2
GSH	-1/2×	gamma_surf-110b_from_boehm_03w	Al ₈₀ O ₁₂₆ H ₁₂	R	-56.3
	-1×	water	O H ₂	J	-61.7
	1/2×	gamma_surf-110b_from_boehm_04w	Al ₈₀ O ₁₂₈ H ₁₆	B	-44.4
GSH	-1/2×	gamma_surf-110b_from_bulk_00w	Al ₆₄ O ₉₆	R	-43.6
	-1×	water	O H ₂	J	-26.1
	1/2×	gamma_surf-110b_from_bulk_02w	Al ₆₄ O ₉₈ H ₄	B	-49.6
GSH	-1/4×	gamma_surf-110b_from_bulk_00w	Al ₆₄ O ₉₆	R	-45.8
	-1×	water	O H ₂	J	-43.6
	1/4×	gamma_surf-110b_from_bulk_04w	Al ₆₄ O ₁₀₀ H ₈	B	-50.9
GSH	-1/2×	gamma_surf-110b_from_bulk_02w	Al ₆₄ O ₉₈ H ₄	R	-48.0
	-1×	water	O H ₂	J	-61.0
	1/2×	gamma_surf-110b_from_bulk_04w	Al ₆₄ O ₁₀₀ H ₈	B	-52.1
GSH	-1/6×	gamma_surf-110b_from_bulk_00w	Al ₆₄ O ₉₆	R	-39.1
	-1×	water	O H ₂	J	-32.6
	1/6×	gamma_surf-110b_from_bulk_06w	Al ₆₄ O ₁₀₂ H ₁₂	B	-41.3
GSH	-1/4×	gamma_surf-110b_from_bulk_02w	Al ₆₄ O ₉₈ H ₄	R	-36.8
	-1×	water	O H ₂	J	-35.9
	1/4×	gamma_surf-110b_from_bulk_06w	Al ₆₄ O ₁₀₂ H ₁₂	B	-37.2
GSH	-1/2×	gamma_surf-110b_from_bulk_04w	Al ₆₄ O ₁₀₀ H ₈	R	-25.6
	-1×	water	O H ₂	J	-10.7
	1/2×	gamma_surf-110b_from_bulk_06w	Al ₆₄ O ₁₀₂ H ₁₂	B	-22.2
GSH	-1/8×	gamma_surf-110b_from_bulk_00w	Al ₆₄ O ₉₆	R	-36.4
	-1×	water	O H ₂	J	-26.9
	1/8×	gamma_surf-110b_from_bulk_08w	Al ₆₄ O ₁₀₄ H ₁₆	B	-38.1
GSH	-1/6×	gamma_surf-110b_from_bulk_02w	Al ₆₄ O ₉₈ H ₄	R	-34.0
	-1×	water	O H ₂	J	-27.1
	1/6×	gamma_surf-110b_from_bulk_08w	Al ₆₄ O ₁₀₄ H ₁₆	B	-34.3
GSH	-1/4×	gamma_surf-110b_from_bulk_04w	Al ₆₄ O ₁₀₀ H ₈	R	-26.9
	-1×	water	O H ₂	J	-10.2
	1/4×	gamma_surf-110b_from_bulk_08w	Al ₆₄ O ₁₀₄ H ₁₆	B	-25.4
GSH	-1/2×	gamma_surf-110b_from_bulk_06w	Al ₆₄ O ₁₀₂ H ₁₂	R	-28.2
	-1×	water	O H ₂	J	-9.7
	1/2×	gamma_surf-110b_from_bulk_08w	Al ₆₄ O ₁₀₄ H ₁₆	B	-28.6
GSH	-1/2×	gamma_surf-110l_A1_00w	Al ₄₈ O ₇₂	R	-86.5

	-1×	water	O H ₂	J	61.0
	1/2×	gamma_surf-1101_A1_01w	Al ₄₈ O ₇₄ H ₄	B	-83.3
GSH	-1/4×	gamma_surf-1101_A1_00w	Al ₄₈ O ₇₂	R	-58.5
	-1×	water	O H ₂	J	4.1
	1/4×	gamma_surf-1101_A1_02w	Al ₄₈ O ₇₆ H ₈	B	-65.9
GSH	-1/2×	gamma_surf-1101_A1_01w	Al ₄₈ O ₇₄ H ₄	R	-30.5
	-1×	water	O H ₂	J	-52.8
	1/2×	gamma_surf-1101_A1_02w	Al ₄₈ O ₇₆ H ₈	B	-48.5
GSH	-1/6×	gamma_surf-1101_A1_00w	Al ₄₈ O ₇₂	R	-65.3
	-1×	water	O H ₂	J	21.2
	1/6×	gamma_surf-1101_A1_03w	Al ₄₈ O ₇₈ H ₁₂	B	-67.2
GSH	-1/4×	gamma_surf-1101_A1_01w	Al ₄₈ O ₇₄ H ₄	R	-54.6
	-1×	water	O H ₂	J	1.4
	1/4×	gamma_surf-1101_A1_03w	Al ₄₈ O ₇₈ H ₁₂	B	-59.2
GSH	-1/2×	gamma_surf-1101_A1_02w	Al ₄₈ O ₇₆ H ₈	R	-78.8
	-1×	water	O H ₂	J	55.5
	1/2×	gamma_surf-1101_A1_03w	Al ₄₈ O ₇₈ H ₁₂	B	-69.8
GSH	-1/8×	gamma_surf-1101_A1_00w	Al ₄₈ O ₇₂	R	-57.0
	-1×	water	O H ₂	J	15.1
	1/8×	gamma_surf-1101_A1_04w	Al ₄₈ O ₈₀ H ₁₆	B	-55.8
GSH	-1/6×	gamma_surf-1101_A1_01w	Al ₄₈ O ₇₄ H ₄	R	-47.1
	-1×	water	O H ₂	J	-0.2
	1/6×	gamma_surf-1101_A1_04w	Al ₄₈ O ₈₀ H ₁₆	B	-46.6
GSH	-1/4×	gamma_surf-1101_A1_02w	Al ₄₈ O ₇₆ H ₈	R	-55.4
	-1×	water	O H ₂	J	26.1
	1/4×	gamma_surf-1101_A1_04w	Al ₄₈ O ₈₀ H ₁₆	B	-45.6
GSH	-1/2×	gamma_surf-1101_A1_03w	Al ₄₈ O ₇₈ H ₁₂	R	-32.0
	-1×	water	O H ₂	J	-3.4
	1/2×	gamma_surf-1101_A1_04w	Al ₄₈ O ₈₀ H ₁₆	B	-21.4
GSH	-1/10×	gamma_surf-1101_A1_00w	Al ₄₈ O ₇₂	R	-49.8
	-1×	water	O H ₂	J	5.5
	1/10×	gamma_surf-1101_A1_05w	Al ₄₈ O ₈₂ H ₂₀	B	-48.5
GSH	-1/8×	gamma_surf-1101_A1_01w	Al ₄₈ O ₇₄ H ₄	R	-40.7
	-1×	water	O H ₂	J	-8.4
	1/8×	gamma_surf-1101_A1_05w	Al ₄₈ O ₈₂ H ₂₀	B	-39.8
GSH	-1/6×	gamma_surf-1101_A1_02w	Al ₄₈ O ₇₆ H ₈	R	-44.1
	-1×	water	O H ₂	J	6.4
	1/6×	gamma_surf-1101_A1_05w	Al ₄₈ O ₈₂ H ₂₀	B	-36.9
GSH	-1/4×	gamma_surf-1101_A1_03w	Al ₄₈ O ₇₈ H ₁₂	R	-26.7
	-1×	water	O H ₂	J	-18.1
	1/4×	gamma_surf-1101_A1_05w	Al ₄₈ O ₈₂ H ₂₀	B	-20.4
GSH	-1/2×	gamma_surf-1101_A1_04w	Al ₄₈ O ₈₀ H ₁₆	R	-21.4
	-1×	water	O H ₂	J	-32.8
	1/2×	gamma_surf-1101_A1_05w	Al ₄₈ O ₈₂ H ₂₀	B	-19.4

GSH	-1/12×	gamma_surf-1101_A1_00w	Al ₄₈ O ₇₂	R	-43.6
	-1×	water	O H ₂	J	-1.2
	1/12×	gamma_surf-1101_A1_06w	Al ₄₈ O ₈₄ H ₂₄	B	-42.5
GSH	-1/10×	gamma_surf-1101_A1_01w	Al ₄₈ O ₇₄ H ₄	R	-35.0
	-1×	water	O H ₂	J	-13.6
	1/10×	gamma_surf-1101_A1_06w	Al ₄₈ O ₈₄ H ₂₄	B	-34.4
GSH	-1/8×	gamma_surf-1101_A1_02w	Al ₄₈ O ₇₆ H ₈	R	-36.2
	-1×	water	O H ₂	J	-3.8
	1/8×	gamma_surf-1101_A1_06w	Al ₄₈ O ₈₄ H ₂₄	B	-30.8
GSH	-1/6×	gamma_surf-1101_A1_03w	Al ₄₈ O ₇₈ H ₁₂	R	-22.0
	-1×	water	O H ₂	J	-23.6
	1/6×	gamma_surf-1101_A1_06w	Al ₄₈ O ₈₄ H ₂₄	B	-17.8
GSH	-1/4×	gamma_surf-1101_A1_04w	Al ₄₈ O ₈₀ H ₁₆	R	-17.0
	-1×	water	O H ₂	J	-33.7
	1/4×	gamma_surf-1101_A1_06w	Al ₄₈ O ₈₄ H ₂₄	B	-16.0
GSH	-1/2×	gamma_surf-1101_A1_05w	Al ₄₈ O ₈₂ H ₂₀	R	-12.5
	-1×	water	O H ₂	J	-34.6
	1/2×	gamma_surf-1101_A1_06w	Al ₄₈ O ₈₄ H ₂₄	B	-12.7
GSH	-1/2×	gamma_surf-1101_A2_00w	Al ₅₆ O ₈₄	R	-82.6
	-1×	water	O H ₂	J	-40.3
	1/2×	gamma_surf-1101_A2_01w	Al ₅₆ O ₈₆ H ₄	B	-89.7
GSH	-1/4×	gamma_surf-1101_A2_00w	Al ₅₆ O ₈₄	R	-66.4
	-1×	water	O H ₂	J	-41.8
	1/4×	gamma_surf-1101_A2_02w	Al ₅₆ O ₈₈ H ₈	B	-75.6
GSH	-1/2×	gamma_surf-1101_A2_01w	Al ₅₆ O ₈₆ H ₄	R	-50.2
	-1×	water	O H ₂	J	-43.2
	1/2×	gamma_surf-1101_A2_02w	Al ₅₆ O ₈₈ H ₈	B	-61.5
GSH	-1/6×	gamma_surf-1101_A2_00w	Al ₅₆ O ₈₄	R	-60.3
	-1×	water	O H ₂	J	-35.4
	1/6×	gamma_surf-1101_A2_03w	Al ₅₆ O ₉₀ H ₁₂	B	-65.2
GSH	-1/4×	gamma_surf-1101_A2_01w	Al ₅₆ O ₈₆ H ₄	R	-49.1
	-1×	water	O H ₂	J	-32.9
	1/4×	gamma_surf-1101_A2_03w	Al ₅₆ O ₉₀ H ₁₂	B	-52.9
GSH	-1/2×	gamma_surf-1101_A2_02w	Al ₅₆ O ₈₈ H ₈	R	-48.1
	-1×	water	O H ₂	J	-22.5
	1/2×	gamma_surf-1101_A2_03w	Al ₅₆ O ₉₀ H ₁₂	B	-44.3
GSH	-1/8×	gamma_surf-1101_A2_00w	Al ₅₆ O ₈₄	R	-52.7
	-1×	water	O H ₂	J	-10.4
	1/8×	gamma_surf-1101_A2_04w	Al ₅₆ O ₉₂ H ₁₆	B	-56.2
GSH	-1/6×	gamma_surf-1101_A2_01w	Al ₅₆ O ₈₆ H ₄	R	-42.7
	-1×	water	O H ₂	J	-0.4
	1/6×	gamma_surf-1101_A2_04w	Al ₅₆ O ₉₂ H ₁₆	B	-45.1
GSH	-1/4×	gamma_surf-1101_A2_02w	Al ₅₆ O ₈₈ H ₈	R	-38.9
	-1×	water	O H ₂	J	21.0

	1/4×	gamma_surf-1101_A2_04w	Al ₅₆ O ₉₂ H ₁₆	B	-36.8
GSH	-1/2×	gamma_surf-1101_A2_03w	Al ₅₆ O ₉₀ H ₁₂	R	-29.8
	-1×	water	O H ₂	J	64.5
	1/2×	gamma_surf-1101_A2_04w	Al ₅₆ O ₉₂ H ₁₆	B	-29.3
GSH	-1/10×	gamma_surf-1101_A2_00w	Al ₅₆ O ₈₄	R	-46.1
	-1×	water	O H ₂	J	-5.3
	1/10×	gamma_surf-1101_A2_05w	Al ₅₆ O ₉₄ H ₂₀	B	-50.1
GSH	-1/8×	gamma_surf-1101_A2_01w	Al ₅₆ O ₈₆ H ₄	R	-37.0
	-1×	water	O H ₂	J	3.5
	1/8×	gamma_surf-1101_A2_05w	Al ₅₆ O ₉₄ H ₂₀	B	-40.2
GSH	-1/6×	gamma_surf-1101_A2_02w	Al ₅₆ O ₈₈ H ₈	R	-32.6
	-1×	water	O H ₂	J	19.0
	1/6×	gamma_surf-1101_A2_05w	Al ₅₆ O ₉₄ H ₂₀	B	-33.0
GSH	-1/4×	gamma_surf-1101_A2_03w	Al ₅₆ O ₉₀ H ₁₂	R	-24.9
	-1×	water	O H ₂	J	39.8
	1/4×	gamma_surf-1101_A2_05w	Al ₅₆ O ₉₄ H ₂₀	B	-27.4
GSH	-1/2×	gamma_surf-1101_A2_04w	Al ₅₆ O ₉₂ H ₁₆	R	-20.0
	-1×	water	O H ₂	J	15.2
	1/2×	gamma_surf-1101_A2_05w	Al ₅₆ O ₉₄ H ₂₀	B	-25.5
GSH	-1/12×	gamma_surf-1101_A2_00w	Al ₅₆ O ₈₄	R	-42.0
	-1×	water	O H ₂	J	-17.4
	1/12×	gamma_surf-1101_A2_06w	Al ₅₆ O ₉₆ H ₂₄	B	-47.1
GSH	-1/10×	gamma_surf-1101_A2_01w	Al ₅₆ O ₈₆ H ₄	R	-33.9
	-1×	water	O H ₂	J	-12.8
	1/10×	gamma_surf-1101_A2_06w	Al ₅₆ O ₉₆ H ₂₄	B	-38.5
GSH	-1/8×	gamma_surf-1101_A2_02w	Al ₅₆ O ₈₈ H ₈	R	-29.8
	-1×	water	O H ₂	J	-5.1
	1/8×	gamma_surf-1101_A2_06w	Al ₅₆ O ₉₆ H ₂₄	B	-32.8
GSH	-1/6×	gamma_surf-1101_A2_03w	Al ₅₆ O ₉₀ H ₁₂	R	-23.7
	-1×	water	O H ₂	J	0.6
	1/6×	gamma_surf-1101_A2_06w	Al ₅₆ O ₉₆ H ₂₄	B	-29.0
GSH	-1/4×	gamma_surf-1101_A2_04w	Al ₅₆ O ₉₂ H ₁₆	R	-20.7
	-1×	water	O H ₂	J	-31.3
	1/4×	gamma_surf-1101_A2_06w	Al ₅₆ O ₉₆ H ₂₄	B	-28.8
GSH	-1/2×	gamma_surf-1101_A2_05w	Al ₅₆ O ₉₄ H ₂₀	R	-21.4
	-1×	water	O H ₂	J	-77.7
	1/2×	gamma_surf-1101_A2_06w	Al ₅₆ O ₉₆ H ₂₄	B	-32.1
GSH	-1/2×	gamma_surf-1101_L2_00w	Al ₅₆ O ₈₄	R	-60.8
	-1×	water	O H ₂	J	-15.8
	1/2×	gamma_surf-1101_L2_01w	Al ₅₆ O ₈₆ H ₄	B	-58.3
GSH	-1/4×	gamma_surf-1101_L2_00w	Al ₅₆ O ₈₄	R	-44.6
	-1×	water	O H ₂	J	10.5
	1/4×	gamma_surf-1101_L2_02w	Al ₅₆ O ₈₈ H ₈	B	-51.9
GSH	-1/2×	gamma_surf-1101_L2_01w	Al ₅₆ O ₈₆ H ₄	R	-28.4

	-1×	water	O H ₂	J	36.8
	1/2×	gamma_surf-1101_L2_02w	Al ₅₆ O ₈₈ H ₈	B	-45.5
GSH	-1/6×	gamma_surf-1101_L2_00w	Al ₅₆ O ₈₄	R	-50.5
	-1×	water	O H ₂	J	25.8
	1/6×	gamma_surf-1101_L2_03w	Al ₅₆ O ₉₀ H ₁₂	B	-53.2
GSH	-1/4×	gamma_surf-1101_L2_01w	Al ₅₆ O ₈₆ H ₄	R	-45.3
	-1×	water	O H ₂	J	46.6
	1/4×	gamma_surf-1101_L2_03w	Al ₅₆ O ₉₀ H ₁₂	B	-50.6
GSH	-1/2×	gamma_surf-1101_L2_02w	Al ₅₆ O ₈₈ H ₈	R	-62.3
	-1×	water	O H ₂	J	56.5
	1/2×	gamma_surf-1101_L2_03w	Al ₅₆ O ₉₀ H ₁₂	B	-55.7
GSH	-1/8×	gamma_surf-1101_L2_00w	Al ₅₆ O ₈₄	R	-53.0
	-1×	water	O H ₂	J	24.9
	1/8×	gamma_surf-1101_L2_04w	Al ₅₆ O ₉₂ H ₁₆	B	-49.3
GSH	-1/6×	gamma_surf-1101_L2_01w	Al ₅₆ O ₈₆ H ₄	R	-50.4
	-1×	water	O H ₂	J	38.5
	1/6×	gamma_surf-1101_L2_04w	Al ₅₆ O ₉₂ H ₁₆	B	-46.2
GSH	-1/4×	gamma_surf-1101_L2_02w	Al ₅₆ O ₈₈ H ₈	R	-61.5
	-1×	water	O H ₂	J	39.3
	1/4×	gamma_surf-1101_L2_04w	Al ₅₆ O ₉₂ H ₁₆	B	-46.6
GSH	-1/2×	gamma_surf-1101_L2_03w	Al ₅₆ O ₉₀ H ₁₂	R	-60.7
	-1×	water	O H ₂	J	22.1
	1/2×	gamma_surf-1101_L2_04w	Al ₅₆ O ₉₂ H ₁₆	B	-37.5
GSH	-1/2×	gamma_surf-111_D1_03w	Al ₃₂ O ₅₄ H ₁₂	R	-60.7
	-1×	water	O H ₂	J	-5.4
	1/2×	gamma_surf-111_D1_04w	Al ₃₂ O ₅₆ H ₁₆	B	-49.0
GSH	-1/4×	gamma_surf-111_D1_03w	Al ₃₂ O ₅₄ H ₁₂	R	-49.5
	-1×	water	O H ₂	J	1.5
	1/4×	gamma_surf-111_D1_05w	Al ₃₂ O ₅₈ H ₂₀	B	-38.6
GSH	-1/2×	gamma_surf-111_D1_04w	Al ₃₂ O ₅₆ H ₁₆	R	-38.4
	-1×	water	O H ₂	J	8.5
	1/2×	gamma_surf-111_D1_05w	Al ₃₂ O ₅₈ H ₂₀	B	-28.3
GSH	-1/6×	gamma_surf-111_D1_03w	Al ₃₂ O ₅₄ H ₁₂	R	-42.9
	-1×	water	O H ₂	J	15.4
	1/6×	gamma_surf-111_D1_06w	Al ₃₂ O ₆₀ H ₂₄	B	-34.8
GSH	-1/4×	gamma_surf-111_D1_04w	Al ₃₂ O ₅₆ H ₁₆	R	-34.0
	-1×	water	O H ₂	J	25.8
	1/4×	gamma_surf-111_D1_06w	Al ₃₂ O ₆₀ H ₂₄	B	-27.7
GSH	-1/2×	gamma_surf-111_D1_05w	Al ₃₂ O ₅₈ H ₂₀	R	-29.6
	-1×	water	O H ₂	J	43.2
	1/2×	gamma_surf-111_D1_06w	Al ₃₂ O ₆₀ H ₂₄	B	-27.1
GSH	-1/2×	gamma_surf-111_D2_03w	Al ₃₂ O ₅₄ H ₁₂	R	-50.3
	-1×	water	O H ₂	J	46.1
	1/2×	gamma_surf-111_D2_04w	Al ₃₂ O ₅₆ H ₁₆	B	-27.4

GSH	-1/4×	gamma_surf-111_D2_03w	Al ₃₂ O ₅₄ H ₁₂	R	-44.4
	-1×	water	O H ₂	J	39.7
	1/4×	gamma_surf-111_D2_05w	Al ₃₂ O ₅₈ H ₂₀	B	-34.8
GSH	-1/2×	gamma_surf-111_D2_04w	Al ₃₂ O ₅₆ H ₁₆	R	-38.5
	-1×	water	O H ₂	J	33.3
	1/2×	gamma_surf-111_D2_05w	Al ₃₂ O ₅₈ H ₂₀	B	-42.1
GSH	-1/6×	gamma_surf-111_D2_03w	Al ₃₂ O ₅₄ H ₁₂	R	-39.4
	-1×	water	O H ₂	J	24.6
	1/6×	gamma_surf-111_D2_06w	Al ₃₂ O ₆₀ H ₂₄	B	-34.0
GSH	-1/4×	gamma_surf-111_D2_04w	Al ₃₂ O ₅₆ H ₁₆	R	-33.9
	-1×	water	O H ₂	J	13.8
	1/4×	gamma_surf-111_D2_06w	Al ₃₂ O ₆₀ H ₂₄	B	-37.3
GSH	-1/2×	gamma_surf-111_D2_05w	Al ₃₂ O ₅₈ H ₂₀	R	-29.4
	-1×	water	O H ₂	J	-5.6
	1/2×	gamma_surf-111_D2_06w	Al ₃₂ O ₆₀ H ₂₄	B	-32.4
GSH	-1/2×	gamma_surf-111_P1_1_05w	Al ₄₀ O ₇₀ H ₂₀	R	-21.2
	-1×	water	O H ₂	J	1.7
	1/2×	gamma_surf-111_P1_1_06w	Al ₄₀ O ₇₂ H ₂₄	B	-22.9
GSH	-1/2×	gamma_surf-111_P1_2_03w	Al ₄₀ O ₆₆ H ₁₂	R	-51.2
	-1×	water	O H ₂	J	47.5
	1/2×	gamma_surf-111_P1_2_04w	Al ₄₀ O ₆₈ H ₁₆	B	-36.4
GSH	-1/4×	gamma_surf-111_P1_2_03w	Al ₄₀ O ₆₆ H ₁₂	R	-41.3
	-1×	water	O H ₂	J	34.9
	1/4×	gamma_surf-111_P1_2_05w	Al ₄₀ O ₇₀ H ₂₀	B	-35.9
GSH	-1/2×	gamma_surf-111_P1_2_04w	Al ₄₀ O ₆₈ H ₁₆	R	-31.4
	-1×	water	O H ₂	J	22.3
	1/2×	gamma_surf-111_P1_2_05w	Al ₄₀ O ₇₀ H ₂₀	B	-35.4
GSH	-1/6×	gamma_surf-111_P1_2_03w	Al ₄₀ O ₆₆ H ₁₂	R	-35.0
	-1×	water	O H ₂	J	24.3
	1/6×	gamma_surf-111_P1_2_06w	Al ₄₀ O ₇₂ H ₂₄	B	-33.6
GSH	-1/4×	gamma_surf-111_P1_2_04w	Al ₄₀ O ₆₈ H ₁₆	R	-26.9
	-1×	water	O H ₂	J	12.7
	1/4×	gamma_surf-111_P1_2_06w	Al ₄₀ O ₇₂ H ₂₄	B	-32.2
GSH	-1/2×	gamma_surf-111_P1_2_05w	Al ₄₀ O ₇₀ H ₂₀	R	-22.3
	-1×	water	O H ₂	J	3.1
	1/2×	gamma_surf-111_P1_2_06w	Al ₄₀ O ₇₂ H ₂₄	B	-29.1
GSH	-1/2×	gamma_surf-111_P2_1_05w	Al ₄₀ O ₇₀ H ₂₀	R	-23.0
	-1×	water	O H ₂	J	60.2
	1/2×	gamma_surf-111_P2_1_06w	Al ₄₀ O ₇₂ H ₂₄	B	-15.2
GSH	-1/2×	gamma_surf-111_P2_2_04w	Al ₄₀ O ₆₈ H ₁₆	R	-46.0
	-1×	water	O H ₂	J	29.6
	1/2×	gamma_surf-111_P2_2_05w	Al ₄₀ O ₇₀ H ₂₀	B	-20.8
GSH	-1/4×	gamma_surf-111_P2_2_04w	Al ₄₀ O ₆₈ H ₁₆	R	-17.4
	-1×	water	O H ₂	J	3.1

	1/4×	gamma_surf-111_P2_2_06w	Al ₄₀ O ₇₂ H ₂₄	B	-21.7
GSH	-1/2×	gamma_surf-111_P2_2_05w	Al ₄₀ O ₇₀ H ₂₀	R	11.2
	-1×	water	O H ₂	J	-23.5
	1/2×	gamma_surf-111_P2_2_06w	Al ₄₀ O ₇₂ H ₂₄	B	-22.6
SUR	-1/32×	gamma_bulk	Al ₃₂ O ₄₈	R	5.1
	1/64×	gamma_surf-001_00w	Al ₆₄ O ₉₆	J	2.5
				B	4.9
SUR	-1/32×	gamma_bulk	Al ₃₂ O ₄₈	R	5.7
	1/80×	gamma_surf-110b_from_boehm_00w	Al ₈₀ O ₁₂₀	J	2.0
				B	3.6
SUR	-1/32×	gamma_bulk	Al ₃₂ O ₄₈	R	7.7
	1/64×	gamma_surf-110b_from_bulk_00w	Al ₆₄ O ₉₆	J	5.7
				B	7.3
SUR	-1/32×	gamma_bulk	Al ₃₂ O ₄₈	R	9.3
	1/48×	gamma_surf-1101_A1_00w	Al ₄₈ O ₇₂	J	1.4
				B	7.9
SUR	-1/32×	gamma_bulk	Al ₃₂ O ₄₈	R	7.4
	1/56×	gamma_surf-1101_A2_00w	Al ₅₆ O ₈₄	J	4.3
				B	6.6
SUR	-1/32×	gamma_bulk	Al ₃₂ O ₄₈	R	7.2
	1/56×	gamma_surf-1101_L2_00w	Al ₅₆ O ₈₄	J	1.1
				B	5.2

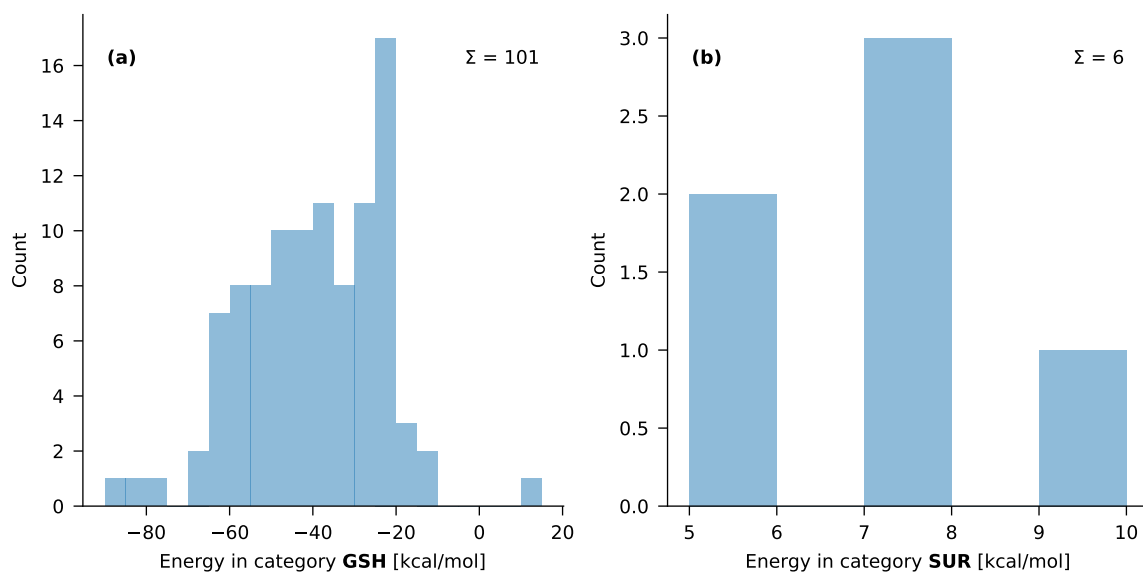


Figure S7: Histograms of reaction energies in the validation set.

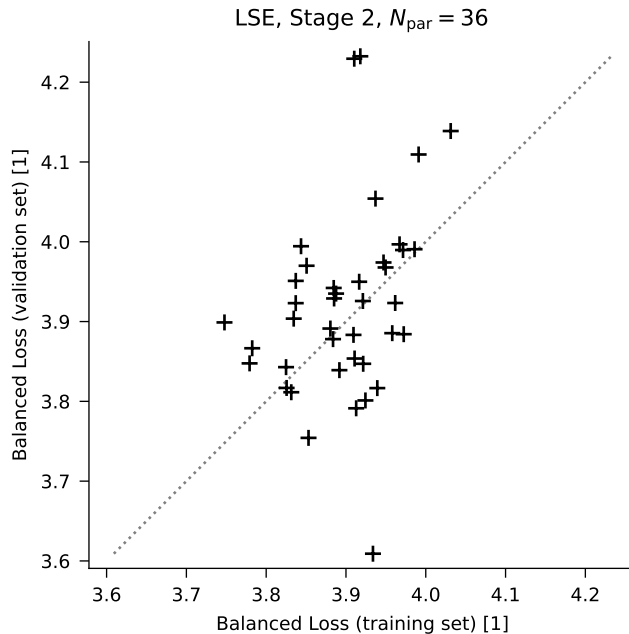


Figure S8: Parity plot comparing the value of the Balanced Loss function, for the training and validation sets, for the best solution from all 40 CMA runs (LSE form, optimization stage 2, see main text for details). Despite that the 40 optimized parameter vectors different significantly, their performance for the training and validation sets is similar.

Table S6: Comparison of root-mean-square-errors (RMSEs) of the initial force field by Joshi *et al.*¹ and the force field optimized in this work (BL). The RMSEs are computed for categories of training data and structures for which there is no counterpart in the validation set, i.e. not related to γ -Al₂O₃ surfaces. For reference, the standard deviation (SD) on the reference data is included.

Category	Unit	Ref. SD	Joshi RMSE	BL RMSE	#
Al-O	Å	0.08	0.35	0.07	1482
Al-Al	Å	0.37	0.33	0.07	1624
O-H	Å	0.03	0.26	0.04	638
O...H	Å	0.15	0.42	0.12	468
Al-O-Al	deg	22.0	9.3	3.3	1646
Al-O-H	deg	7.6	14.2	5.1	1077
O-Al-O	deg	32.2	11.0	3.2	3522
Al-O...H	deg	8.6	12.8	4.9	803
H-O...H	deg	15.8	18.2	8.1	484
H...O...H	deg	21.5	15.1	7.1	72
BSH	kcal mol ⁻¹	11.8	38.1	4.7	5
GEH	kcal mol ⁻¹	14.6	84.5	1.9	21
FOR	kcal mol ⁻¹	10.3	22.4	2.4	11

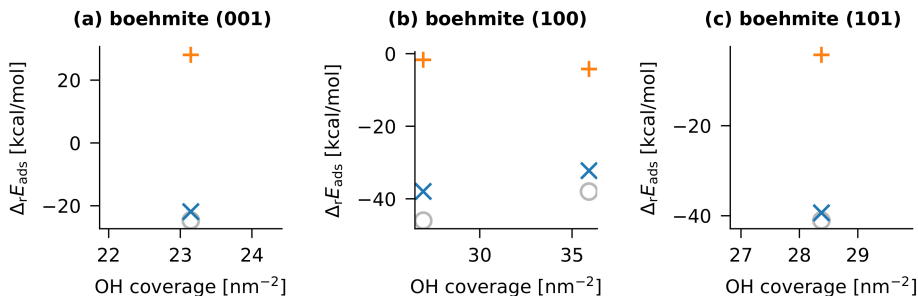


Figure S9: Adsorption energies, as defined in Eq. (3) in the main text, on boehmite surfaces as a function of the OH coverage, computed with different models: DFT (gray circle), Joshi (orange plus), this work (blue cross). All structures are derived from the training set.

S2 Comparison of Non-Equilibrium ReaxFF and DFT energies

A hydrated alumina slab (structure `gamma_surf-1101_A1_06w` from the validation set) was used as a starting point for a constant-temperature molecular dynamics (MD) run with VASP using the same level of theory as the training set. A Nosé-Hoover thermostat with a temperature of 1000 K and a relaxation time of 40 fs was used to stimulate the desorption of water from the surface. The simulation ran for 500 steps of 1 fs, and snapshots were taken every 10 steps for further analysis. Two desorption events occurs during the first 200 fs, after which no additional water molecules desorb.

The total single-point energies, E_{total} , of the selected snapshots are compared in Fig. S10(a). The DFT energies are shown in black and ReaxFF results with the new parameters in blue. ReaxFF energies obtained with the parameters of Joshi *et al.*¹ are depicted in red. The average is subtracted from both time series because these energies are only comparable up to a constant. While the fluctuations in DFT and ReaxFF energy are correlated, they also show significant deviations. This is expected, since the majority of the atoms are in the slab, not the water, and our training set emphasizes hydration reactions, not the vibrations in the alumina slab.

To show that our ReaxFF parameters can reproduce the relevant contribution to the DFT reference energy, additional single-point energies were calculated on the same snapshots from which some atoms were removed:

- E_{slab} is the energy of the slab and the water molecules that remain adsorbed, but without the atoms of the two water molecules that desorb during the simulation.
- $E_{2\text{H}_2\text{O}}$ is the energy computed for only the atoms of the two desorbing water molecules.

The energies of these two complementary subsystems are shown in Fig. S10(b) and Fig. S10(c), respectively. (Since these are also absolute energies, the average is again subtracted in both plots.) Finally, using these data, also the energy difference $(E_{\text{total}} - E_{\text{slab}} - E_{2\text{H}_2\text{O}})/2$ was computed and is shown in Fig. S10(d). In this case, no average was subtracted because the difference in energy has a chemically meaningful reference.

Fig. S10(b) shows deviations between ReaxFF and DFT energies that are very similar to those in Fig. S10(a), confirming that these deviations are due to the internal energy of the alumina slab. The results in Fig. S10(c) and Fig. S10(d) show a fair agreement between the DFT and ReaxFF energies obtained with our new parameters. Mainly Fig. S10(d) is of interest, because it is closely related to the hydration energies in the training set: This energy difference is calculated similarly to energy training data (Eq. (3) in the main text) but is now evaluated using non-equilibrium snapshots instead of optimized geometries. Because of this similarity, it is reasonable to expect a correspondence of the energies in Fig. S10(d). The average of the relative error over the first 200 fs is 25 % for the Balanced Loss parameters, which is comparable to relative errors on adsorption energies in the training set. For Fig. S10(a) and Fig. S10(b), however, a similar agreement would have been coincidental, since no related data were used for training. Also note that the new ReaxFF parameters show a clear improvement in Fig. S10(d) with respect to the parameters of Joshi *et al.*,¹ for which the relative error is 79%. In Fig. S10(c) both ReaxFF parameterizations yield the same results because the parameters for water were not refitted.

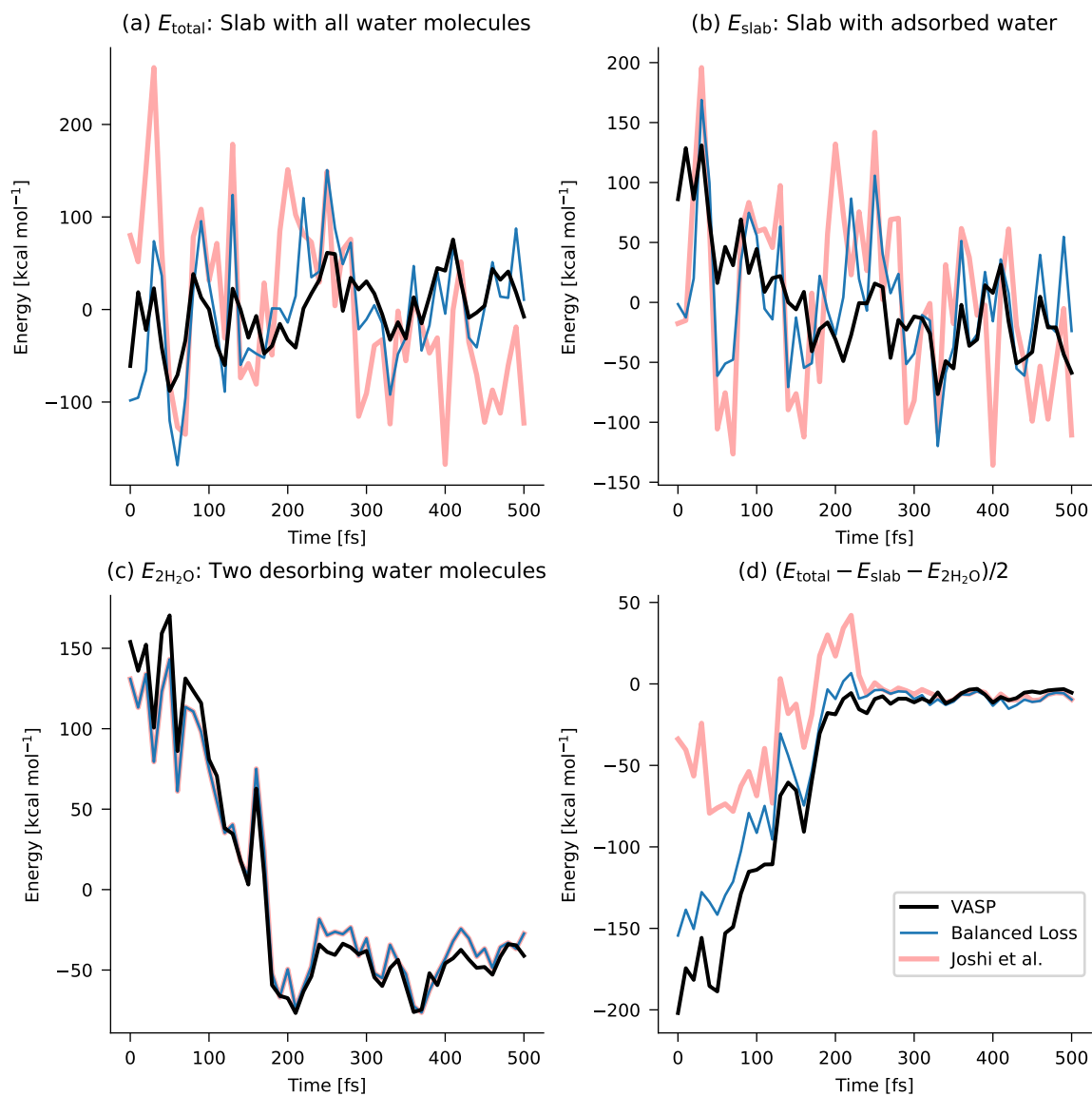


Figure S10: Comparison of DFT and ReaxFF energies for snapshots taken from a 1000 K DFT molecular dynamics simulation. (black: DFT, blue: ReaxFF with Balanced Loss parameters, red: ReaxFF with Joshi *et al.* parameters¹). Panel (a) contains the total energy of the system, panel (b) the energy of the slab and the water molecules that remain adsorbed, and panel (c) the energy of only the desorbing water molecules. Panel (d) depicts the instantaneous hydration energy as computed with Eq. (3) in the main text.

References

- (1) Joshi, K. L.; Psfogiannakis, G.; Duin, A. C. T. v.; Raman, S. Reactive molecular simulations of protonation of water clusters and depletion of acidity in H-ZSM-5 zeolite. *Phys. Chem. Chem. Phys.* **2014**, *16*, 18433–18441.